

AD-A258 907



①

AFIT/GAE/ENY/92D-26

DTIC
ELECTE
JAN 8 1993
S C D

**Behavior of a Centrally Notched
Cross-ply and Unidirectional
Ceramic Matrix Composite in
Tension-Compression Fatigue**

THESIS

William A. Weidenaar
AFIT/GAE/ENY/92D-26

93-00141



113

Approved for public release; distribution unlimited

93 1 139

AFIT/GAE/ENY/92D-26

Behavior of a Centrally Notched
Cross-ply and Unidirectional
Ceramic Matrix Composite in
Tension-Compression Fatigue

THESIS

Presented to the Faculty of the School of Engineering
of the Air Force Institute of Technology
Air University
In Partial Fulfillment of the
Requirements for the Degree of
Master of Science in Aeronautical Engineering

William A. Weidenaar

December 1992

Accession For	
NTIS	<input checked="checked" type="checkbox"/>
DTIC TAB	<input type="checkbox"/>
Unannounced	<input type="checkbox"/>
Justification	
By _____	
Distribution/	
Availability Codes	
and/or	
Dist	Special
A-1	

Approved for public release; distribution unlimited DTIC QUALITY INSPECTED

Acknowledgements

Several people provided expert guidance and support to me while completing this project. I couldn't have done it without them.

I first want to thank Dr. Shankar Mall, my advisor. He was always available to answer my many questions and guide me in the right direction.

The technicians in the AFIT Aeronautical Engineering Laboratory showed a willingness to help that was too often taken for granted. Mark Derriso, in particular, always found the time to help no matter how many ignorant students were asking for his attention.

I'd also like to thank Captain John Pernot, the project's sponsor, and Larry Zawada of the Air Force Materials Laboratory for the material and their expert advise. Others whose help was indispensable include Bob Lewis of the Material Laboratory's metallography lab and Joe Hoffele from the AFIT Model Shop. Bob provided guidance for specimen polishing and replica photography and Joe fabricated the parts required to mount the video camera.

Beyond those who were paid to help, I want to thank my wife, Jutta, who helped me keep things in perspective and my fellow students whose curiosity and technical knowledge made the "Aero Lab" a great place to work and learn.

Table of Contents

Acknowledgements	ii
List of Figures	iv
List of Tables	viii
Abstract	ix
I. Introduction	1
A. Background	1
B. Approach	3
II. Background	5
A. Experimental Background	5
B. Theoretical Background	7
III. Experimental Procedure	19
A. Test Equipment	19
B. Specimen Preparation	21
C. Specimen Alignment	23
D. Testing Procedures	26
IV. Results and Discussion	32
A. Introduction	32
B. Cross-ply Specimens	32
C. Unidirectional Specimens	69
V. Conclusions and Recommendations	85
A. Conclusions	85
B. Recommendations	88
Bibliography	89
Appendix A	91
Appendix B	93
Vita	100

List of Figures

Figure	Page
Figure 1 Uniaxial Loading in Fiber Direction	17
Figure 2 Stress Concentrations at the Hole Periphery in an Infinite Orthotropic Plate	18
Figure 3 Test Equipment Setup	20
Figure 4 Typical Plate Cutting Pattern	21
Figure 5 Specimen Schematic	23
Figure 6 Alignment Specimen Strain Gage Placement . .	24
Figure 7 Specimen Alignment	26
Figure 8 MTS 458.20 Microconsole Panel	27
Figure 9 Static Tensile Test Stress-Strain Curve . . .	34
Figure 10 Static Compression Test Stress-Strain Curve	35
Figure 11 Tension-Tension Fatigue Stress-Strain Curves	37
Figure 12 Normalized Stiffness Curve, 150 MPa Maximum Stress at Notch, Tension-Tension Fatigue . .	39
Figure 13 Hysteretic Energy Density, 150 MPa Max Stress at Notch, Tension-Tension Fatigue .	40
Figure 14 Comparison of Static Tensile Stress-Strain Curves for Different Production Batches . .	42
Figure 15 Compression-Compression Fatigue Stress- Strain Curves	43
Figure 16 Compression-Compression Fatigue Normalized Modulus	44

Figure 17	Compression-Compression Fatigue HED	44
Figure 18	Normalized Stiffness vs. Number of Cycles .	47
Figure 19	Hysteretic Energy Density vs. Number of Cycles	49
Figure 20	200 MPa T-T Fatigue Stress-Strain Curves . .	51
Figure 21	150 MPa, T-T Fatigue Stress-Strain Curves .	52
Figure 22	150 MPa, T-C Fatigue Stress-Strain Curves .	53
Figure 23	Typical Damage after Cycle One, 40X	54
Figure 24	Typical Damage up to 1,000 cycles, 40X . . .	55
Figure 25	Maximum Transverse Crack Density, 50X . . .	56
Figure 26	Specimen 92G04001, 300,000 Cycles, Near the Hole, 80X	57
Figure 27	Specimen 92G04001, 300,000 Cycles, Far from the Hole, 80X	58
Figure 28	Specimen in Tension	59
Figure 29	Specimen in Compression	60
Figure 30	Face Cracks Emanating From Hole 16X	61
Figure 31	Static Tension Failure, Face View, 3X	62
Figure 32	Static Tension Failure, Edge View, 30X	63
Figure 33	Static Compression Failure Face View, 2.5X .	64
Figure 34	Static Compression Failure, Edge View, 5X .	64
Figure 35	Tension-Tension Fatigue Failure, Face View, 2.5X	65
Figure 36	Tension-Tension Fatigue Failure, Edge View, 10X	66

Figure 37	Tension-Compression Fatigue Failure, Face View, 3X	67
Figure 38	Tension-Compression Fatigue Failure, Edge View, 5X	68
Figure 39	Stress vs. Strain, Static Tension	71
Figure 40	Stress vs. Strain, Static Compression	72
Figure 41	Tension-Tension Fatigue Stress-Strain Curve	74
Figure 42	Face Replica of Cracks Emanating from hole on Specimen 93G01000	75
Figure 43	Specimen 92G01000 after 1,000,000 Cycles	75
Figure 44	Edge Replica of Tension-Tension Fatigue Specimen	76
Figure 45	Tension-Compression, Stress-Strain Curves, 200 MPa	77
Figure 46	Front Face of Specimen 92G01003, 1,000,000 Cycles	78
Figure 47	Back Face of Specimen 92G01003, 1,000,000 Cycles	78
Figure 48	Unidirectional Normalized Stiffness Graphs	80
Figure 49	Unidirectional Hysteretic Energy Density Graphs	82
Figure 50	Tension-Compression Fatigue Edge Replica	83
Figure 51	Specimen Face at 10,000 Cycles	84
Figure 52	Strain vs. Cycles, 92G03014	93
Figure 53	Strain vs. Cycles, 92G03005	94
Figure 54	Strain vs. Cycles, 92G03013	95

Figure 55	Strain vs. Cycles, 92G03006	96
Figure 56	Specimen 92G03006 Stress-Strain Curves	99

List of Tables

Table	Page
I. Tension-Compression Test Summary	46
II. Cross-ply Tests Summary	92
III. Unidirectional Tests Summary	93
IV. Tension-Tension Maximum and Minimum Strains	97
V. Tension-Compression Maximum and Minimum Strains . .	98

ABSTRACT

The purpose of this study was to determine the behavior of centrally notched Silicon Carbide fiber-reinforced Aluminosilicate glass, SiC/1723, in tension-compression fatigue. Unidirectional, $[0]_8$, and cross-ply, $[(0/90)_2]_8$, lay-ups were investigated. All specimens had a 1.6 mm diameter hole.

The 22.24 kN MTS tension machine with modified rigid hydraulic grips in the AFIT Aeronautical Engineering Laboratory was used for all tests.

Specimen damage was monitored and recorded using stress-strain curves, stiffness reduction, hysteretic energy reduction, acetate replicas, and video.

Damage accumulated continuously for both the cross-ply and the unidirectional laminates leading to eventual failure and a reduced fatigue life. The critical damage in the cross-ply consisted of longitudinal cracks in the 90° plies. These cracks grew and combined with transverse cracks to effectively eliminate the 90° plies' load carrying capability and allowing the specimen to buckle. Critical damage in the unidirectional lay-up consisted of longitudinal cracks which initiated at the shear stress concentration points on the hole periphery. Reversed cyclic loading caused continued crack growth at stresses below the tension-tension fatigue limit.

The cross-ply lay-up appeared insensitive to the hole while critical damage in the unidirectional lay-up was dependent on the shear stress concentrations at the hole.

BEHAVIOR OF A CENTRALLY NOTCHED
CROSS-PLY AND UNIDIRECTIONAL
CERAMIC MATRIX COMPOSITE IN
TENSION-COMPRESSION FATIGUE

I. Introduction

A. Background

Future military aircraft as well as the High Speed Civilian Transport (HSCT) require engines with higher thrust-to-weight ratios than those available today. A major limiting factor in today's engine performance is material capability. Materials for the next generation of engines must withstand high temperatures for many flight cycles.

Ceramics' generally greater resistance to high temperatures than metals or polymers make them candidates for the extreme environments of advanced aircraft engines. However, the same atomic behavior that produces the excellent thermal resistance of ceramics also causes them to be hard and brittle. These characteristics lead to high compressive strengths, low fracture strengths, and high notch sensitivity.

Low fracture strength and high notch sensitivity are not desirable attributes for engine applications. One method to increase fracture toughness is to reinforce the ceramic with fibers. Strong ceramic fibers are used in order to dissipate energy during crack advance [1]. Metal

matrix composites, on the other hand, use ceramic fibers to increase their strength at the expense of some fracture toughness.

Fiber-reinforced ceramics, more commonly called ceramic matrix composites (CMCs) are expected to provide the fracture toughness and thermal resistance required for advanced aircraft engine applications. General Electric, Pratt & Whitney, and NASA are working together to fabricate a silicon carbide fiber-reinforced ceramic matrix composite combustor liner for the HSCT [2]. The Air Force Propulsion Laboratory is also supporting research to develop and characterize CMCs that may help meet their goal to double the thrust-to-weight ratio. As stated earlier, the materials used for these types of applications must have a usable life of many flight cycles.

Fatigue damage in composites can take a variety of forms. The fiber-matrix interface may fail, the matrix may crack, there may be fiber breaks, delaminations, or some combinations of these [3]. The existence of one or more of these damage modes does not necessarily constitute failure. Damage may initiate very early but because of the composites structure it may be arrested and have very little effect on the overall fatigue life.

Laboratory fatigue testing allows engineers to study the effects of cyclic loading in a controlled environment. Test variables can be altered systematically to determine

their effect, thus providing insight into ways to optimize the product's behavior for a particular application. This thesis is part of the ongoing research supporting the Propulsion Laboratory.

One variable that requires attention is the presence of holes. The effect of holes is very important since most aerospace structures require holes for cooling air, attachment points, access openings, etc. The effects of holes on CMC static strength has been looked at by Bullock [4] and their effects on CMCs in tension-tension fatigue has been examined by Moschelle [5]. This study built on these studies by changing the fatigue load ratio to include reversed loading.

The purpose of this study was to examine the effect of tension-compression fatigue on a ceramic matrix composite with a circular hole. Any effects on the fatigue limit was examined as well as damage mechanisms.

B. Approach

The material tested is SiC/1723, a silicon carbide reinforced aluminosilicate glass. This material has been the subject of several studies by the Air Force Materials Laboratory and AFIT graduate students. The Materials Laboratory has concentrated on the unnotched behavior while AFIT students have examined the effects of holes.

Tension-compression fatigue testing will be conducted

with a minimum to maximum stress ratio of -1. Stress-strain, stiffness, and hysteretic energy density (HED) curves will be generated for comparison with earlier studies and correlation with physical damage, which will also be recorded.

Two different lay-ups will be examined. $[(0/90)_2]_8$ and $[0]_8$ laminate specimens will be tested with a circular center hole. The hole diameter to specimen width ratio will be 0.26 ± 0.02 . Evaluation techniques will include acetate film replicas, microvideo, stiffness degradation, and hysteretic energy density monitoring.

An analytical model specifically for notched CMCs has not yet been formulated but test results will be compared with fatigue life models developed for graphite/epoxy composites. These models include classical laminated plate theory using the total ply discount method and the Whitney-Nuismer model.

II. Background

This chapter will describe the experimental research that has been done previously upon which this study depends and on some theoretical models that may provide a starting point for modeling CMC fatigue behavior.

The long term goal of the CMC research being done is to provide insight into the behavior and failure mechanisms which would enable the development of a realistic model. This study is a step in that direction. Testing each and every material in all lay-ups and geometries would be very expensive if not impossible. A model that accurately predicts a material's behavior under given conditions gives designers the confidence required to use the material in real-life applications.

A. Experimental Background

Research to date on the fatigue of silicon carbide fiber-reinforced ceramic matrix composites is limited but some trends have been noted. These trends will be described briefly in the following section.

In 1987 Prewo [6] tested unidirectional SiC/LAS-I in tension-tension fatigue. He found that if the fatigue stresses were below the proportional limit the composite elastic modulus and stress-strain curves were unchanged through 1,000,000 cycles. Testing above the proportional limit brought a definite change in stress-strain behavior.

The proportional limit stress was reduced and a second linear stress-strain region with an elastic modulus less than the original was found.

Zawada and Butkus [7] tested unidirectional and cross-ply SiC/1723 composite in tension-tension fatigue. They showed that at fatigue stress levels below that required for matrix microcracking, there was no loss in stiffness. Above the matrix microcracking stress the stiffness gradually decreased for unidirectional specimens, while for cross-ply specimens most of the damage occurred on the first cycle.

Tracy [8] used the same silicon carbide fiber as Zawada and Butkus but used it as a reinforcement for a different ceramic matrix. He tested NiCAlON/CAS II (0/±45/90)₃ specimens and found that testing below the second proportional limit allowed a tension-tension fatigue life of greater than 1,000,000 cycles. Testing with the fatigue stress above the second proportional limit brought failure within 700 cycles. He also applied classical laminated plate theory using total discount methods with excellent correlation.

Moschelle [5] ran tension-tension fatigue tests with centrally notched unidirectional and cross-ply SiC/1723 laminates. He found the [(0/90)₂]₃ was insensitive to the notch with fatigue limits very close to those of unnotched specimens. The fatigue limit was determined by the stress at the second proportional limit just as in Tracy's tests

[8]. Damage progression began with transverse matrix microcracking in the 90^0 plies. These cracks deflected longitudinally at the $0^0/90^0$ interface leading to delamination between the plies. Final failure was marked by fiber breakage and pullout in the 0^0 plies and an increase in transverse crack density near the fracture location in the 90^0 plies.

The effect of the hole on the $[0]_4$ laminate was more pronounced. The notch appeared to lower the ultimate tensile stress and the fatigue failure stresses for this lay-up. Cracks initiated at the theoretical shear stress concentration points, then turned and grew longitudinally, parallel to the loading direction.

Zawada and Pernot [9] examined the additional effects of various load ratios on the fatigue life of SiC/1723. They found that tension-compression fatigue resulted in continual damage accumulation and reduced fatigue life. Longitudinal cracks grew parallel to the loading direction in the 90^0 plies and caused the reduced fatigue life. Compression-compression fatigue caused no damage.

B. Theoretical Background

Theories have not yet been formulated to specifically model ceramic matrix composites. However, some models developed for polymeric or metal matrix composites have been

used in specific cases with varying success. This section looks at some of those models.

The first model is based on classical laminated plate theory. This theory is developed as follows [10]:

Given the generalized Hooke's law for an orthotropic material as

$$\sigma_i = [Q_{ij}] \epsilon_j \quad (1)$$

where σ_i are the stress components, Q_{ij} is the reduced stiffness matrix of the lamina, and ϵ_j are the engineering strain components. Each ply's reduced stiffness matrix is then transformed to the laminate coordinate system:

$$[\overline{Q}_{ij}] = [T]^{-1} [Q_{ij}] [T]^{-T} \quad (2)$$

where,

$$[T] = \begin{bmatrix} \cos^2\theta & \sin^2\theta & -2\sin\theta\cos\theta \\ \sin^2\theta & \cos^2\theta & 2\sin\theta\cos\theta \\ \sin\theta\cos\theta & -\sin\theta\cos\theta & \cos^2\theta - \sin^2\theta \end{bmatrix} \quad (3)$$

and θ is the angle from the x-axis to the l-axis, giving $[\bar{Q}]$, the transformed reduced stiffness matrix in x-y coordinates. The $[\bar{Q}]$ s for each lamina are combined to form the extensional stiffness matrix, $[A_{ij}]$. Since the focus of this thesis is on axial loading, the coupling and bending stiffness matrices are not required. The extensional stiffness matrix is defined by:

$$[A_{ij}] = \sum_{k=1}^N [\bar{Q}_{ij}]_k t_k \quad (4)$$

where t_k is the thickness of the k^{th} ply and N is the total number of plies. This gives the laminate constitutive equation as

$$\begin{pmatrix} N_x \\ 0 \\ 0 \end{pmatrix} = \begin{bmatrix} A_{11} & A_{12} & 0 \\ A_{12} & A_{22} & 0 \\ 0 & 0 & A_{66} \end{bmatrix} \begin{pmatrix} \epsilon_x^o \\ \epsilon_y^o \\ \gamma_{xy}^o \end{pmatrix} \quad (5)$$

with N_x = normal force resultant in the x-direction.

Inverting to obtain strain as a function of load leads to

$$\begin{pmatrix} \epsilon_x^o \\ \epsilon_y^o \\ \gamma_{xy}^o \end{pmatrix} = [A_{ij}]^{-1} \begin{pmatrix} N_x \\ 0 \\ 0 \end{pmatrix} \quad (6)$$

Since $\sigma_i = N_i/t$, where t is the total specimen thickness and

$$E_x = \frac{\sigma_x}{\epsilon_x^o} \quad (7)$$

the longitudinal modulus is:

$$E_x = \frac{\sigma_x}{\epsilon_x^o} = \frac{A_{11}A_{22} - A_{12}^2}{tA_{22}} \quad (8)$$

Now the initial stiffness of the cross-ply laminate can be calculated and the effective stiffness after the 90° plies have been assumed to have failed can be determined using the total discount method. Tracy [8] found that tensile fatigue failure occurred in unnotched specimens when the stiffness decreased below the discounted failure value. Moschelle [5] found that tensile fatigue failure in notched specimens occurred when the stiffness decreased the same percentage as predicted by the total discount method. This method's applicability for notched specimens in tension-compression fatigue will be examined.

Another popular model is the Whitney-Nuismer average stress criterion model. Tsangarakis [11] modified this model for fatigue and found good agreement between experimental results and the model. Whitney and Nuismer assumed failure occurs when the average stress over some distance, α_0 , equals the unnotched plate strength. The critical distance was assumed to be a

material property. A mathematical solution of this model as given by Tsangarakis is:

$$\frac{\sigma_n}{\sigma_o} = 2 * \frac{(1-X_2)}{(2-X_2^2-X_2^4)} \quad (9)$$

where,

$$X_2 = \frac{R}{(R+a_o)} \quad (10)$$

and R = radius of the hole. Tsangarakis goes on to explain that Nuismer and Whitney modified their solution to apply to an orthotropic plate.

$$\frac{\sigma_{noc}}{\sigma_o} = \frac{2(1-X_2)}{2-X_2^2-X_2^4+(K_T^o-3)*(X_2^6-X_2^8)} \quad (11)$$

where, σ_{noc} = notched strength of the infinite width plate, σ_o is the unnotched strength, and K_T^o is the corresponding orthotropic stress concentration factor.

The value of the average stress is

$$\overline{\sigma_n} = \frac{1}{a_o} \int_R^{R+a_o} \sigma(x, 0) dx \quad (12)$$

The correction for the size of the hole and plate as given by Tsangarakis is:

$$\frac{K_T}{K_T^0} = \frac{2 + (1 - 2\frac{R}{W})^3}{3(1 - 2\frac{R}{W})} \quad (13)$$

where,

K_T^0 = stress concentration factor for the infinite plate with a hole of radius, R.

K_T = stress concentration factor for plate of width, w, and a hole of radius, R.

Tsangarakis gives K_T^0 for a general orthotropic plate as

$$K_T^0 = 1 + \left[\frac{2}{A_{22}} \left[(A_{11}A_{22})^{.5} - A_{12} + \frac{A_{11}A_{22} - A_{12}^2}{2A_{66}} \right] \right]^{.5} \quad (14)$$

The values for A_{ij} are found from classical laminated plate theory as discussed earlier. This gives the ratio of notched to unnotched strength as,

$$\frac{\sigma_{noc}}{\sigma_o} = \frac{2(1-X_2)}{2 - X_2^2 - X_2^4 + (K_T - 3)(X_2^6 - X_2^8)} \quad (15)$$

Moschelle [6] also found good agreement between this theory and his experimental results for tension-tension fatigue of the unidirectional laminate.

One model that initially seems promising is the fatigue modulus model developed by Hwang and Han [13]. This model

looks promising because the data necessary to apply this model is easily obtained. However, some of the basic assumptions of this model do not apply to CMCs.

Fatigue modulus is defined as the slope of the stress vs. resultant strain at the n^{th} loading cycle and is given by,

$$F(n, r) = \frac{\sigma_a}{\epsilon_{(n)}} = \sigma_u \frac{r}{\epsilon_{(n)}} \quad (16)$$

where,

- $F(n, r)$ = fatigue modulus at the n^{th} loading cycle
- $\epsilon_{(n)}$ = resultant strain at the n^{th} loading cycle
- σ_a = applied stress
- r = ratio of applied stress, σ_a , to ultimate strength, σ_u

Initial and final conditions are assumed to be

$F(0, r) = F_0 \approx E_0$ and $F(N, r) = F_f$ = final fatigue modulus, respectively. The authors assume the fatigue modulus degradation rate, dF/dn , acts like a power function of cycles, n , i.e., $dF/dn = -A n^{c-1}$; where, A and c are material constants. Integrating from 0 to n yields,

$$F(n) - F(0) = -A n^c \quad (17)$$

At failure $n = N$ and

$$F_f - F_{(0)} = -AN^c \quad (18)$$

Therefore, the number of cycles to failure is given by:

$$N = \left[B \left(1 - \frac{F_f}{F_0} \right) \right]^{\frac{1}{c}} \quad (19)$$

where, $B = F_0/A$.

The authors go on to apply strain failure criterion. This criterion says that final failure of the material occurs when the fatigue resultant strain reaches the static ultimate strain. They assume the material follows an elastic stress-strain relation under static loading giving:

$$\sigma_u = E_0 \epsilon_u = F_0 \epsilon_u \quad (20)$$

where, σ_u = ultimate strength and ϵ_u = ultimate strain. Fatigue modulus gives the relation,

$$\sigma_s = F_{f,s} \epsilon_{f,s} \quad (21)$$

where,

σ_s = applied stress

$F_{f,s}$ = fatigue modulus at failure at stress level σ_s .

$\epsilon_{f,s}$ = resultant strain at failure at stress level σ_s .

Using the strain failure criterion ($\epsilon_u = \epsilon_{f,a}$) gives

$$F_{f,a}/F_0 = \sigma_a/\sigma_u = r \quad (22)$$

Putting this into Eq (19) gives,

$$N=[B(1-r)]^{\frac{1}{c}} \quad (23)$$

This is a nice, simple expression for the number of cycles to failure but the stress-strain curve for ceramic matrix composites is extremely nonlinear which is contrary to the basic assumptions of this model. Therefore, results from this model will not correlate well with experimental results [5].

This study investigates the behavior of notched CMC specimens in tension-compression fatigue. To understand the effects of the hole one should examine the theoretical state of stress near the hole. Although the specimens were far from infinite, calculating the stresses around the hole in an infinite plate should give an idea of the trends for the specimens in the present study.

The circumferential stress at the edge of the hole of a uniaxially loaded orthotropic plate (Figure 1) where the loading direction is the same as the fiber direction is given by [13]:

$$\sigma_{\theta L} = \left[\frac{(1+\gamma_1)(1+\gamma_2)(1+\gamma_1+\gamma_2-\gamma_1\gamma_2-2\cos 2\theta)}{(1+\gamma_1^2-2\gamma_1\cos 2\theta)(1+\gamma_2^2-2\gamma_2\cos 2\theta)} \right] \sigma_L \quad (24)$$

where,

$$\gamma_1 = \frac{\left[\left(\frac{E_T}{2G_{LT}} - \nu_{TL} \right) + \left[\left(\frac{E_T}{2G_{LT}} - \nu_{TL} \right)^2 - \frac{E_T}{E_L} \right]^{.5} \right]^{.5} - 1}{\left[\left(\frac{E_T}{2G_{LT}} - \nu_{TL} \right) + \left[\left(\frac{E_T}{2G_{LT}} - \nu_{TL} \right)^2 - \frac{E_T}{E_L} \right]^{.5} \right]^{.5} + 1} \quad (25)$$

$$\gamma_2 = \frac{\left[\left(\frac{E_T}{2G_{LT}} - \nu_{TL} \right) - \left[\left(\frac{E_T}{2G_{LT}} - \nu_{TL} \right)^2 - \frac{E_T}{E_L} \right]^{.5} \right]^{.5} - 1}{\left[\left(\frac{E_T}{2G_{LT}} - \nu_{TL} \right) - \left[\left(\frac{E_T}{2G_{LT}} - \nu_{TL} \right)^2 - \frac{E_T}{E_L} \right]^{.5} \right]^{.5} + 1} \quad (26)$$

E_L is the modulus of elasticity in the fiber direction, E_T is the modulus of elasticity in the transverse direction, G_{LT} is the in-plane shear modulus, and ν_{TL} is the Poisson's ratio giving the transverse strain due to a stress in the longitudinal (fiber) direction.

The stresses, σ_{LL} , σ_{TT} , σ_{LT} associated with the principal axes of the plate are,

$$\sigma_{LL} = \sigma_{\theta L} \sin^2 \theta \quad (27)$$

$$\sigma_{TT} = \sigma_{\theta L} \cos^2 \theta \quad (28)$$

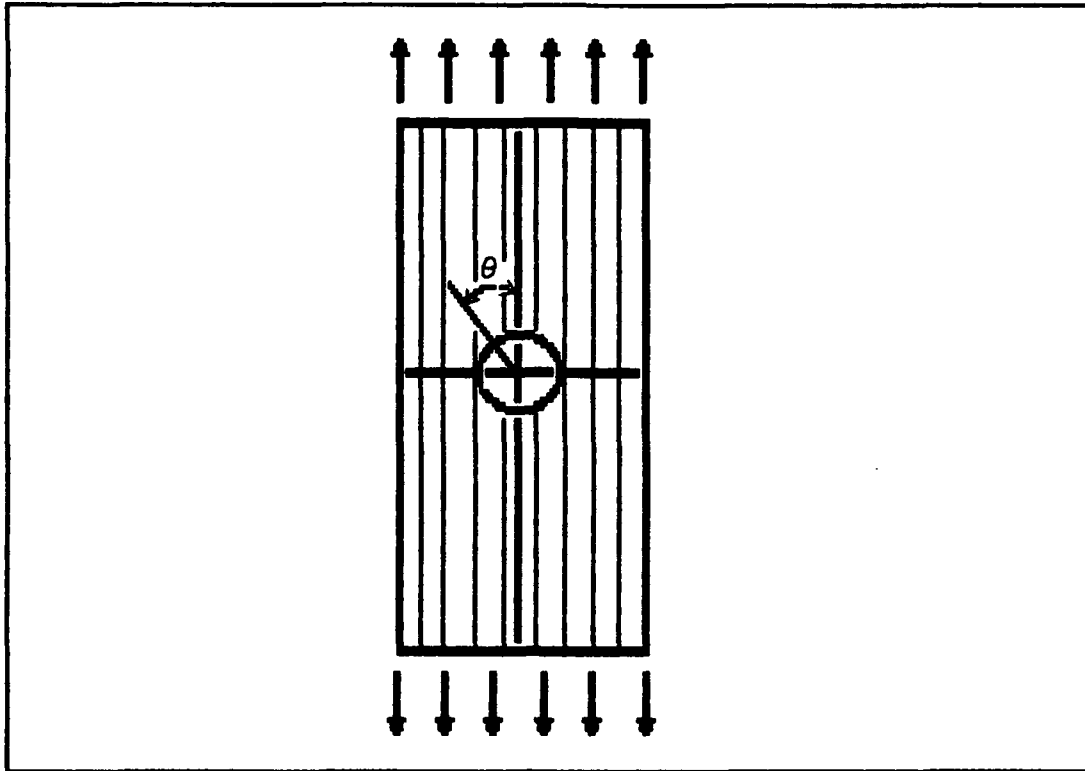


Figure 1 Uniaxial Loading in Fiber Direction

$$\sigma_{LT} = -\sigma_{\theta L} \sin\theta \cos\theta \quad (29)$$

The stress concentrations around the periphery of the hole, σ_{LL}/σ_L , $\sigma_{\theta\theta}/\sigma_L$, $\sigma_{L\theta}/\sigma_L$ can be calculated given the material properties. Bachmann [14] has given the material properties for SiC/1723 as:

$$E_L = 140 \text{ GPa}$$

$$E_\theta = 88 \text{ GPa}$$

$$G_{L\theta} = 44 \text{ GPa}$$

$$\nu_{\theta L} = 0.18$$

This gives the stress concentrations from 0 to 1.57 radians (90°) as shown in Figure 2.

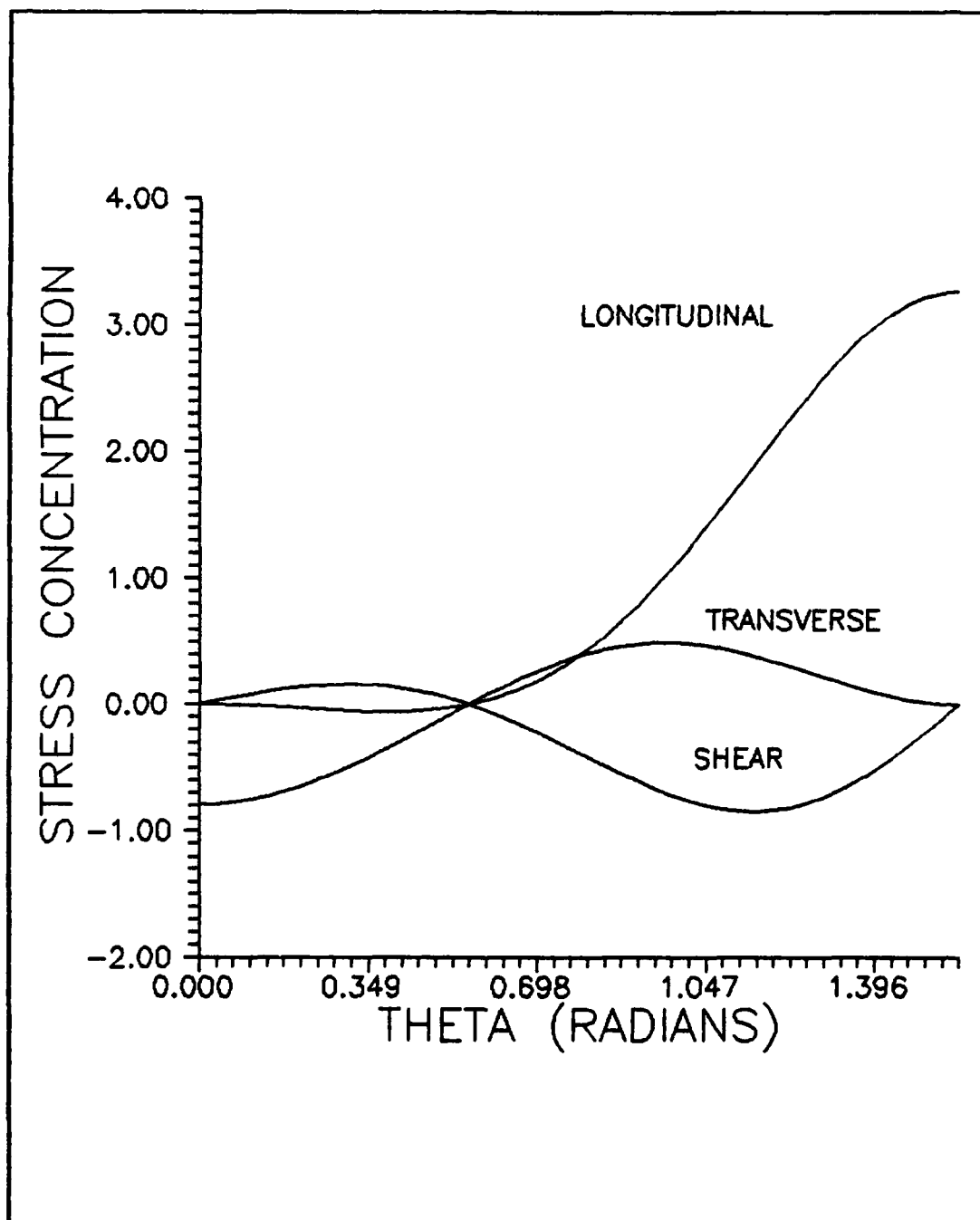


Figure 2 Stress Concentrations at the Hole Periphery in an Infinite Orthotropic Plate

The theories covered in this chapter will be applied in Chapter IV and compared to the experimental results.

III. EXPERIMENTAL PROCEDURE

This chapter describes the equipment used to run the tests and collect data, specimen preparation, verification of specimen alignment, and test procedures.

A. Test Equipment

The 22.24 KN MTS tensile test machine used for these tests has been used previously by Tracy [8] and Moschelle [5] to investigate the fatigue properties of ceramic matrix composites. Tracy modified the grip system per Hartman's design [15]. This rigid grip system uses hydraulic pressure from an air driven pump to close the grips and secure the specimen. An anti-rotation device was also fabricated and attached to the actuator to eliminate any rotation of the specimen.

The MTS test stand consisted of a test frame with a 5000 lb MTS Servoram Actuator, a 22.24 kN load cell, an MTS 464.80 Data Display Module, and an MTS 458 Microconsole. Additional equipment used for these tests included a IBM PC-AT computer, a Wavetek model 75 waveform generator, a Measurements Group 2310 Amplifier, and an MTS model 632.26B-30 extensometer. The test equipment setup is shown in Figure 3.

The fatigue testing was controlled by the personal computer and the waveform generator using a fatigue cycling

program (MATE233) developed by Hartman at the University of Dayton Research Institute. An additional data acquisition program (MODULUS), developed by Sanders [16] at AFIT was used for the static tension and compression tests.

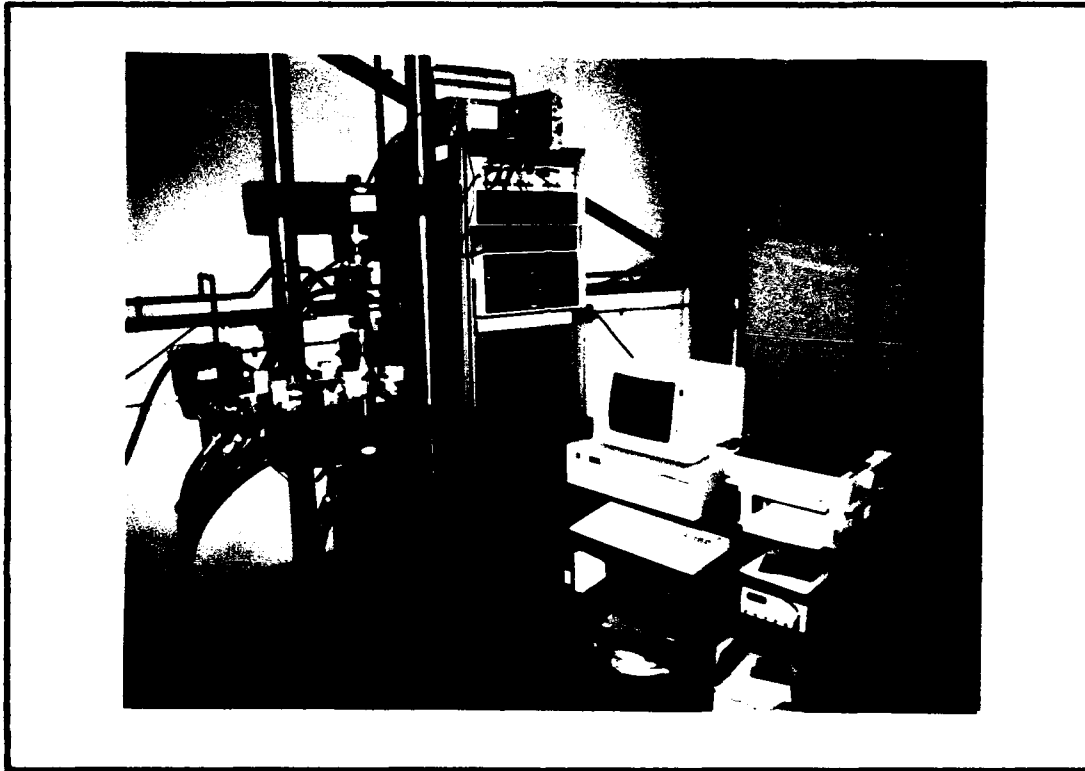


Figure 3 Test Equipment Setup

A video system was set up to view and record real time observations of specimen response to cyclic loading. All components of this system were borrowed, as needed, from other systems within the lab. An old Bausch and Lomb optical microscope provided the optics. One eyepiece was removed and a Panasonic CCTV model WV-1410 video camera was inserted into the viewing tube. The camera was connected to a monitor and VCR. The microscope, video camera, and a

light were mounted on a fixture attached to a tripod. The fixture provided reasonably precise, if not vibration free, x, y, and z adjustments.

B. Specimen Preparation

This study investigates a ceramic matrix composite designated as SIC/1723. It is made up of aluminosilicate glass matrix manufactured by Corning Glass Works reinforced with Tyranno_® silicon carbide fibers developed by Yajima [17]. The composite was processed by the Materials Laboratory into 100 mm by 100 mm by 2.54 mm (on average) plates. To remove edge effects and to provide a 38.1 mm gage length the test specimens were trimmed to 76.2 mm long. This provided 19 mm on each end for tabs. A typical plate cutting pattern is shown in Figure 4. The center holes

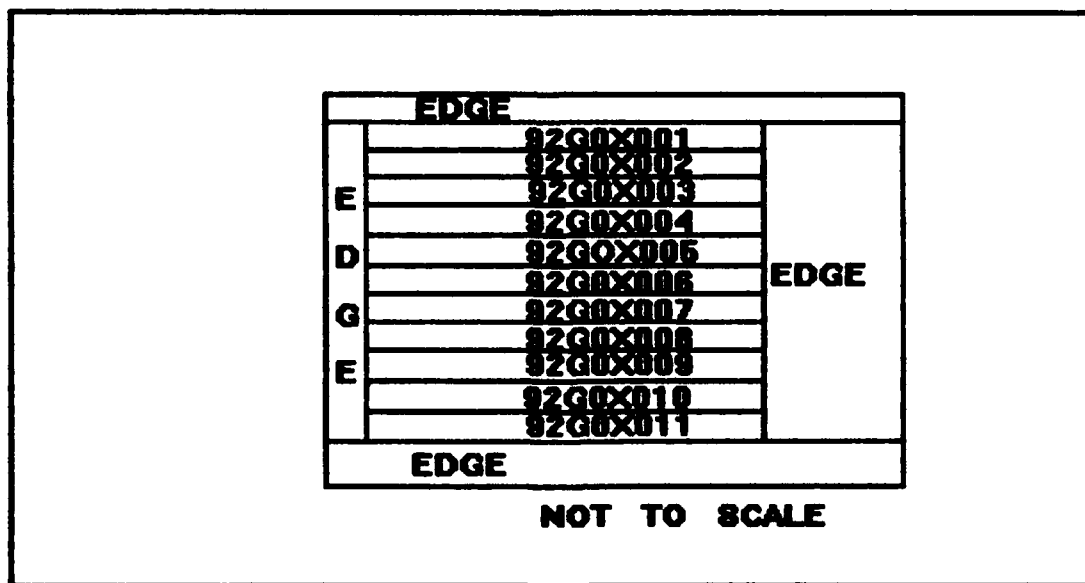


Figure 4 Typical Plate Cutting Pattern

were drilled ultrasonically using a 1.524 mm diameter rod. The diamond slurry abrasive used by the ultrasonic drill in conjunction with the rod gave the holes a final diameter of 1.6 mm. Since a D/W ratio of .26 was desired for all tests, a specimen width of 5.97 mm was needed.

The specimens were polished on one edge to allow acetate replication or video taping. All polishing was done on an eight inch diameter Buehler polishing wheel at approximately 300 rpm. The first step consisted of ten minutes using a diamond "FINE GRIND" wheel to ensure a flat, perpendicular surface. Next a diamond "ROUGH POLISH" wheel was used for ten minutes to prepare the specimen for final polishing.

Final polishing was done in two steps. The first used three micron suspension fluid on a nylon mat. After 45 minutes of polishing with the three micron fluid, the nylon mat was replaced and one micron suspension fluid was used for another 45 minutes. This provided an adequate finish for replicas and video. Polishing the hole was not attempted due to the problems Moschelle [5] had.

To complete the specimen preparation, fiberglass tabs were epoxied on the ends of each specimen. The tabs provided a secure gripping surface for the serrated grip inserts while protecting the specimens from any stress concentrations grooves or scratches.

The tabs were mounted to the specimens with a 50/50 mixture of EPON brand epoxy resin and V-40 curing agent. The surface of the tabs was sanded lightly with medium grit emery cloth to ensure a good bond. The tabs were held in place with binder clips while the epoxy cured. To expedite curing the specimens were placed in a oven at 78.3°C for 90 minutes. A schematic of a prepared specimen is shown in Figure 5.

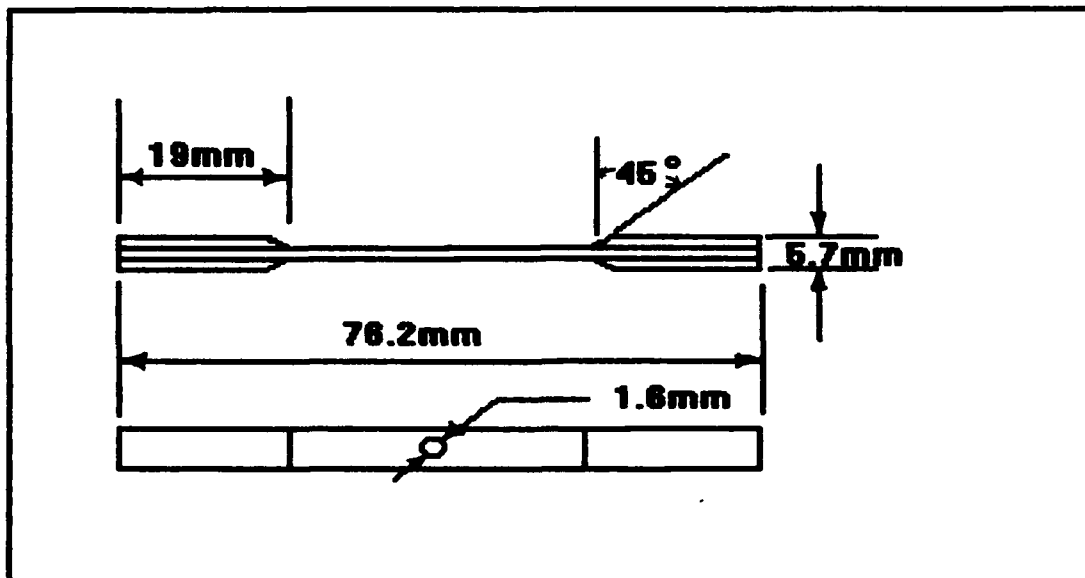


Figure 5 Specimen Schematic

C. Specimen Alignment

Specimen alignment is critical when fatigue testing CMCs. Even slight bending can cause premature damage affecting the stiffness and strength [15]. Because of this, specimen alignment was verified in accordance with ASTM Standard E 1012-89 methods two and three. Method three consists of visually inspecting the test fixtures, machine,

and specimens. Method two consists of measurement of longitudinal strain at the mid-length locations on each side of a test specimen as shown in Figure 6. Bending strains are then determined from ratios of opposing strain measurements.

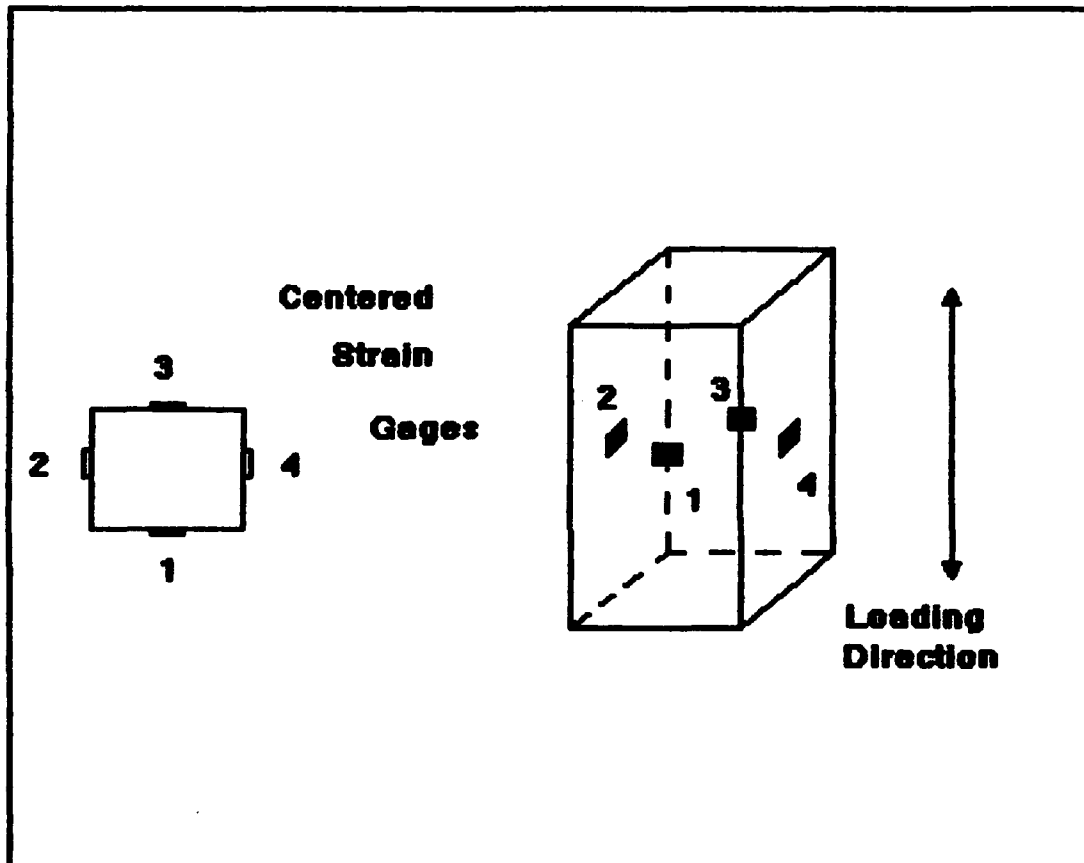


Figure 6 Alignment Specimen Strain Gage Placement

Alignment method three was the first and the last method used. The first step in specimen alignment was to bring the grips together to demonstrate that all four sides and the faces were flush with each other. The last step occurred when placing the specimen in the grips just prior to testing. A carefully machined aluminum block in

conjunction with the machined surfaces of the grips was used to align the specimen. If the edges of the specimen within the grip area were clear of any excess epoxy from tab application, a depth gage was also used to ensure the top and bottom of the specimen were equal distances from the machined edges of the grips.

Method two was used to verify the alignment during tensile loading. The four strains measured from the strain gages placed as shown earlier were used to obtain an axial strain, a .

$$a = (e_1 + e_2 + e_3 + e_4) / 4 \quad (30)$$

The local bending strains, b_i , are calculated as follows for $i = 1$ to 4:

$$b_i = e_i - a \quad (31)$$

The maximum bending strain, B , is calculated from:

$$B = \frac{|b_1 - b_3|}{2} + \frac{|b_2 - b_4|}{2} \quad (32)$$

Percent bending, PB , is found using:

$$PB = (B/a) 100 \quad (33)$$

Figure 7 shows a sample graph from alignment tests using a 0.25 inch by 0.25 inch square cross section four inch long

steel specimen. This graph demonstrates the excellent alignment of the test station.

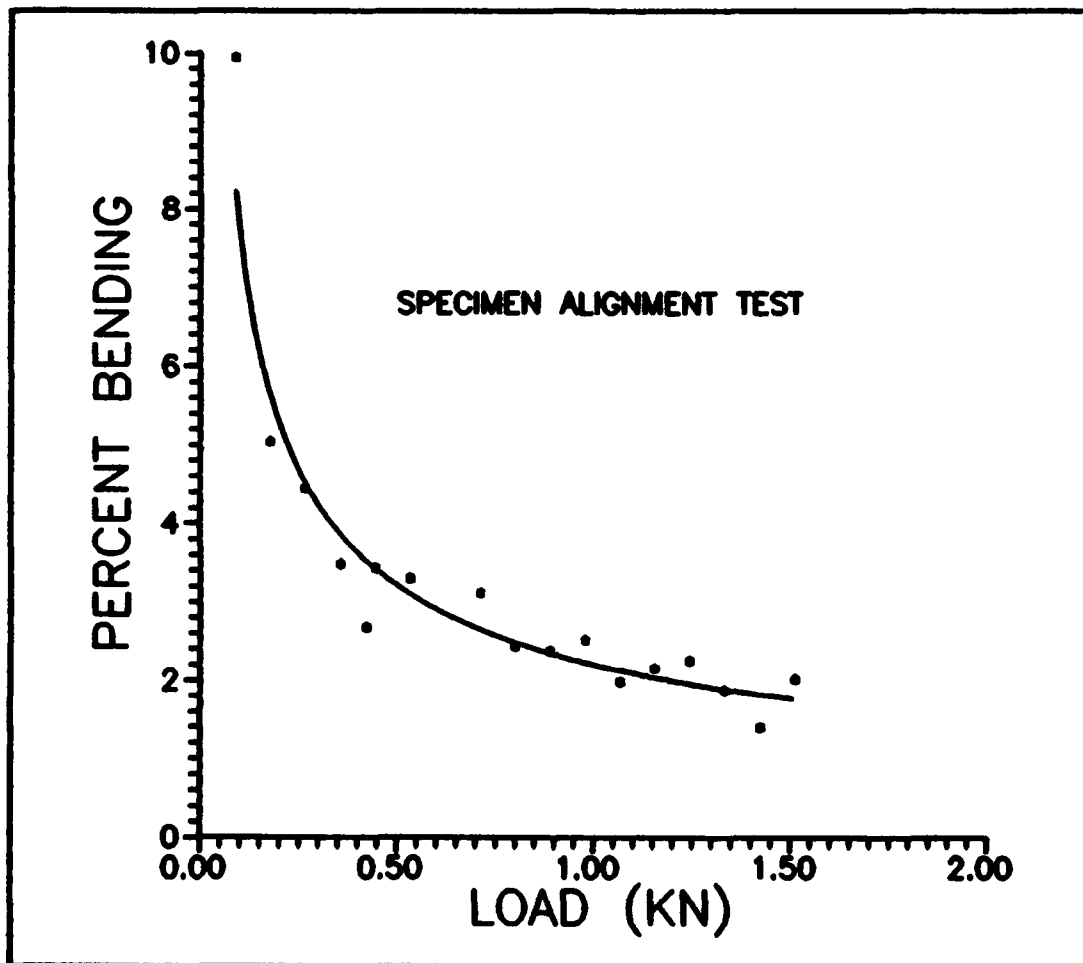


Figure 7 Specimen Alignment

D. Testing Procedures

Static tension and compression tests were run as well as fatigue tests. Test procedures for all of these tests were the same until the test control or data acquisition software was chosen. Control of the 22.24 kN tensile test machine was through the MTS 458.2 Microconsole (Figure 8) for this portion of the tests.

The first step was to ensure the correct load card was installed in the DC Controller for load (Force). The closer the limit of the load card was to the maximum test load to be applied the more accurately load adjustments could be made. However, if during the cyclic tests the maximum load applied was close to the capacity of the load card the equipment was unable to accurately maintain the correct load at 10 Hz. Using a load card that put the maximum test load between 50 and 65 percent, if possible, was a good compromise.

The hydraulic pressure could now be applied. The pressure was first set "Low" and then to "High". If not already accomplished, displacement control was selected and the ram actuator was cycled repetitively to ensure free and controllable movement.

Load display was selected and the zero point was set. Using the zero adjustment on the DC Controller for load (Force) the display was set to zero. This removed the weight of the hydraulic grip yokes and the grips from the loads to be applied to the specimen.

The specimen was placed and aligned in the grips. Removable steel inserts were installed in the grips. The thickness of the insert chosen was based on the thickness of the specimen. The specimen fit within the grips with very little play before any hydraulic pressure was applied to the grips when the correct insert was used. The close fit and

the grooves machined into the inserts helped hold the specimen securely. The specimen was first placed in the bottom grips, aligned with the machined aluminum alignment block, and pressure was applied to the grips. The top of the specimen was then moved into position within the top grips and pressure was applied. Pressure in the grips was set at approximately 16.5 MPa. Actuator control was switched to load control and the load was zeroed using the set point control. Alignment of the specimen was again checked to ensure proper alignment prior to applying load.

Control of the actuator was switched to load control prior to positioning into the top grip if a compression test was to be run. The specimen was positioned with its ends butting against the surface of the grips for the static compression tests to ensure there would be no slipping at the higher loads required for these tests.

The extensometer was then attached at the desired location to provide displacement readings. An MTS model 632.26B-30 was attached to the edge of the specimen using four small rubber bands. The rubber bands provided the pressure necessary to reduce the chance for slippage while not damaging the specimens. The springs provided with the extensometer tended to chip the corners of the specimen. The extensometer was connected to the signal amplifier, the restraining pin was removed, and the displacement reading was zeroed. This completed the hardware setup.

The procedures used to set up the software varied depending on the type of test to be run. Static tests used data acquisition software developed by Sanders [17] at AFIT and the load was applied "manually" by using the set point control on the MTS 458.20.

The software for the fatigue tests controlled the loading, collected data, and provided some data analysis capability. The software used was MATE233 developed by Hartman of the University of Dayton Research Institute.

Data for the tension-tension and compression-compression fatigue tests was acquired logarithmically. In other words, data was collected at cycles one, two, five, ten, twenty, fifty, one hundred, etc. up until one million cycles. This was done since most of the damage from tension-tension fatigue occurs in the first few thousand cycles. Damage was not expected in the compression-compression tests at the load levels tested so the number of cycles between data acquisition cycles was not critical.

Data for the tension-compression fatigue tests was acquired logarithmically up to 100,000 cycles. Data was then acquired every 50,000 cycles. This was done to try and capture the results of any damage accumulation.

Load versus time curves were sine waves for all fatigue tests. Fatigue testing was run at ten hertz except when it was slowed down for video. The tests were cycled at 0.5 to 5 Hz when being video taped.

The tests were stopped periodically to take acetate replicas. Replicas are taken by wetting the specimen with acetone and pressing acetate film against it. When the acetone dries, an imprint of the specimen is imbedded in the acetate. The acetate can then be examined with microscopes and saved for later reference. Replicas were taken at various loading conditions to determine loading effects on crack opening and to show crack progression with cycling. Results of the stress-strain data, video, and replications are discussed in Chapter IV.

IV. RESULTS AND DISCUSSION

A. Introduction:

This chapter describes the tests performed. Results of the tests will be discussed and compared to results from previous studies and to the theories discussed in Chapter II. Special attention will be given to any effects of the hole. As mentioned previously, the objective of the present study is to determine those effects. Section B will detail the tests on the cross-ply specimens, while Section C will cover the unidirectional specimen tests. Tabular summaries of the tests are in Appendix A.

B. Cross-ply Specimens

1. Experimental Results: As discussed in Chapter II, previous tests by Moschelle [5] and Zawada [8] have shown the existence of a fatigue limit for notched and unnotched tension-tension fatigue specimens respectively. The fatigue limit was defined as the maximum stress applied during a fatigue cycle where the specimen would not fail when subjected to 1,000,000 cycles. Zawada [9] has also shown that damage accumulation in unnotched specimens in tension-compression fatigue continued until eventual failure of the specimen even with stresses below the tension-tension

fatigue limit. Zawada found that cracks parallel to the loading direction grew continuously in the 90 degree plies and caused the reduction in fatigue life.

To demonstrate the additional effects of compression in conjunction with tensile stresses on the fatigue life of notched CMC specimens, it was necessary to first obtain a baseline for comparison. The first step was to perform a static tension test. The stress-strain curve from the static tension test was then used to determine maximum stress values for tension-tension fatigue tests. Once a fatigue limit for tension-tension fatigue was found, reversed cyclic loading was applied to determine the effects of the addition of compressive loading. Sample load versus time curves are shown in Appendix B. In addition, static compression and compression-compression fatigue tests were run to identify the applicable failure modes for comparison.

A typical static tension test stress-strain curve is shown in Figure [9]. The extensometer was placed away from the hole for this test. This curve demonstrates the characteristic two proportional limit curve of a symmetric cross-ply CMC. The first proportional limit occurs at 55 MPa and corresponds to the onset of matrix microcracking, while the second proportional limit at 160 MPa corresponds to the stress at which the 0 degree plies begin to exhibit nonlinear behavior due to its matrix cracking.

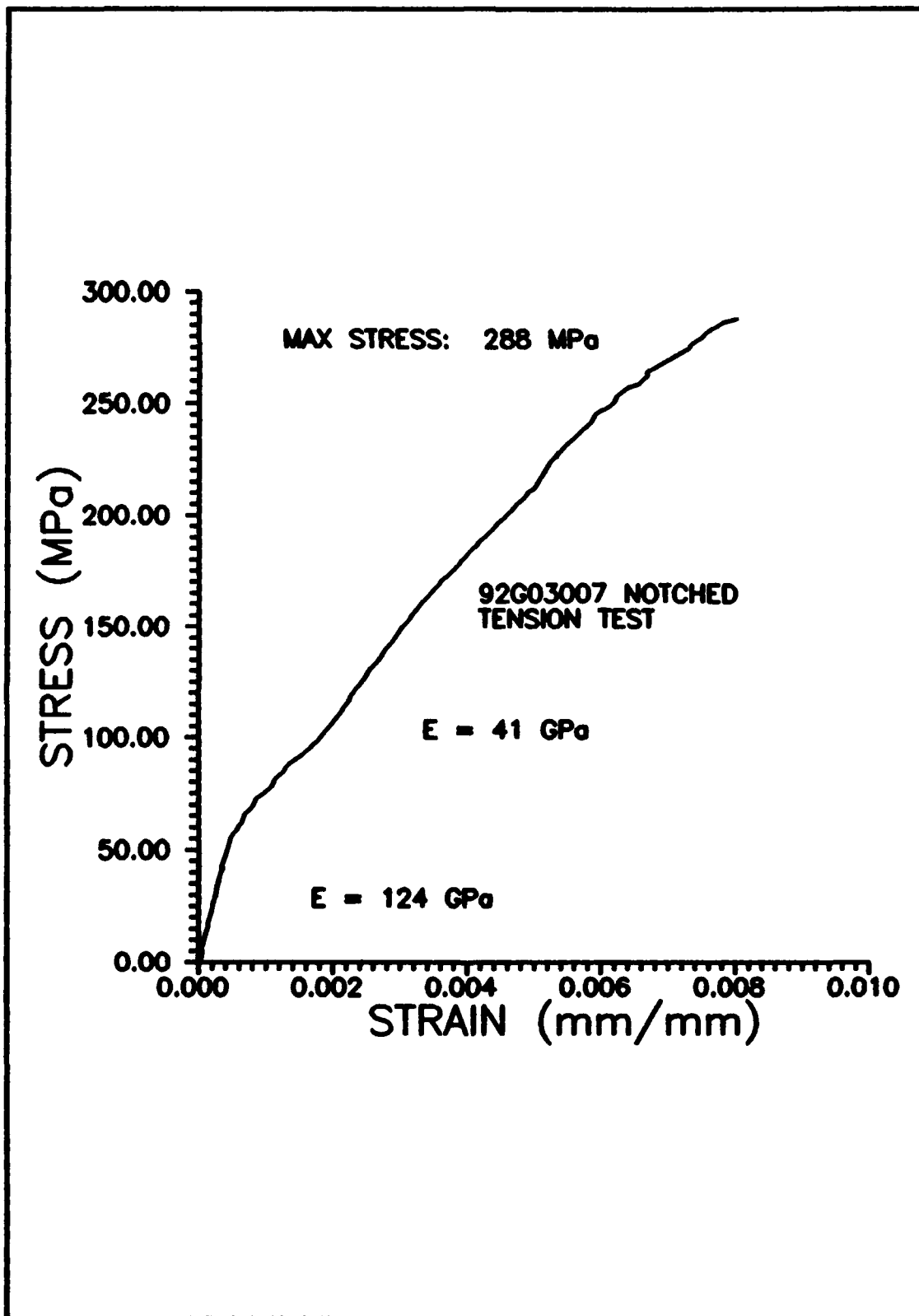


Figure 9 Static Tensile Test Stress-Strain Curve

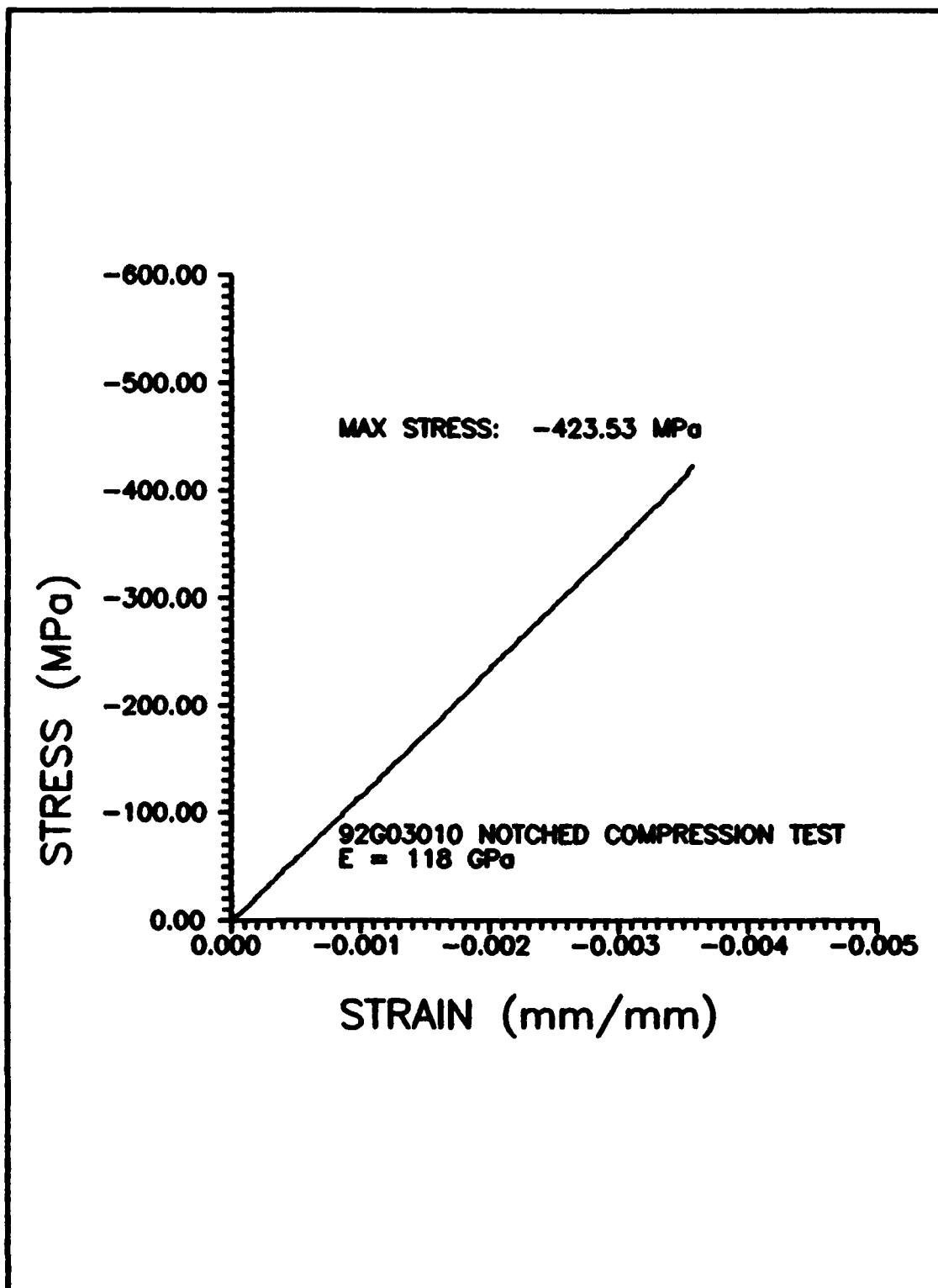


Figure 10 Static Compression Test Stress-Strain Curve

The static compression test stress-strain curve shown in Figure [10] shows no damage effects until the ultimate compressive strength is reached. At this level sudden catastrophic failure occurs. The extensometer was away from the hole for this test.

Moschelle related the fatigue limit of notched CMC with its ultimate strength. He found that using maximum stress levels of under 80% of the ultimate strength resulted in test runout ($> 1,000,000$ cycles). The ultimate stress from Figure 9 is 288 MPa. 80% of this value is 230 MPa. Therefore a maximum stress of 250 MPa was chosen for the first tension-tension fatigue test. This was above 80% of ultimate and it was above the second proportional limit. The maximum stress value is for the notched area. The stress level at the extensometer location was somewhat lower. This test used specimen 92G03011 and failure occurred at approximately 37,000 cycles.

The next tension-tension test was run on specimen 92G03014 with a maximum stress of 200 MPa. This value was above the second proportional limit but below 80% of ultimate. This specimen failed at 64,227 cycles.

Thereafter, specimen 92G03005 was cycled using a maximum stress of 150 MPa. This brought the maximum stress below the second proportional limit but still above the first proportional limit. This test was stopped at

1,000,000 cycles, achieving "runout". Stress strain curves for this test are shown in Figure 11.

These curves indicate that the greatest damage occurs in the first cycle. The curve for cycle one goes nonlinear at the point corresponding to the first proportional limit found in the static tensile test. The curves for the remaining cycles are nearly parallel below 30 MPa indicating the transverse cracks are closed at these stress levels.

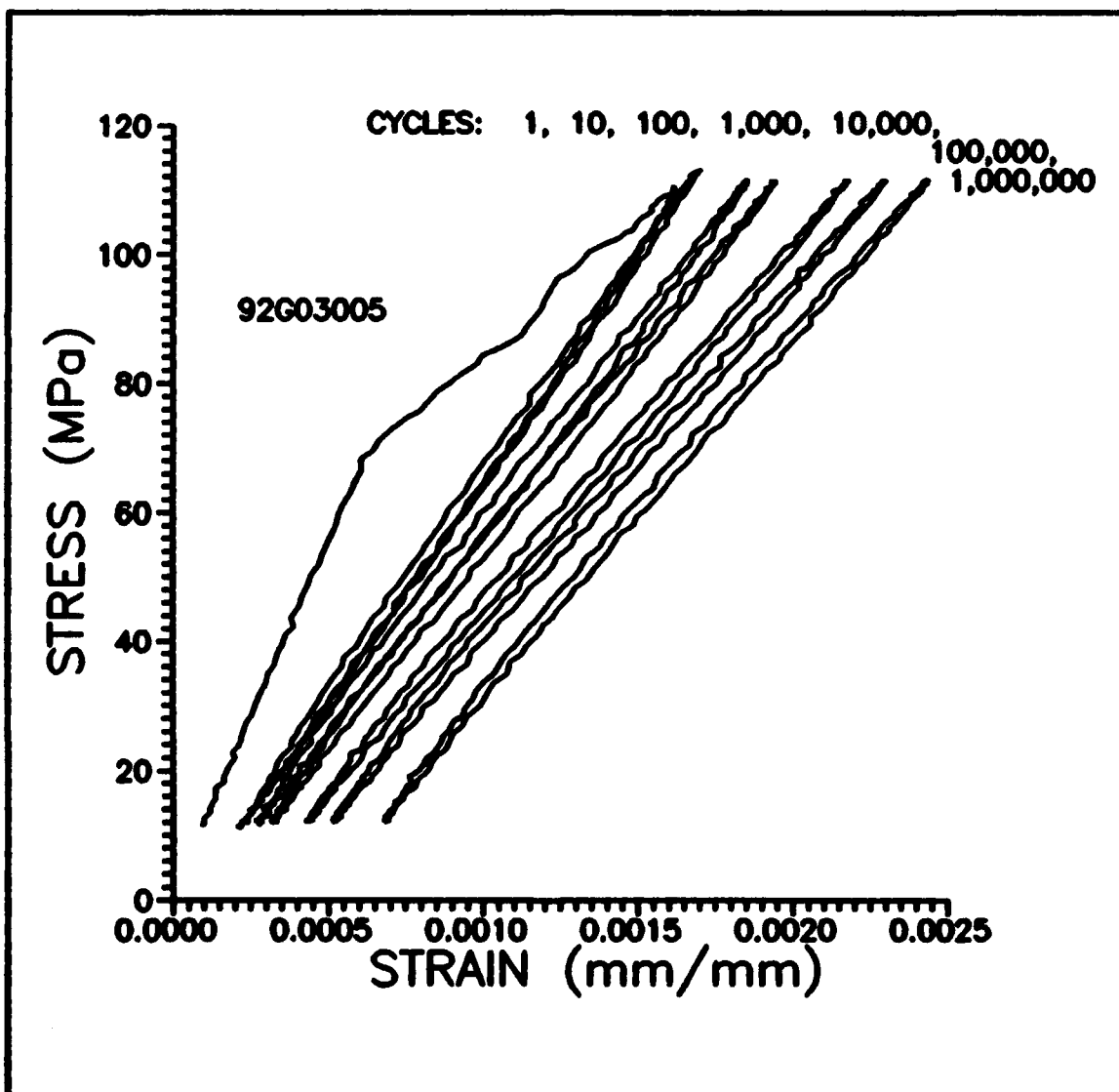


Figure 11 Tension-Tension Fatigue Stress-Strain Curves

Figure 12 shows the normalized stiffness (stiffness at the n^{th} cycle / stiffness at cycle one) versus the number of cycles. This curve also indicates that most of the damage happens in the first cycle. The stiffness decreases gradually until 100,000 cycles after which it essentially levels off.

The curve in Figure 13 reinforces the observation that the largest proportion of damage occurs in the first cycle. The hysteretic energy density was found by taking the area within the hysteresis curve and dividing it by the cross sectional area and the extensometer gage length. The first cycle has a relatively large hysteretic energy density. The hysteretic energy density levels off by five cycles at a fairly low value. The energy dissipated after cycle five is steady.

A large amount of energy is dissipated in the first cycle corresponding to a large drop in stiffness. After five cycles energy is released at a constant level. Part of this energy is used to create more damage while the remainder may be dissipated by friction at the interface of debonded fibers or crack faces. As cracks and debonds lengthen and multiply the friction increases, reducing the amount of energy available to create more damage.

The static tension stress-strain curves obtained from the present batch of material were compared to the stress-strain curves of the material used by Moschelle. On closer

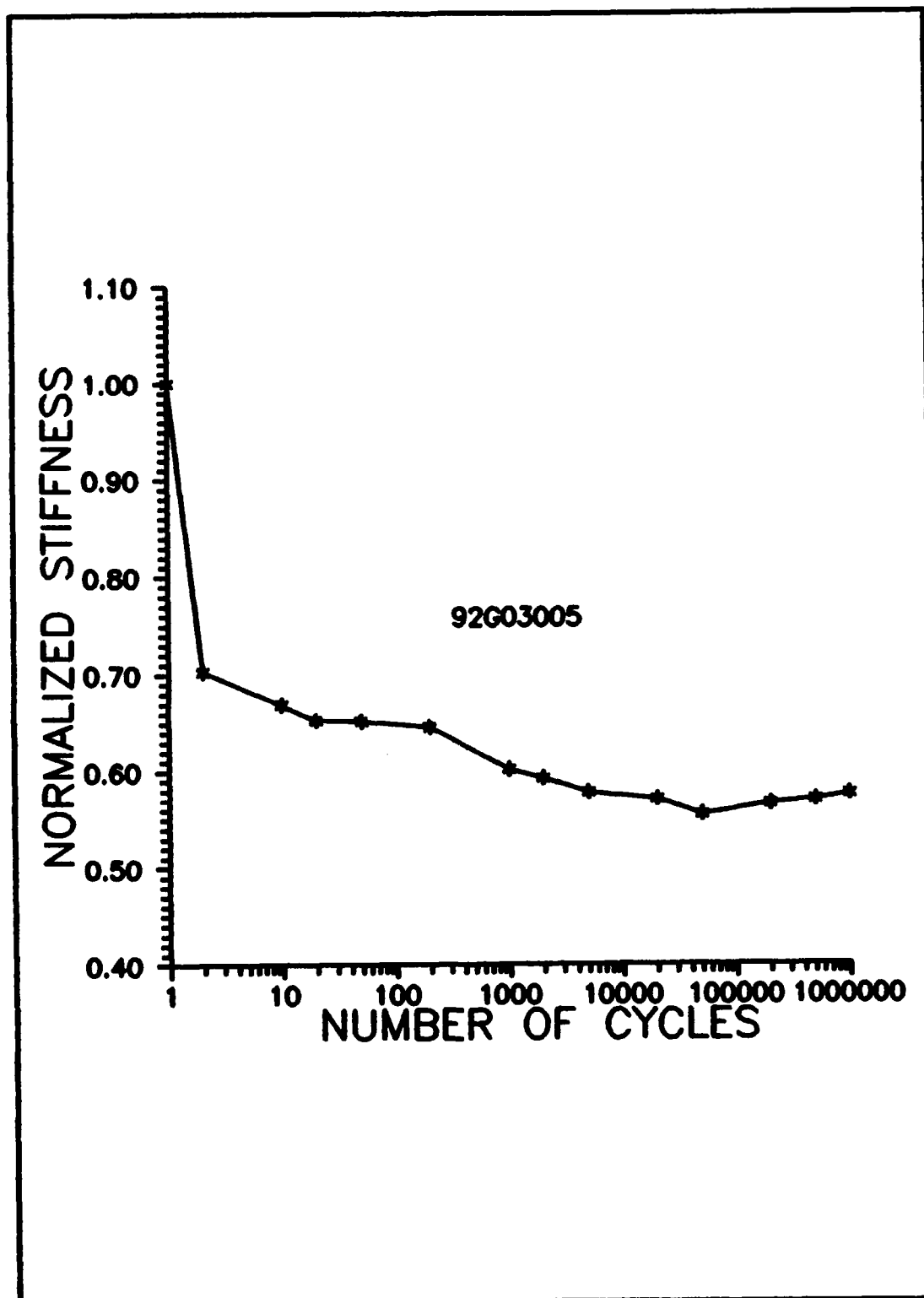


Figure 12 Normalized Stiffness Curve, 150 MPa Maximum
Stress at Notch, Tension-Tension Fatigue

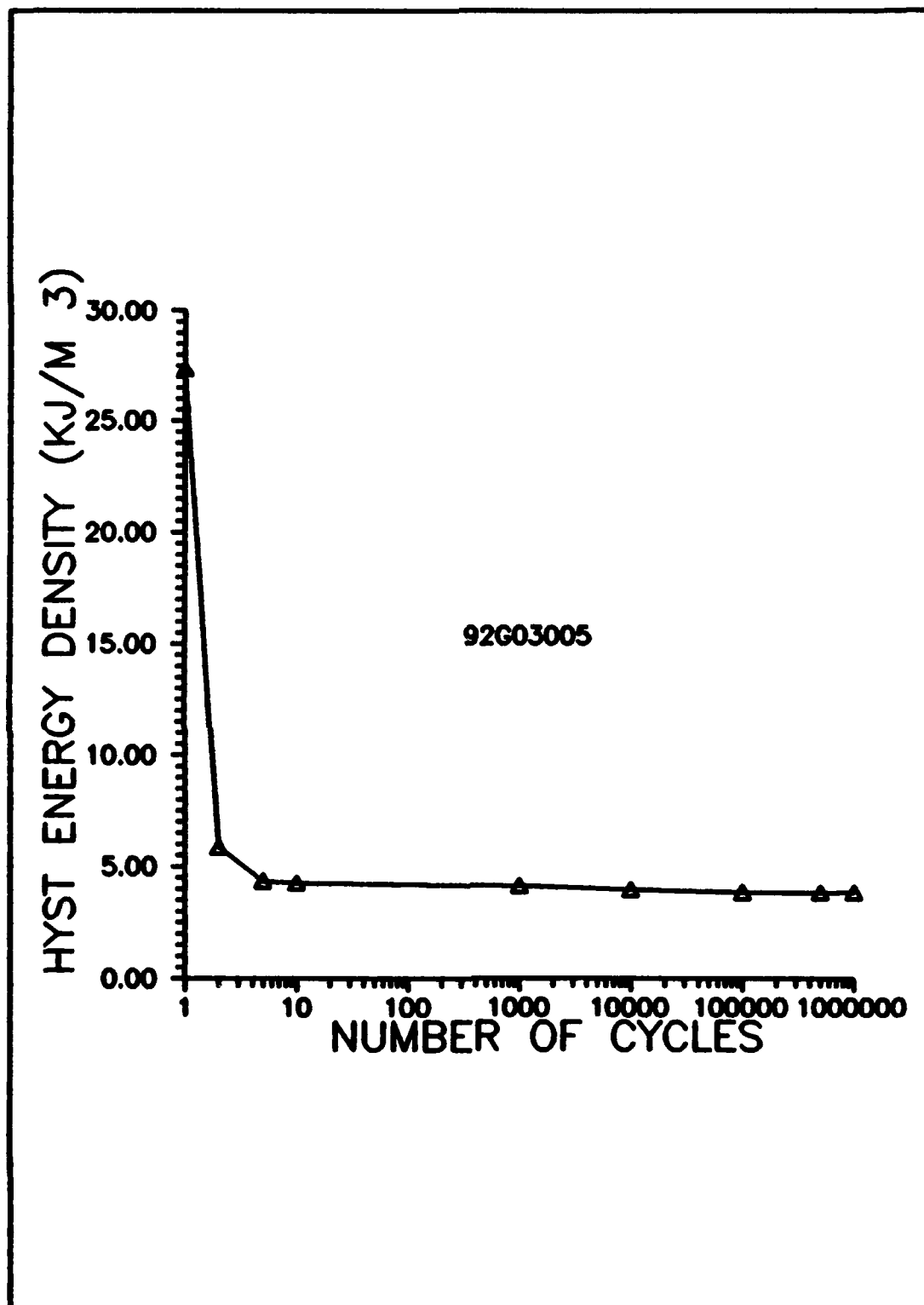


Figure 13 Hysteretic Energy Density, 150 MPa Max Stress
at Notch, Tension-Tension Fatigue

examination, it was noticed that the strain at the proportional limits and thus at the stress levels required for tension-tension fatigue runout were very close from batch to batch (Figure 14). The ultimate stress of a particular specimen is highly dependent on the production batch of the composite. The experimental nature of this material resulted in wide fluctuations of strength from batch to batch. Since material behavior at specified strains, up to the second proportional limit, was very predictable, stress levels at particular strains are better determinants for finding the fatigue limit of a specimen than are percentages of the ultimate strength.

Two plates were used for these tests so it was necessary to perform a static tension test on each plate to ensure material properties didn't vary excessively. The stress-strain curve from the second plate was very close to that of the first plate. These results confirm the value of testing plates from the same batch to facilitate analysis.

Once the behavior of the material in tension-tension fatigue had been established it was time to look at its behavior when cycled in compression. The static compression tests showed no damage until final fracture, therefore one would expect no damage at the relatively small compressive loads required to be comparable with the tension-tension tests. Indeed, this was the case as can be seen in Figures 15-17. Specimen 92G04011 was cyclically tested from -150

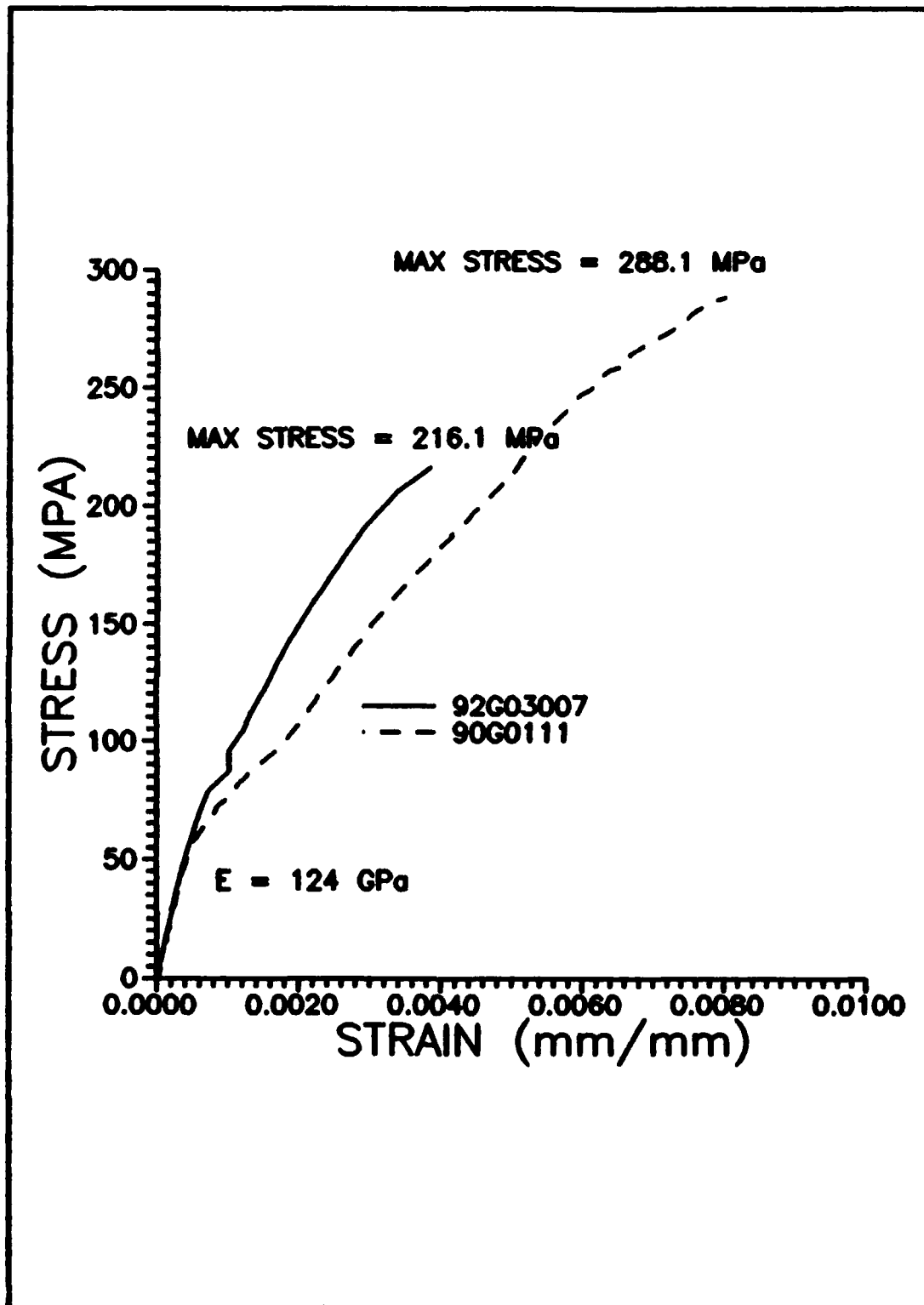


Figure 14 Comparison of Static Tensile Stress-Strain Curves for Different Production Batches

MPa to -15 MPa at 10 Hz. No decrease in stiffness was observed. Extremely small, constant values of hysteretic energy density were recorded; and no damage was observed with edge replicas throughout the test. The test was stopped at 1,000,000 cycles. Stress-strain curves are shown in Figure 15. Only the curves from one and 1,000,000 cycles are plotted for clarity. The other curves are superimposed on top of these.

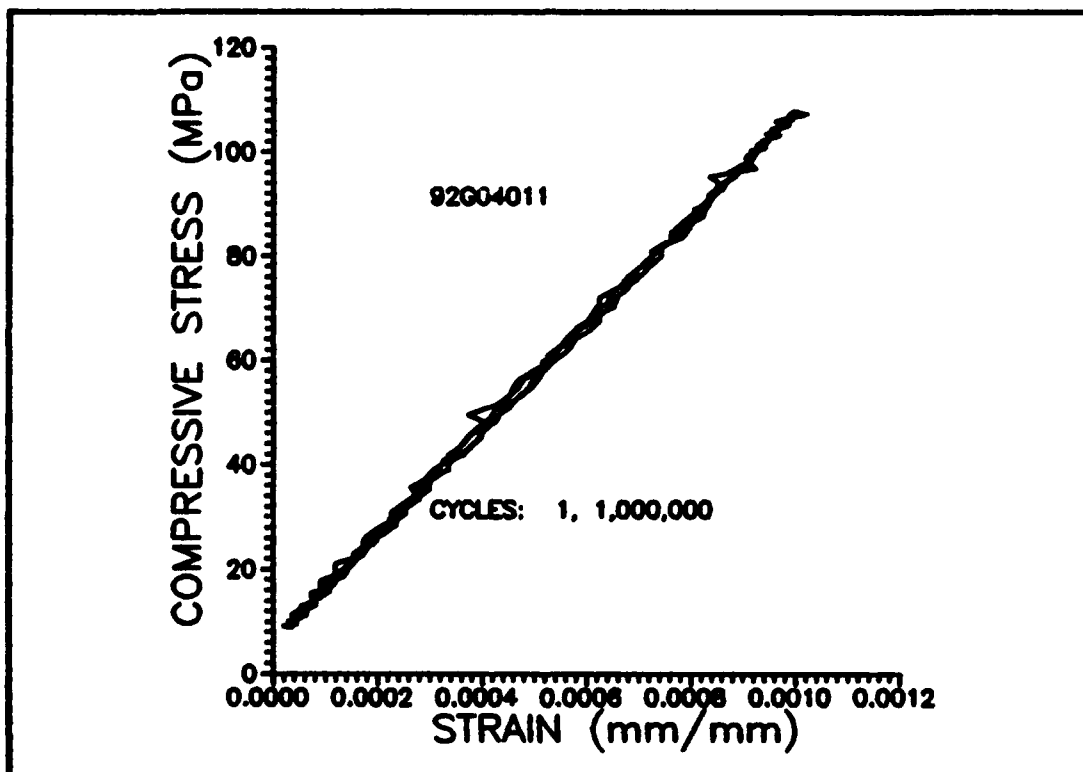


Figure 15 Compression-Compression Fatigue Stress-Strain Curves

Tension-tension fatigue causes damage even at stress levels low enough to allow runout and compression-compression fatigue causes no damage at the same stress levels. What happens when the two are put together? Zawada

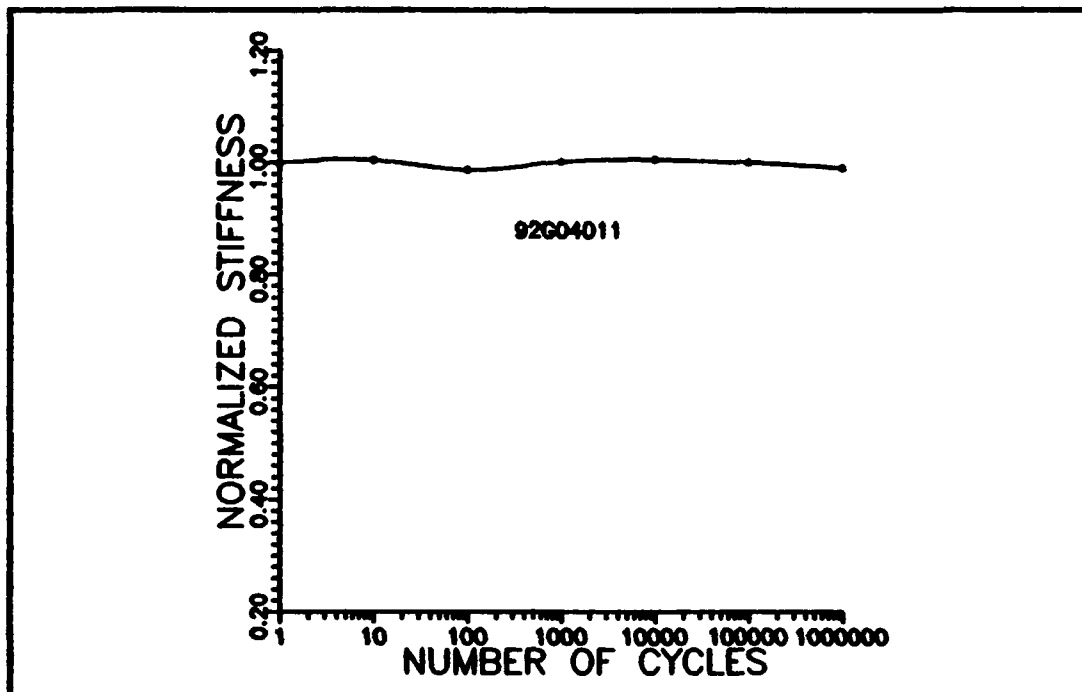


Figure 16 Compression-Compression Fatigue Normalized
Modulus

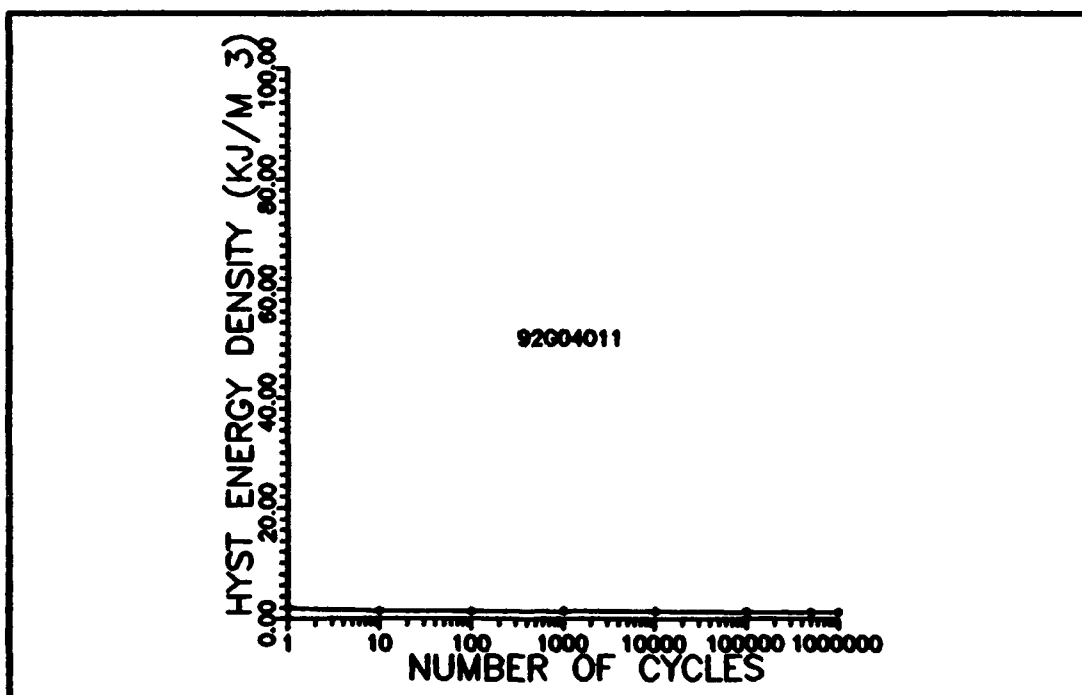


Figure 17 Compression-Compression Fatigue HED

[9] found that tension-compression fatigue of unnotched specimens resulted in continual damage accumulation. The effect of the hole seemed to have negligible effect on the cross-ply laminate in tension-tension fatigue [6] and compression-compression fatigue. Therefore, one would expect damage accumulation in the notched specimens comparable to that in the unnotched specimens when subjected to tension-compression fatigue. This will be investigated next.

A maximum notched area stress of 150 MPa was chosen for the tension-compression tests since the tension-tension and compression-compression fatigue tests achieved runout at this level. Table 4-1 is a summary of the tension-compression tests. The maximum stress given in Table 4-1 are for the notched area.

Most damage occurred early in the tension-compression tests, just as it did in the tension-tension tests. This is evidenced by the sudden drop in stiffness as shown in Figure 18. The stiffness reduction slowed and then reversed itself slightly. At this point the specimen would either break or have a rapid decrease in stiffness just prior to failure. As expected, the stiffness decreased to an overall lower value when the extensometer gage length included the hole than when the extensometer was away from the hole. This indicates the specimen has more damage near the hole.

The additional damage near the hole is caused by two

factors. The dominant reason is simply the reduced area and subsequent increase in stress. Another factor that plays a less significant role is the effect of the hole as a stress

Table 4-1 Tension-Compression Test Summary

Specimen Number	Width (mm)	Thickness (mm)	Max Stress (MPa)	R	Initial Modulus (GPa)	Cycles to Failure
92G03004	6.160	2.403	150	-1	113.22	304862
92G03013	6.101	2.405	150	-1	106	291795
92G04003	5.865	2.563	150	-1	110	245225
92G04001	5.715	2.555	150	-1	105.8	315753
92G03006	5.994	2.534	150	-1	106.1	362584

concentrator. This applies primarily to the 0 degree plies. As will be discussed later in the case of unidirectional specimens, radial cracks originate at the theoretical shear stress concentration locations and turn longitudinally. These cracks are retarded by the 90 degree plies and do not go through the thickness. They do not cause the failure but they do affect the shape of the fracture surface.

Zawada and Butkus [8] suggested the slight rise in stiffness near the end of the specimens life is caused by a combination of several possible events. Perhaps the frictional sliding coefficient of the debonded fibers

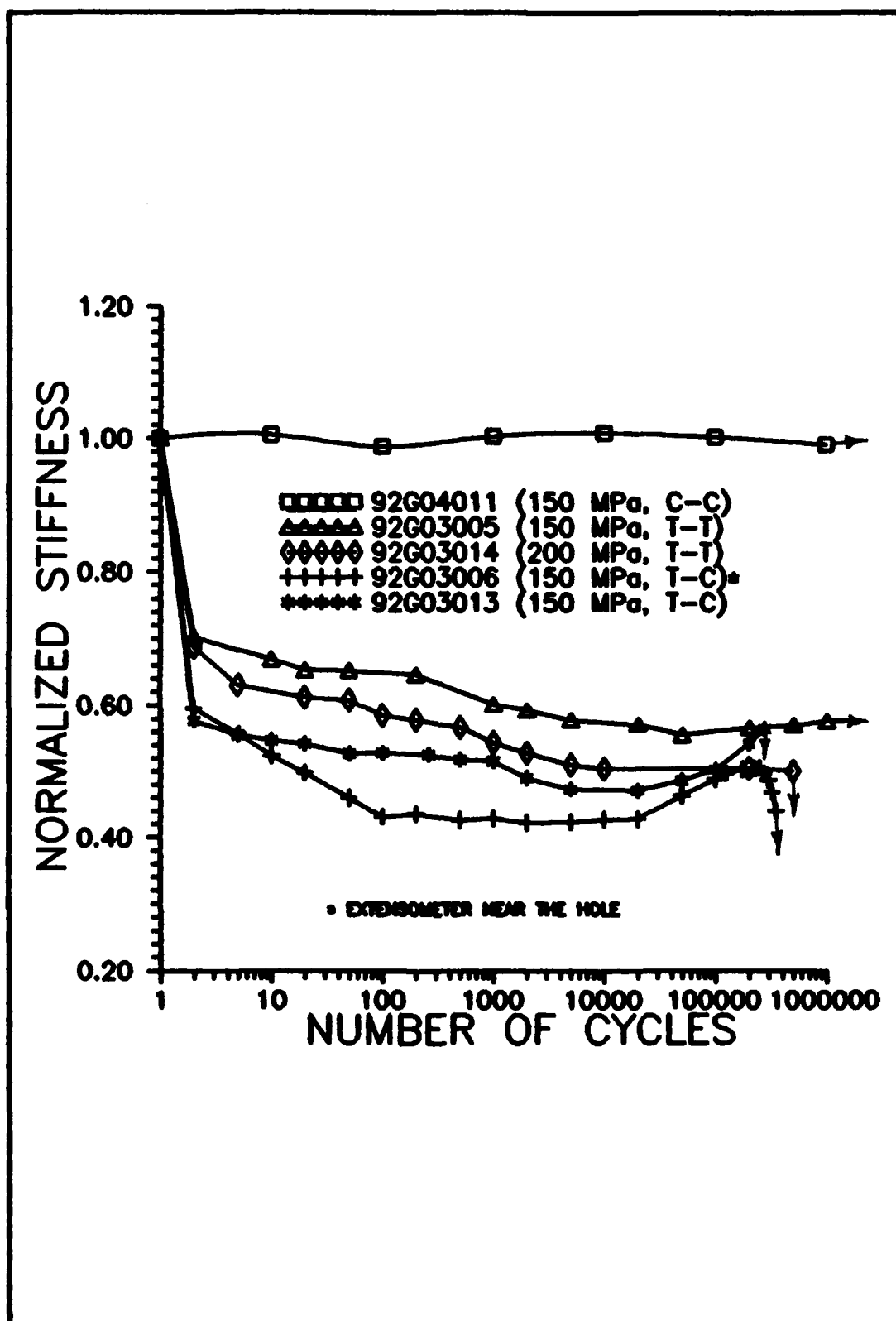


Figure 18 Normalized Stiffness vs. Number of Cycles

increases as the debond length increases; or the debonded fibers may have realigned themselves into a stiffer orientation. Or during cycling, the crack faces may fret, causing debris and prohibiting full crack closure during unloading. Video of the fatigue process seems to support the first and third possibility more than the second.

Unlike the tension-tension test at 150 MPa, damage continued to accumulate throughout the tension-compression test. The hysteretic energy density graphs (Figure 19) show this even more clearly than the normalized stiffness variations. Looking at the case where the extensometer is away from the hole, the first cycle has a relatively high energy density, once again supporting the observation that a greater proportion of the damage occurs in the first cycle. The density for the remaining cycles is lower but still high compared to that of the 150 MPa tension-tension and compression-compression tests indicating significantly more damage is taking place. In fact, the HED after the first cycle is very close to that of the tension-tension specimen tested at 200 MPa which failed at 64,000 cycles. Each of the failed specimen's energy densities begin to increase just before failure, indicating an increased damage rate near the end of the fatigue life. One interesting feature of this graph is the significant dip in energy density between cycles one and ten for the specimen with the

extensometer near the hole. More investigation is required before a plausible explanation is developed.

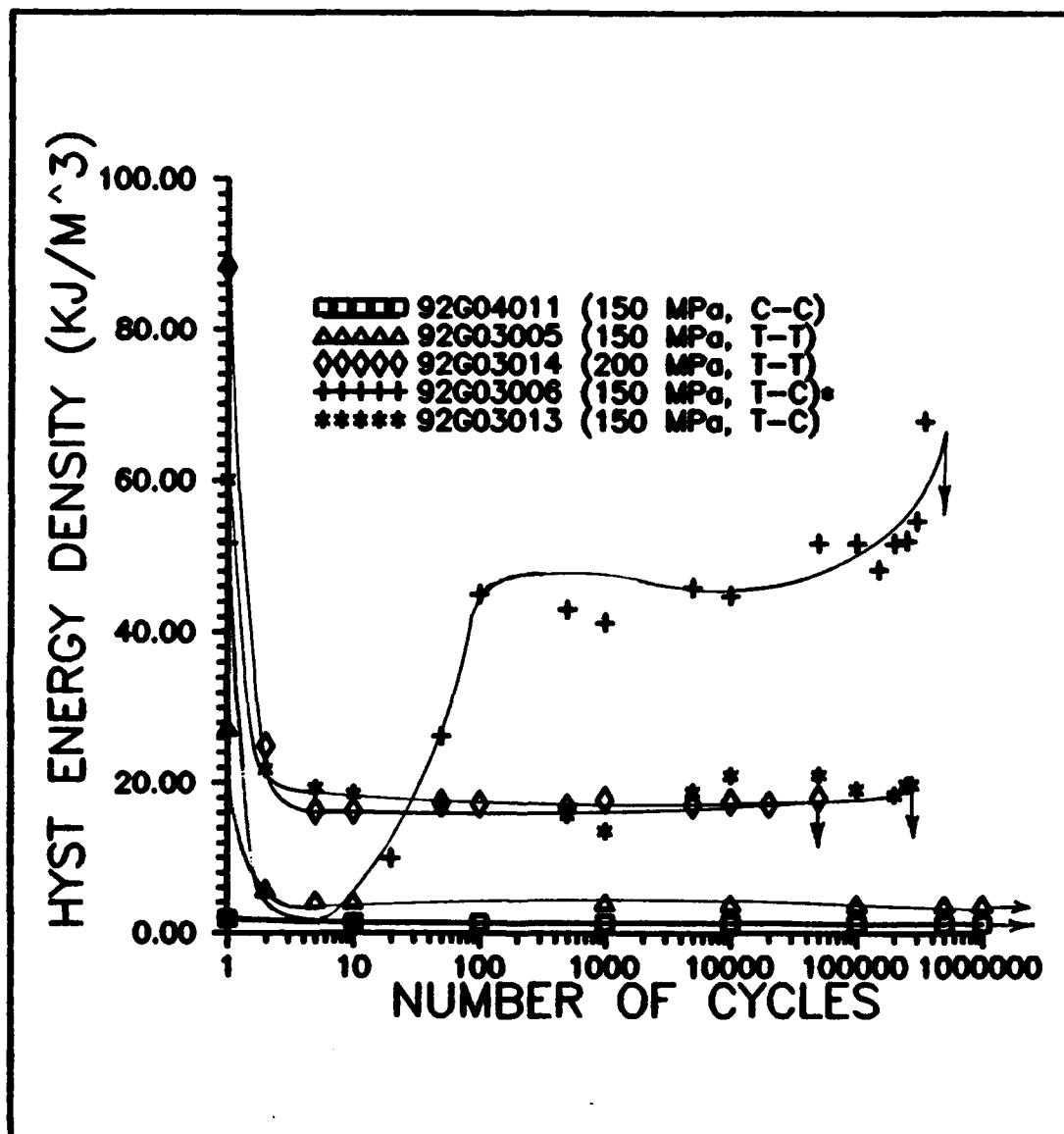


Figure 19 Hysteretic Energy Density vs. Number of Cycles
* Extensometer Near the Hole

Figures 20-22 show stress-strain curves for a failed tension-tension specimen, a tension-tension specimen that ran out, and a tension-compression specimen. All strains were measured away from the hole. The maximum stress given

in each curve's title is for the notched area. The actual stresses in the unnotched area are lower as can be seen by the stress-strain curves.

Many of the characteristics that were mentioned earlier for the 150 MPa tension-tension stress-strain curves apply to the other curves as well. All the curves have a nonlinearity point in cycle one that corresponds to the first proportional limit seen in the static tensile test. After cycle one the curves are nearly parallel from 0 MPa to 30 MPa, indicating that the transverse cracks are closing. There is slight nonlinearity in the compression portion of Figure 22 due to the opening of the longitudinal cracks, but the strain is less than that caused by the transverse cracks in tension.

Residual strain is usually a good indicator of permanent damage and when comparing the two cases of tension-tension fatigue it works well. However, since the longitudinal cracks caused the failure in tension-compression fatigue and they have little, if any, effect on axial strain, the residual strain is not a good indication of permanent damage for tension-compression fatigue. This is supported by similar amounts of residual strain for the tension-tension and tension-compression tests at the same maximum stress level. The tension-compression specimen failed while the tension-tension specimen did not.

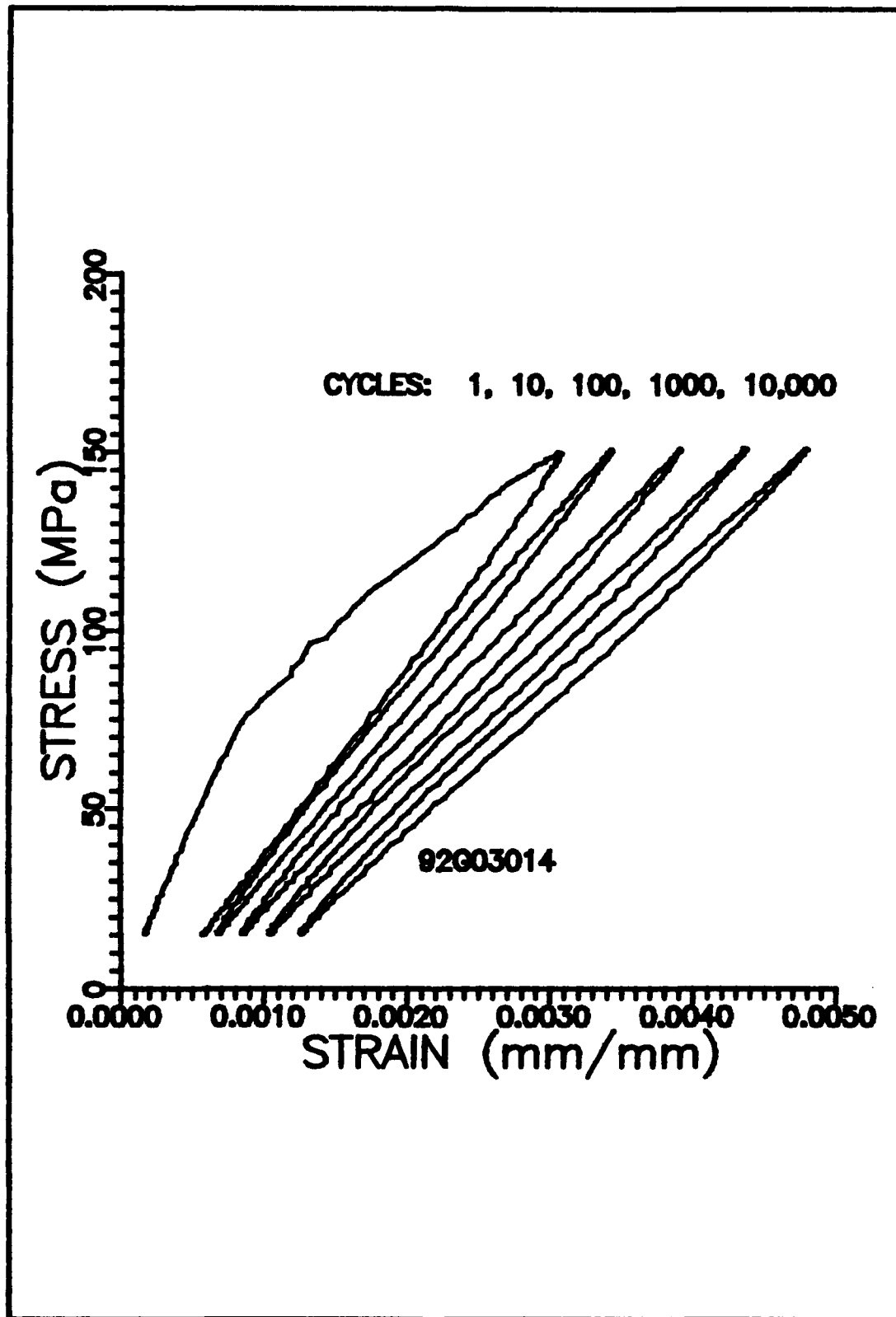


Figure 20 200 MPa T-T Fatigue Stress-Strain Curves

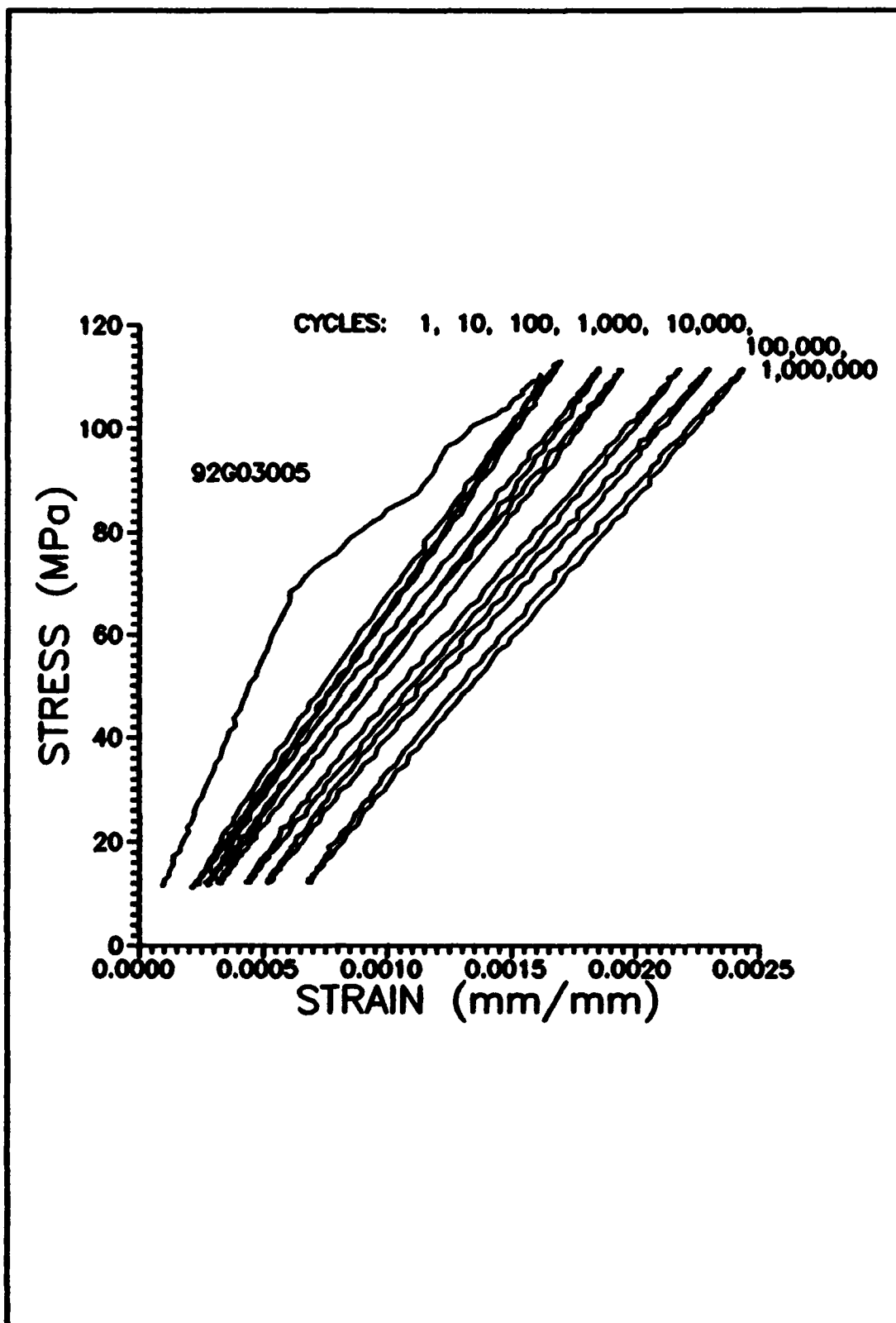


Figure 21 150 MPa, T-T Fatigue Stress-Strain Curves

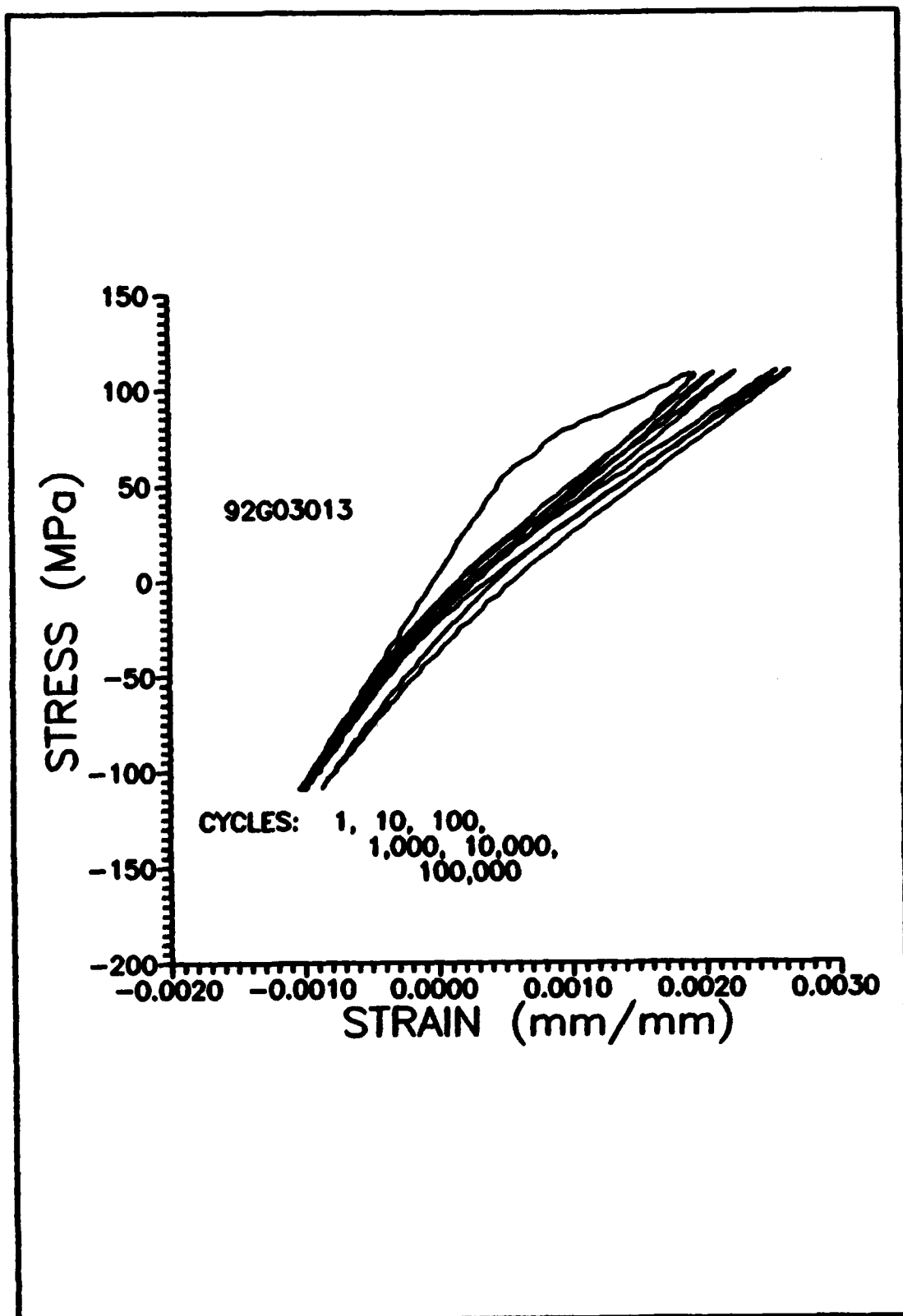


Figure 22 150 MPa, T-C Fatigue Stress-Strain Curves

Typical damage progression for tension-compression fatigue is shown in Figures 23-27. Figures 23-26 are dark field photographs of edge replicates near the hole, while Figure 27 is far from the hole. Figure 23 is a replica showing the damage after the first cycle. The patterns of damage are already fully formed. Transverse cracks have formed in the 90 degree plies and are retarded by the zero degree plies. Longitudinal cracks have formed but they haven't yet joined together.

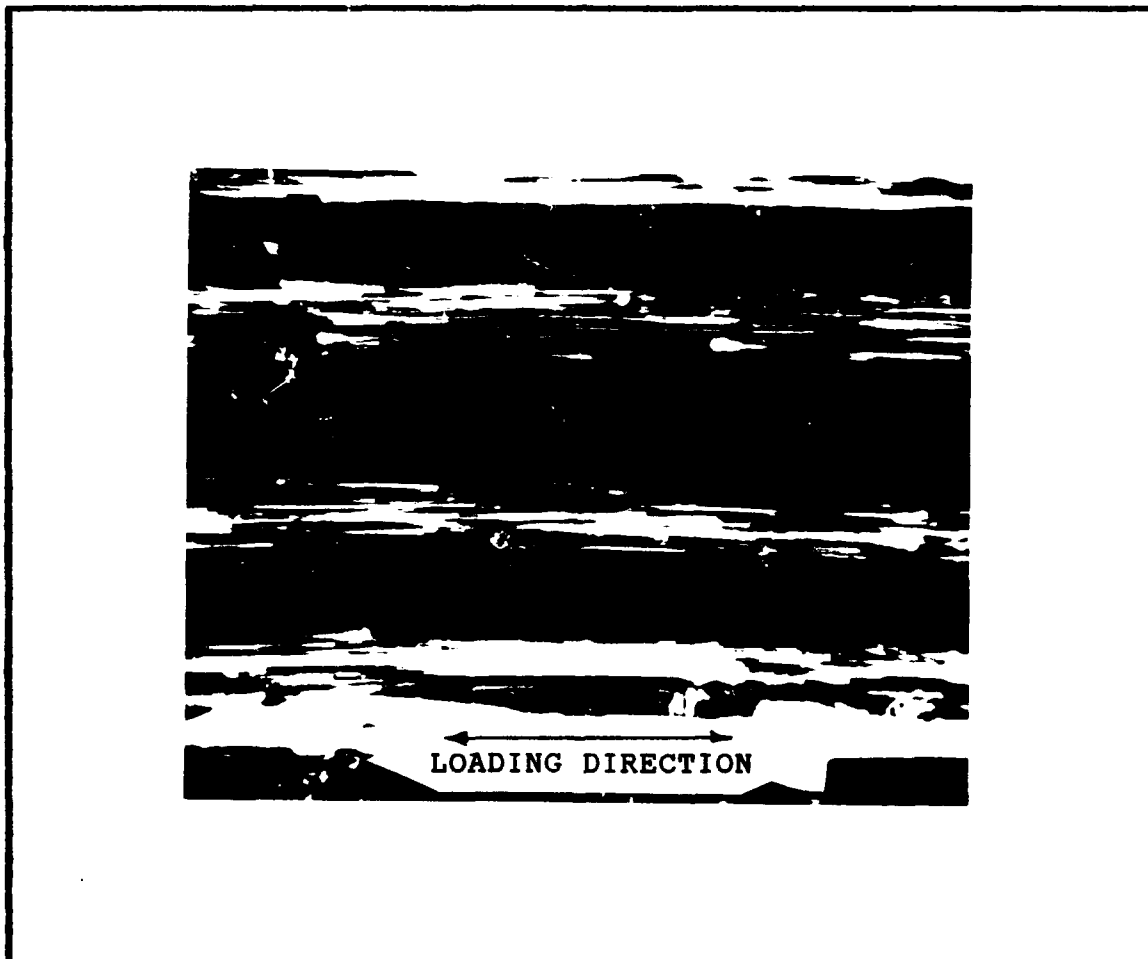


Figure 23 Typical Damage after Cycle One, 40X

In Figure 24 the transverse crack density has increased and the longitudinal cracks are beginning to join up. This is typical of the first 1,000 cycles.

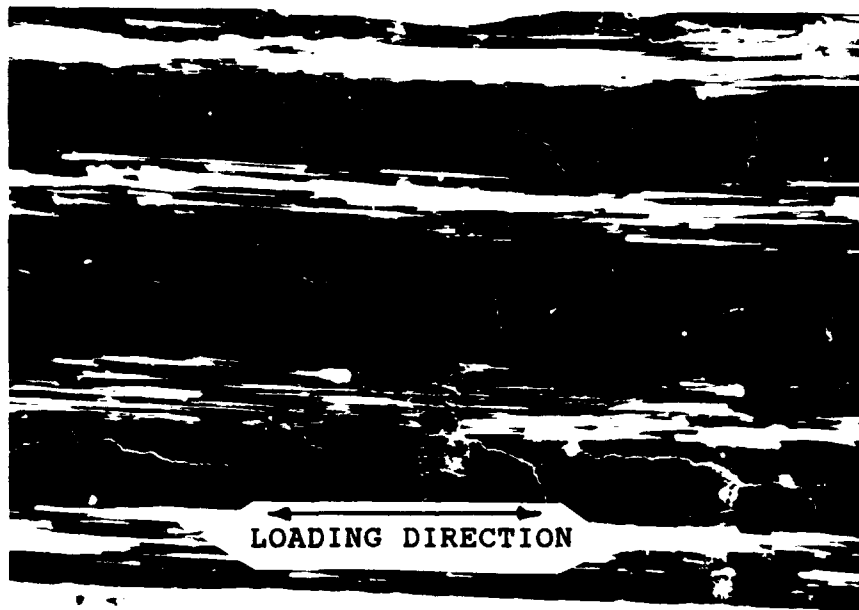


Figure 24 Typical Damage up to 1,000 cycles, 40X

By 100,000 cycles the transverse crack density has increased to its maximum level. Transverse crack spacing is approximately 50% of ply thickness. The crack density for the middle two 90 degree plies is less than for the other two, but if these two plies are considered as one thick ply, the spacing is still 50%.

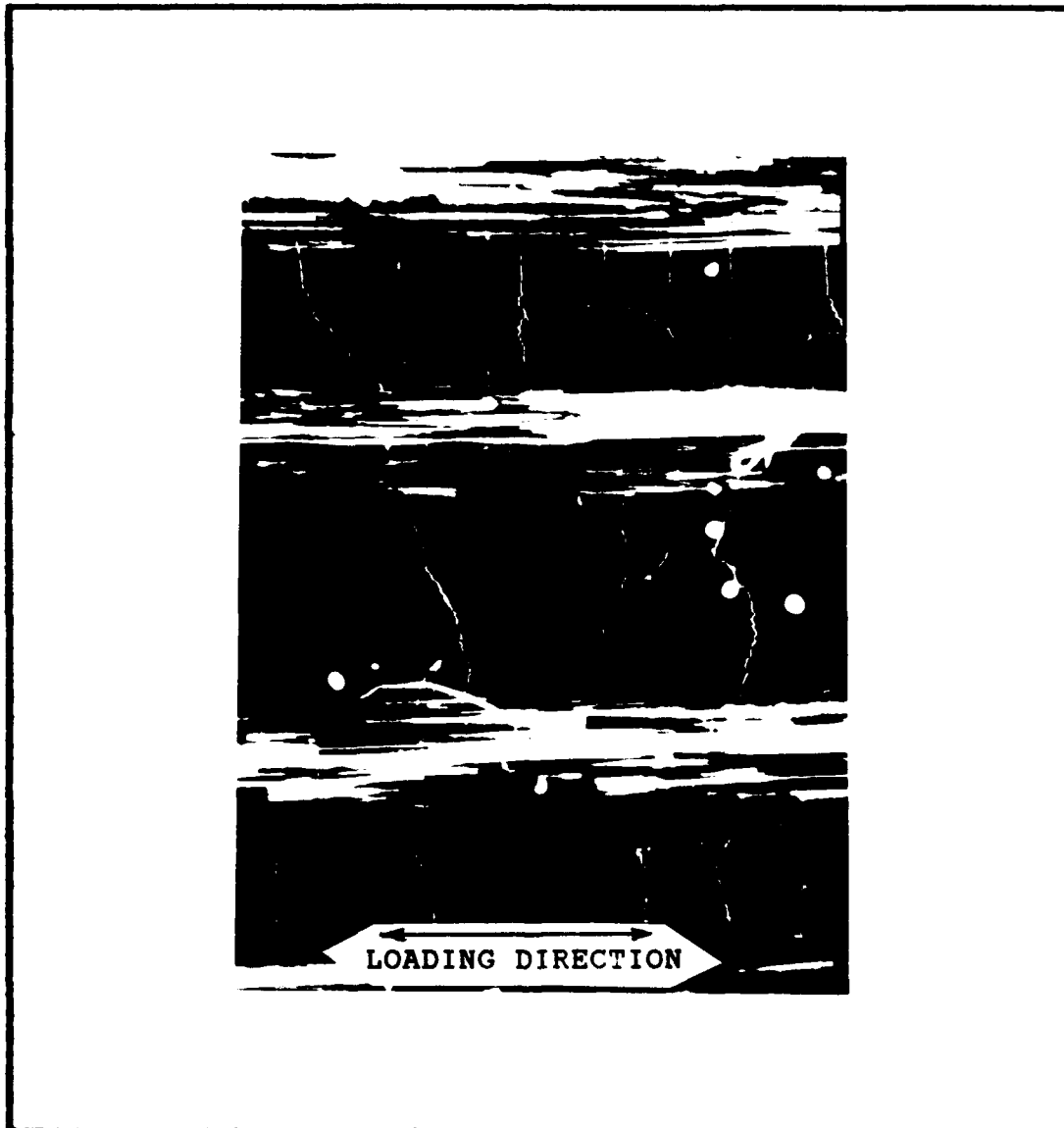


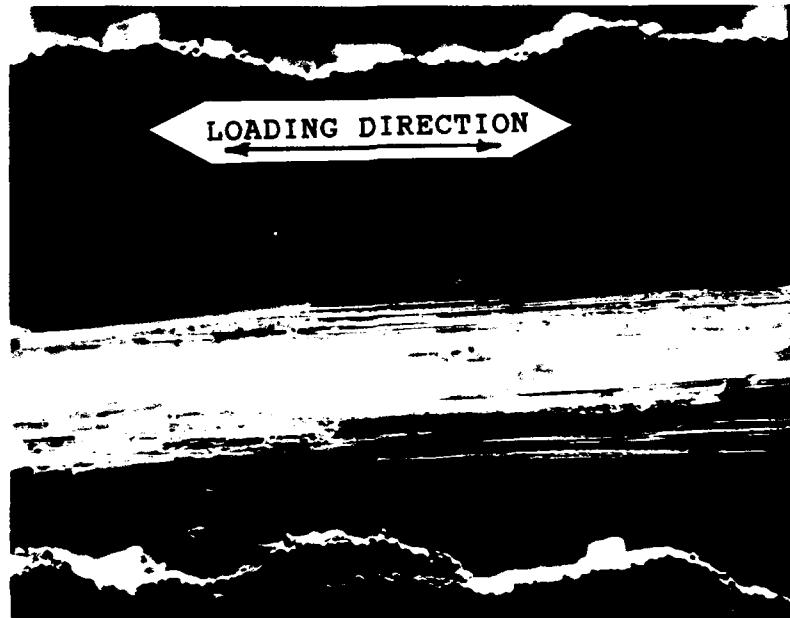
Figure 25 Maximum Transverse Crack Density, 50X

Figure 26 shows the typical crack pattern near the hole just prior to failure. Multiple longitudinal cracks have formed and have been linked by the transverse cracks. Thereby eliminating the load carrying ability of the 90 degree plies and allowing the specimen to buckle.



Figure 26 Specimen 92G04001, 300,000 Cycles, Near the Hole, 80X

Figure 27 shows the damage away from the hole at the same cycle as that in Figure 26. Damage away from the hole



**Figure 27 Specimen 92G04001, 300,000 Cycles, Far from
the Hole, 80X**

is dominated by a major longitudinal crack in the 90 degree plies with a low density of transverse cracks. This photograph confirms that more damage occurs near the hole, where the area is least.

In general, transverse cracks would open during tension and close during compression while longitudinal cracks did the reverse. This is shown in Figures 28 and 29. These are

digitized "photographs" taken from a video. Figure 28 shows the specimen in tension and Figure 29 shows it in compression.

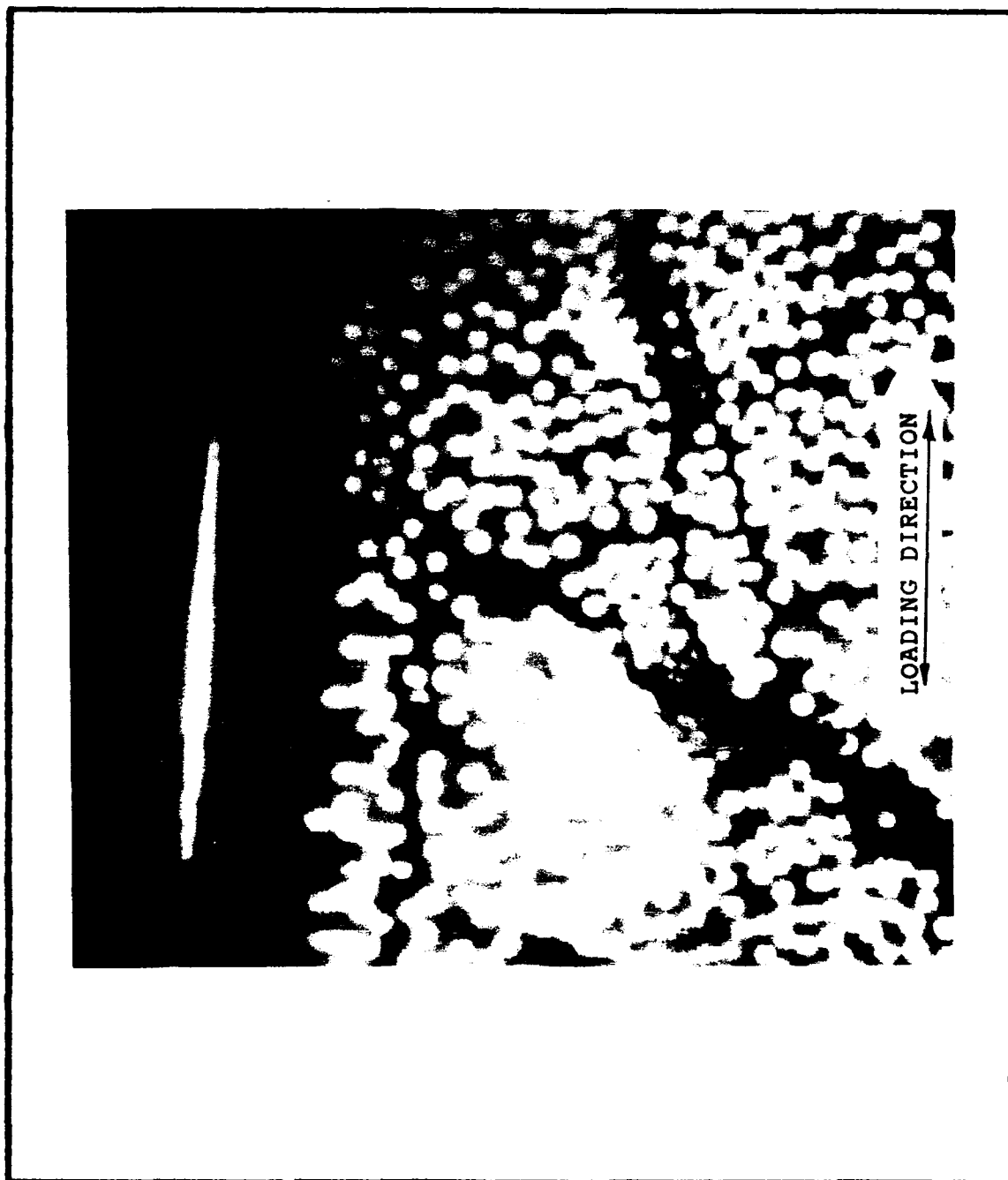


Figure 28 Specimen in Tension

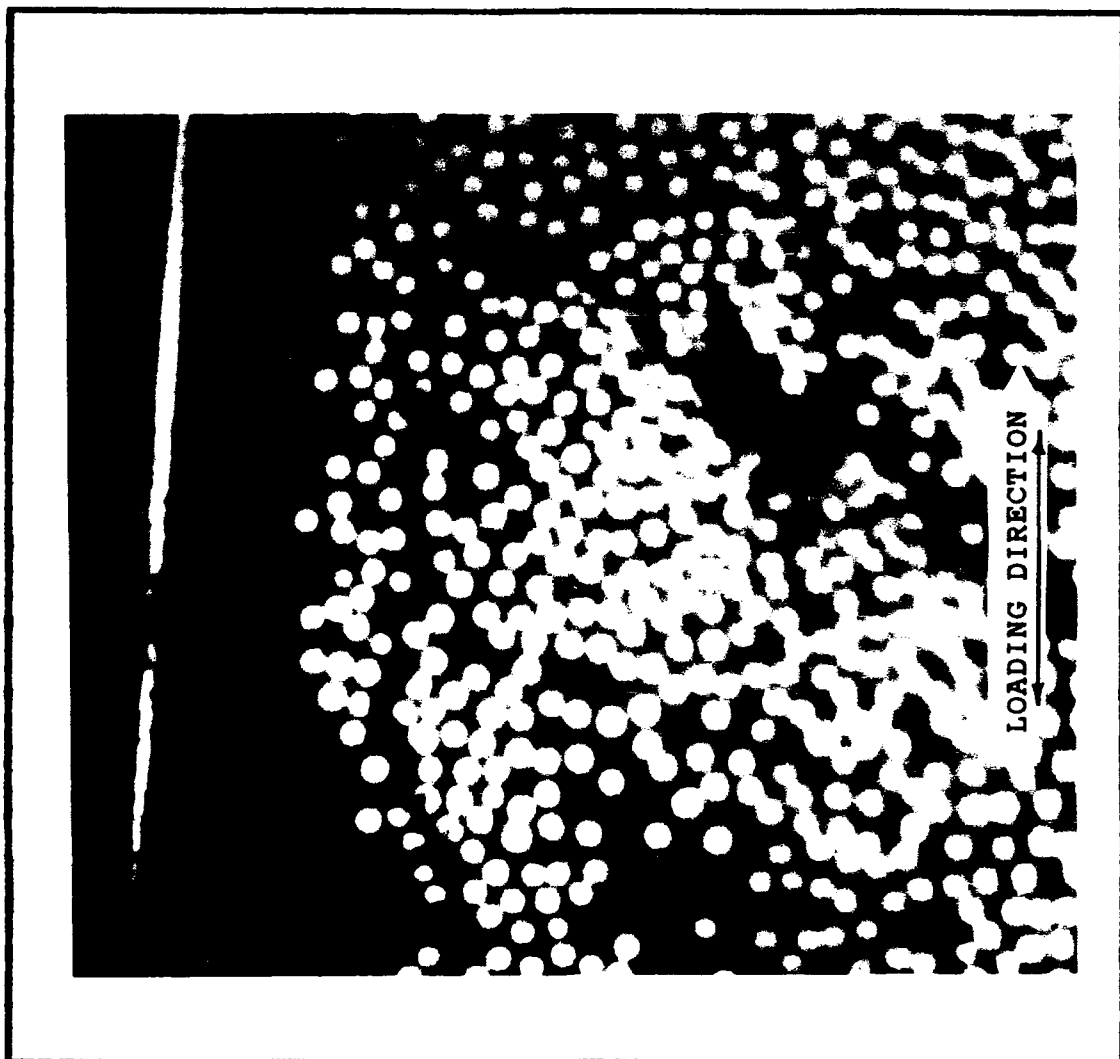


Figure 29 Specimen in Compression

The major difference between the tension-compression tests and the tension-tension tests is the continued growth of the longitudinal cracks in the 90 degree plies. Some longitudinal cracks would form in tension-tension, but they did not keep growing and their effect on the fatigue life of the specimens was negligible. In tension-compression fatigue, on the other hand, the longitudinal cracks continued to grow and eventually caused the failure.

No clear effect of the hole on failure was seen other than the reduction in the effective area of the specimen and the initiation of cracks in the specimen face. Face cracks formed at approximately 68° from the vertical in the zero degree plies as discussed in Chapter II, but the growth of these cracks was retarded and they were not the ultimate cause of failure. Figure 30 shows the typical pattern of these face cracks. They start as radial cracks at the point of highest shear stress and then quickly turn longitudinally.

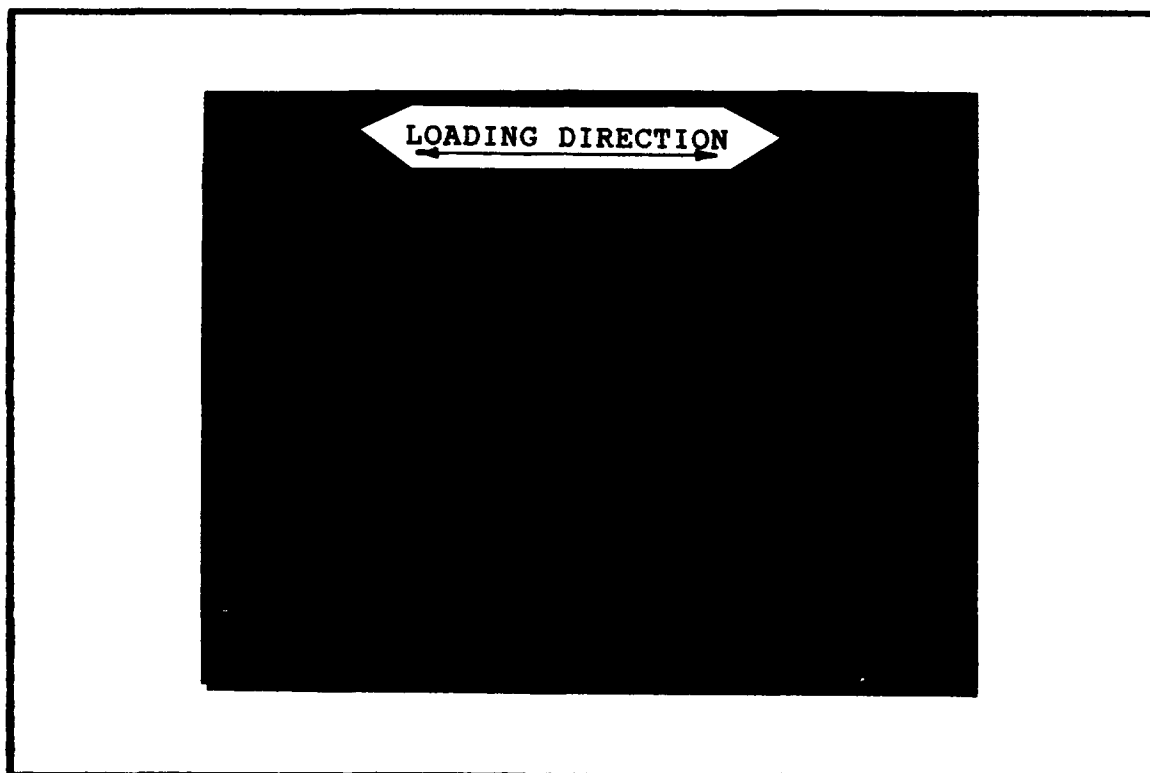


Figure 30 Face Cracks Emanating From Hole 16X

Post-fracture analysis of the tension-compression specimens was difficult since all specimens failed in compression. However, comparisons between the different types of failures can show some trends.

The photographs of the static tension failure show a large amount of fiber pullout from the 0 degree plies. The 90 degree plies have fractured due to transverse cracks. The different locations of the 90 degree ply fractures show that the transverse cracks were retarded by the 0 degree plies.

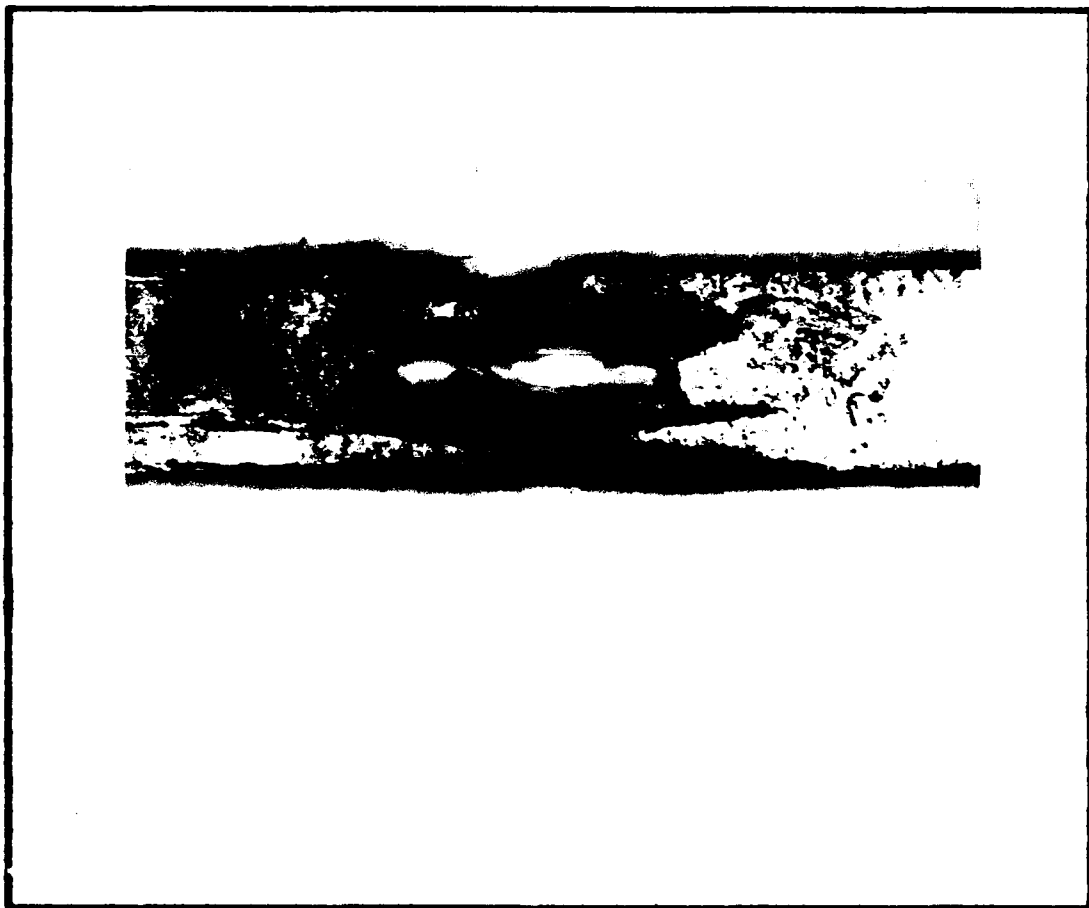


Figure 31 Static Tension Failure, Face View, 3X



Figure 32 Static Tension Failure, Edge View, 30X

The dominant feature in the static compression failure photographs is the delamination. Crushing of the specimen after failure make it very difficult to make any other definitive statements about damage at failure.

The tension-tension fatigue failure looks very much like the static tension failure with less fiber pullout. This is consistent with more damage accumulation prior to final fracture.

The tension-compression fatigue specimen failed in compression but the effects of the tensile loading are also evident. Viewing from the face the fracture surface is very similar to that of the tension-tension specimen. This

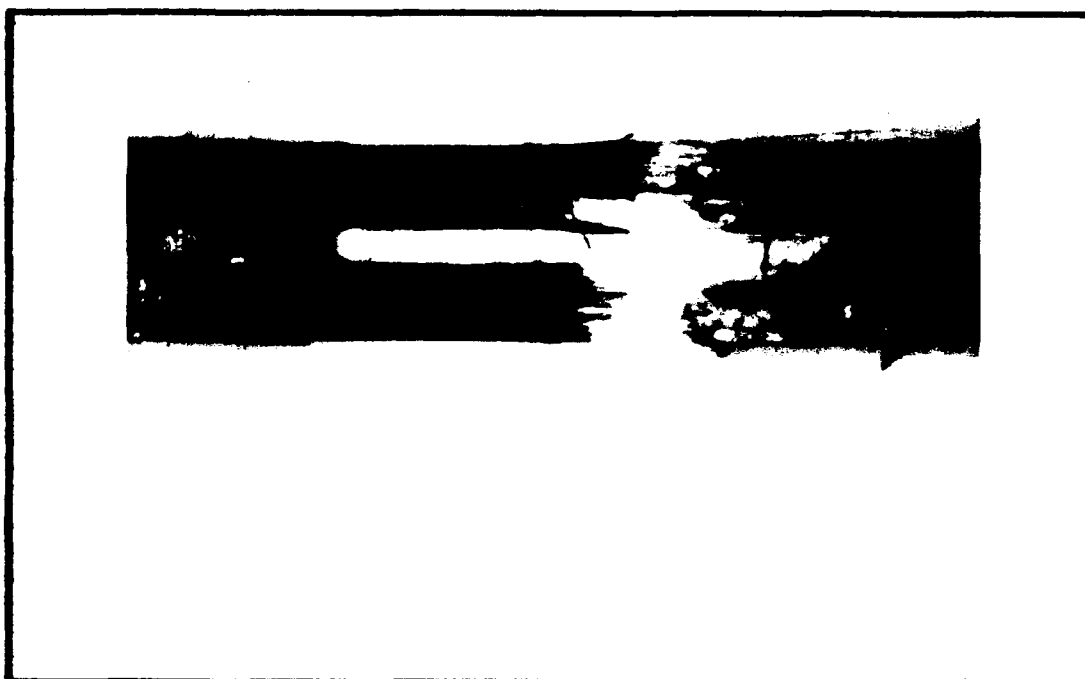


Figure 33 Static Compression Failure Face View, 2.5X

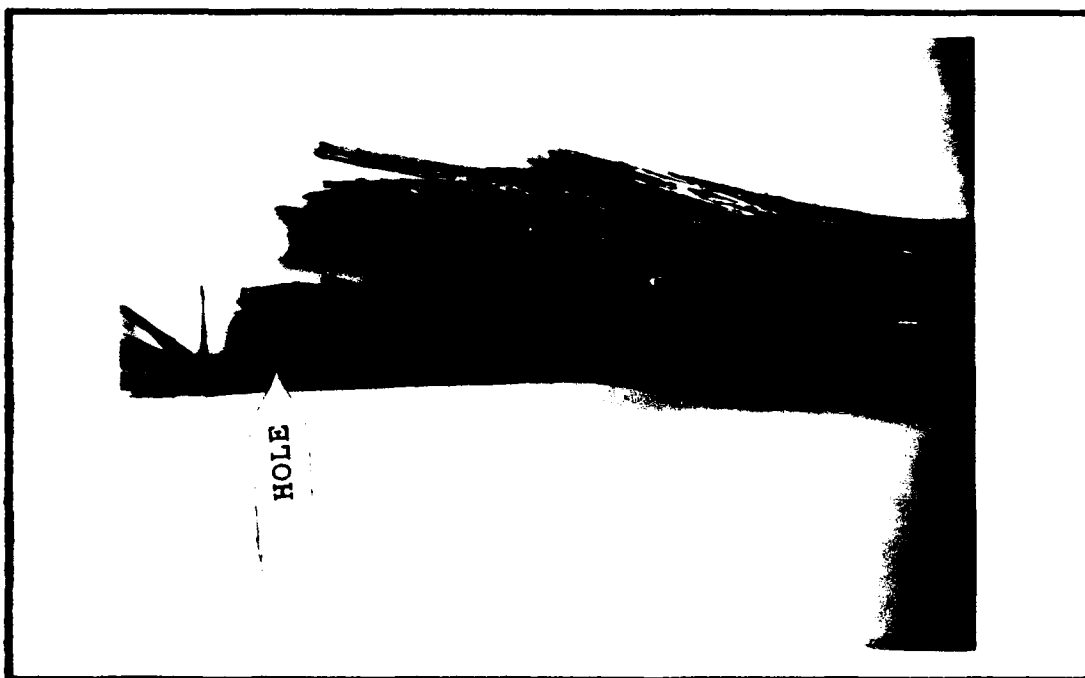


Figure 34 Static Compression Failure, Edge View, 5X

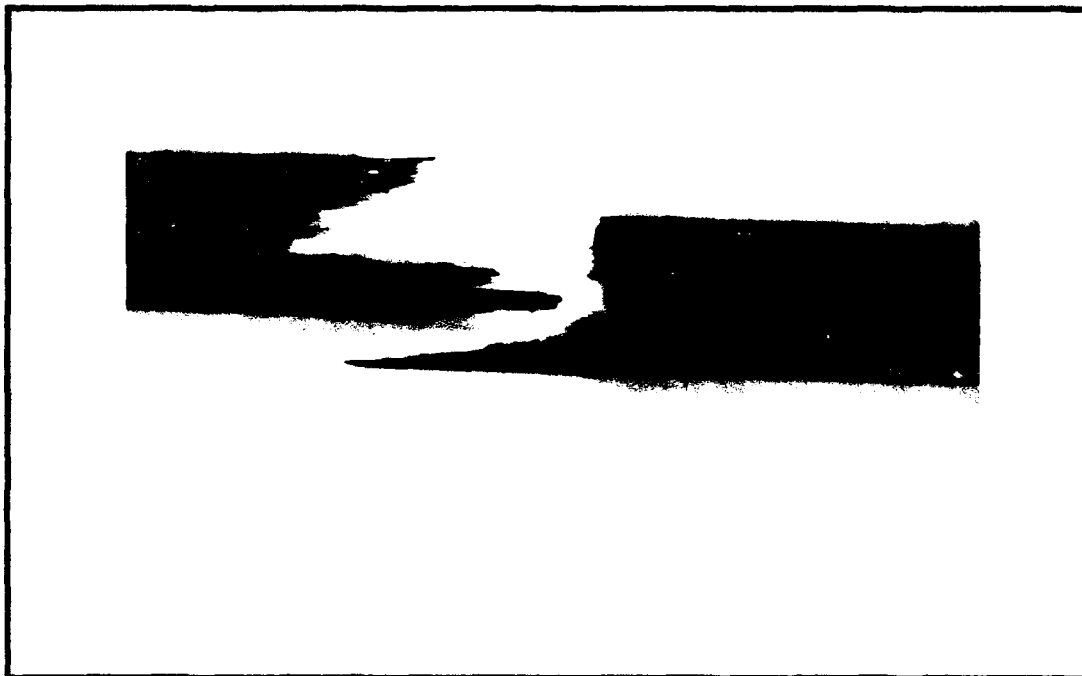


Figure 35 Tension-Tension Fatigue Failure, Face View,

2.5X

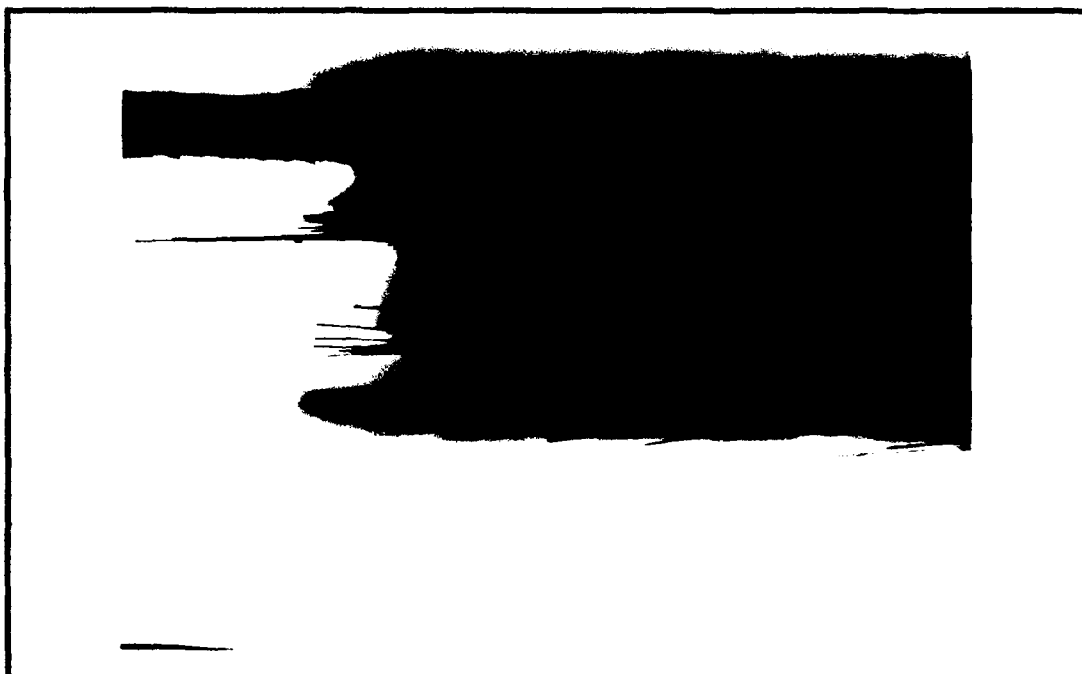


Figure 36 Tension-Tension Fatigue Failure, Edge View,

10X

indicates many of the same damage processes are taking place. The edge view, however, shows the longitudinal cracks that reduced the specimen's effective thickness and caused the buckling failure.

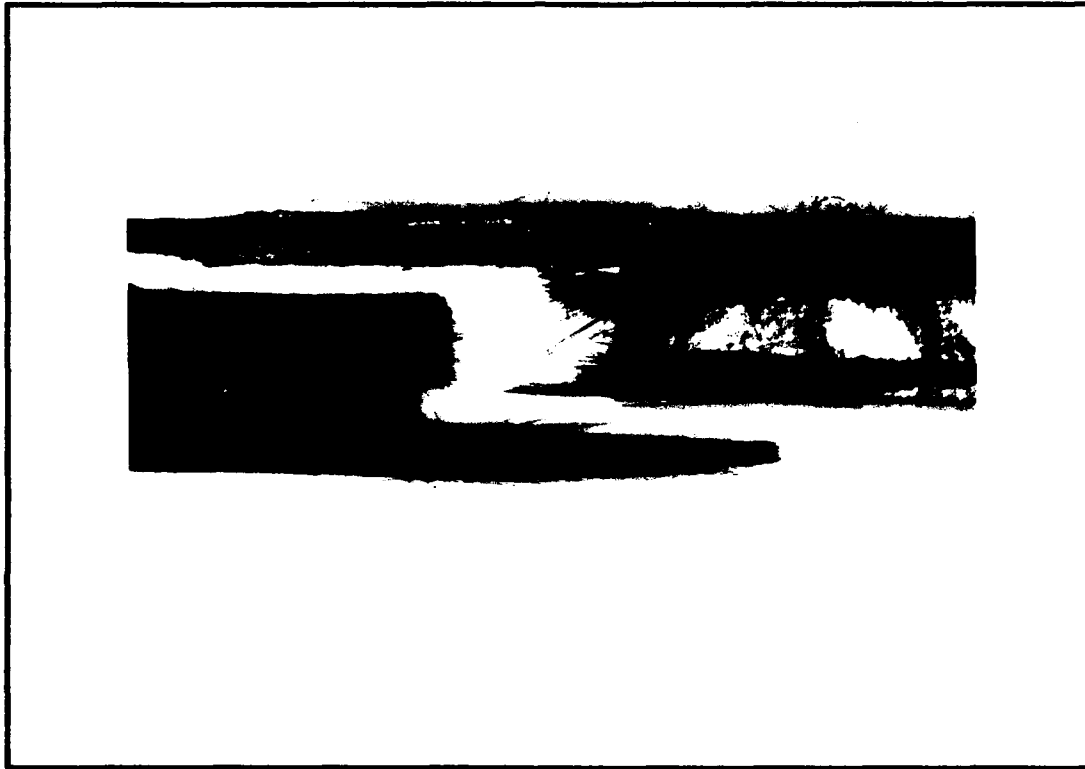


Figure 37 Tension-Compression Fatigue Failure, Face View, 3X

Tension-compression fatigue caused damage to continuously accumulate in the notched specimens just as it did for unnotched specimens. The tension-compression fatigue life of the notched specimens is not significantly different than that reported by Zawada and Pernot [9]. As such it seems that the cross-ply lay-up is insensitive to the notch in tension-compression fatigue just as it was in tension-tension fatigue.

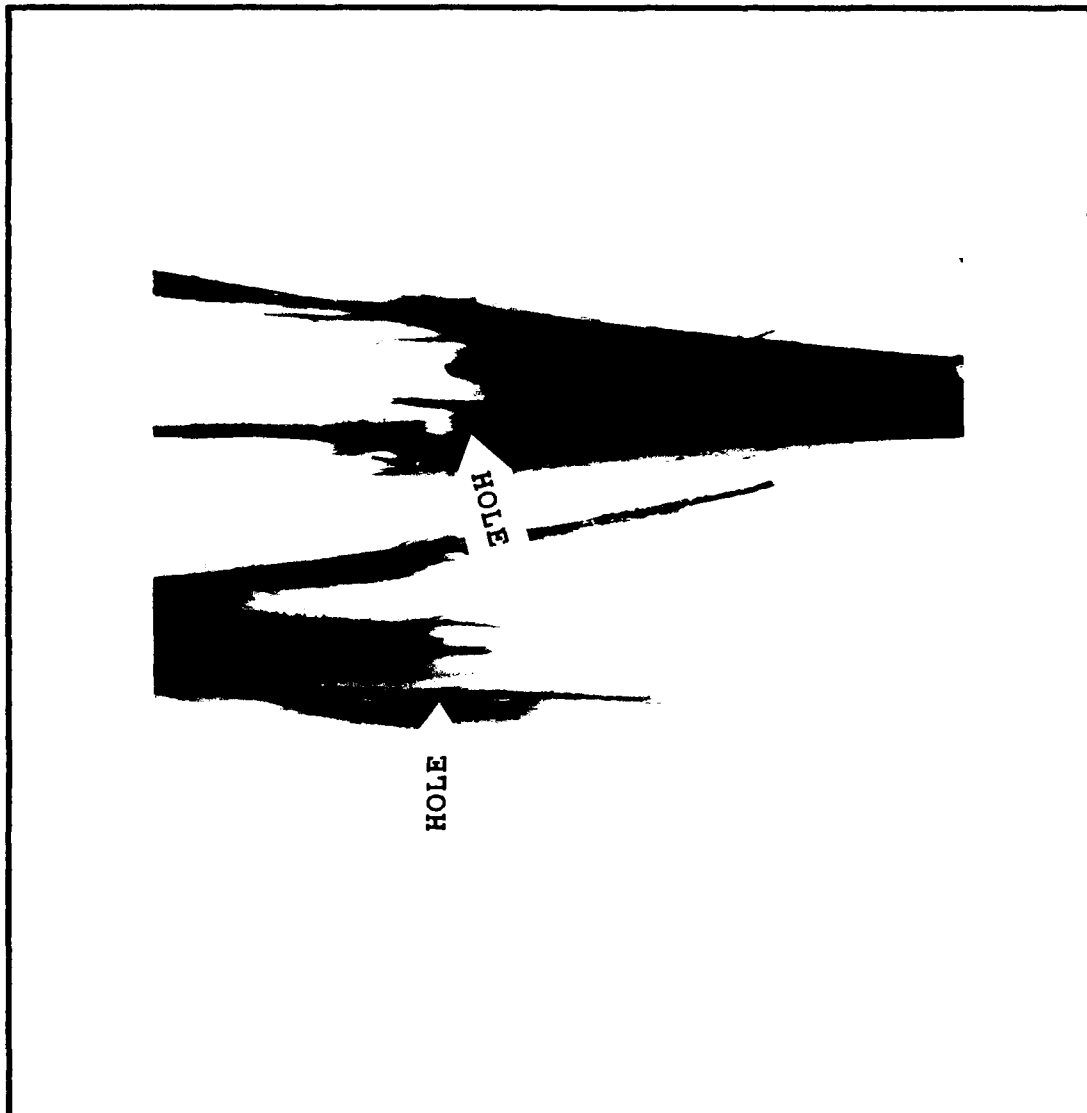


Figure 38 Tension-Compression Fatigue Failure, Edge
View, 5X

2. Analytical Comparisons

Classical laminated plate theory (CLPT) has been used previously to predict the specimen stiffness degradation limit for tension-tension fatigue [5,7]. By applying total ply discount methods they found the stiffness value, where, if the specimen stiffness remained above that value the

specimen would last 1,000,000 cycles. And if the specimen stiffness went below that value the specimen would fail.

Stiffness measurements for this series of tests were taken away from the hole for a majority of the tests. This eliminated the complicated stress and strain fields near the hole from having an effect on these measurements.

Using again the material properties for SiC/1723 from Bachmann, $E_1 = 140$ GPa, $E_2 = 88$ GPa, $\nu_{12} = 0.18$, $\nu_{21} = 0.113$, and $G_{12} = 44$ MPa, along with CLPT as described in Chapter II, one can determine the stiffness in the loading direction. The stiffness for the undamaged $[(0/90)_2]_s$ SiC/1723 laminate is 114 GPa. Totally discounting the 90 degree plies gives a stiffness of 70 GPa. If one assumes that failure occurs when the 90 degree plies have lost their effectiveness, the stiffness limit will be 61% of the original value. Looking back at Figure 18 it can be seen that this is the case. However, every case of fully reversed cyclic loading at stress levels close to the tension-tension fatigue limit had continuous damage accumulation, bringing the stiffness below the 61% limit and causing failure. Because every case of tension-compression fatigue at these stress levels failed, the usefulness of finding a stiffness limit is unclear. More investigation using a variety of load ratios and maximum stresses may identify tension-compression loading conditions where the existence of a stiffness limit will have more applications.

C. Unidirectional Specimens:

1. Experimental Results: Moschelle studied tension-tension fatigue of notched unidirectional SiC/1723 [5]. He found a clear fatigue limit and also found that the notch induced a stress concentration evidenced by cracks emanating from the theoretical maximum shear stress locations and the notched specimens having a much lower fatigue limit than unnotched specimens as reported by Zawada and Butkus [7]. One conclusion of Zawada and Butkus that Moschelle confirmed for notched specimens is that SiC/1723 specimens will show some damage in the form of matrix microcracking near or below the proportional limit and still survive one million cycles.

In the previous section it was shown that longitudinal cracks formed and grew in the 90 degree plies of the cross-ply specimens during tension-compression cycling eventually leading to buckling failure. The unidirectional specimens used for this portion of the tests had no 90 degree plies and therefore the added effect of cyclic compressive loads was unknown.

Once again a baseline was needed. A static tensile test was run with the resulting stress-strain curve shown in Figure 39. All tests with the unidirectional specimens were run with the extensometer near the hole. Unidirectional SiC/1723 only has one knee which for this batch of material

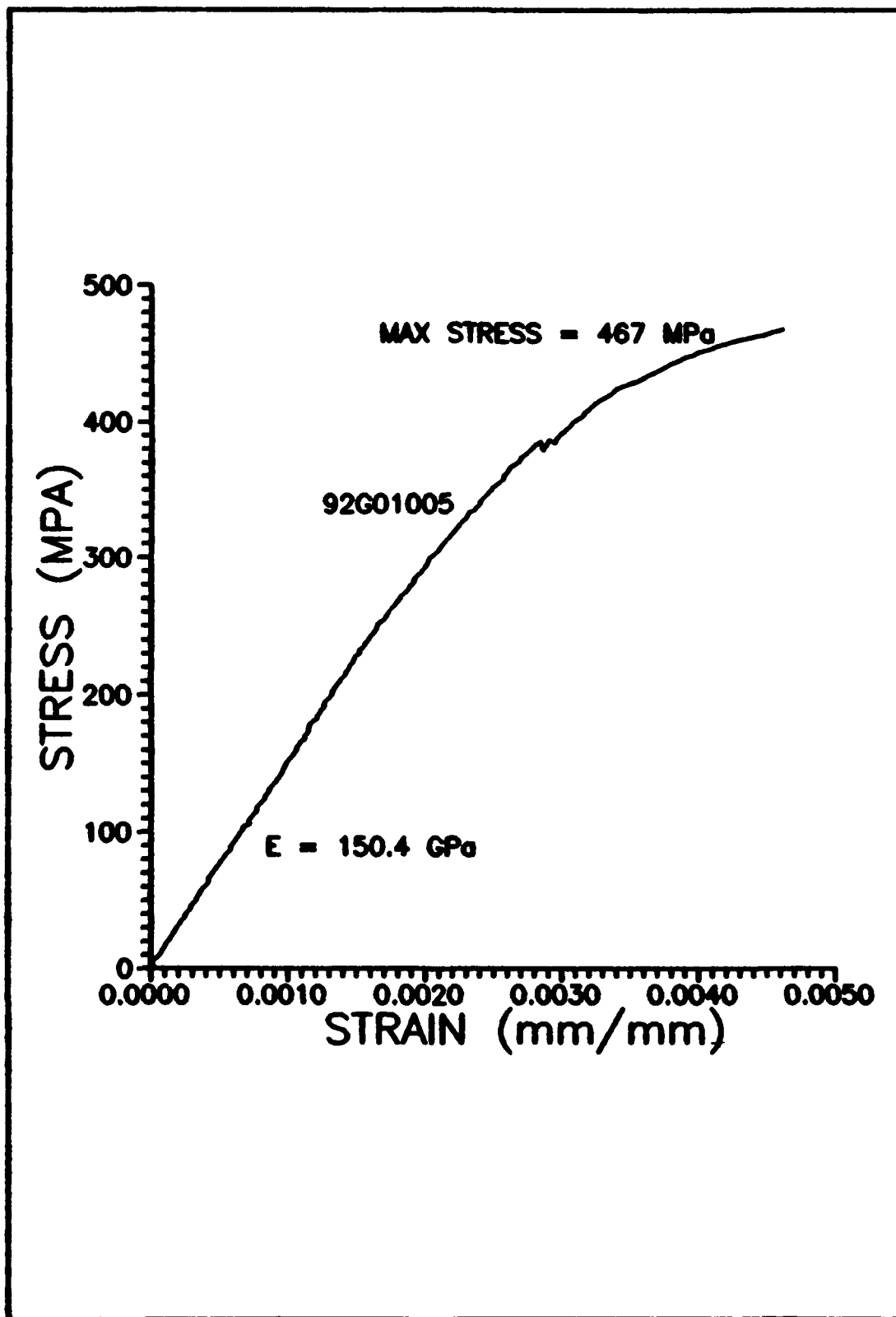


Figure 39 Stress vs. Strain, Static Tension

was at 255 MPa and 0.0017 mm/mm strain. This compares to 170 MPa and 0.0015 mm/mm strain for one of Moschelle's plates of material. A static compression test was also run with the results shown in Figure 40. Just as in the static compression test for the cross-ply laminate, the curve is linear until failure, indicating no damage occurs until catastrophic failure.

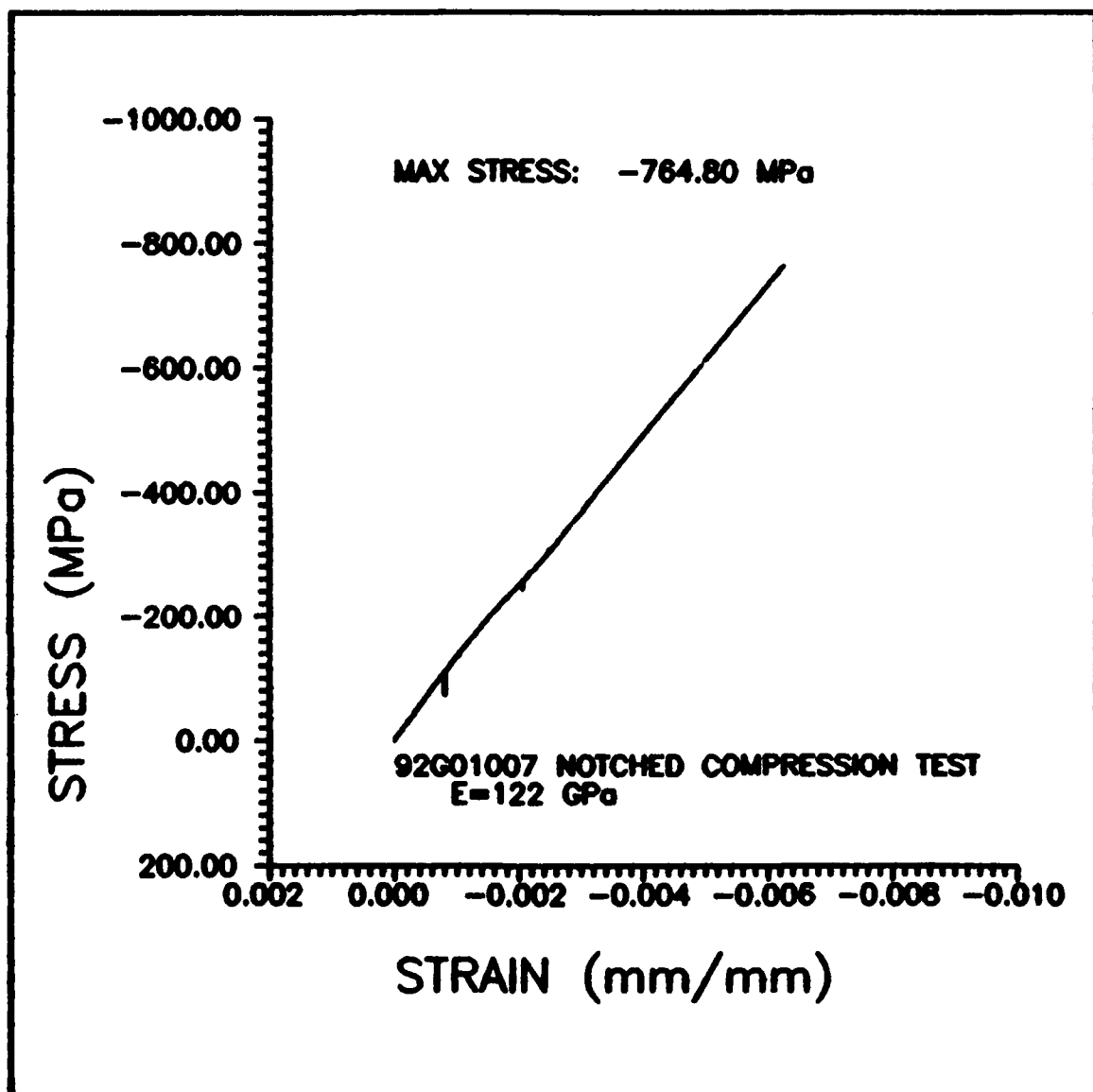


Figure 40 Stress vs. Strain, Static Compression

The previous studies showed that the fatigue limit was at the proportional limit. To verify the fatigue limit specimen 92G01004 was fatigued in tension-tension at 300 MPa maximum stress. This specimen failed at 270,655 cycles. Failure modes were consistent with those reported by Moschelle [5]. Radial cracks emanated from the hole near the theoretical stress concentration points turning into through the thickness longitudinal cracks that eventually caused failure.

MPa and achieved runout. 200 MPa was chosen because it was below the proportional limit and also below the strain value of 0.0015 which marked the proportional limit during Moschelle's tests. The stress-strain curves are shown in Figure 41. This specimen also had the characteristic longitudinal cracks emanating from the hole as can be seen in Figure 42. These cracks were very small and were not visible when the specimen was unloaded (Figure 43). Close examination of edge replicas also showed some matrix microcracking (Figure 44) but no longitudinal cracks, supporting previous studies [5, 7]. A fatigue limit had now been established for unidirectional specimens.

A compression-compression fatigue test at 200 MPa maximum stress was not run due to the similarities between the static compression curve of the unidirectional laminate with that of the cross-ply lay-up and the limited amount of

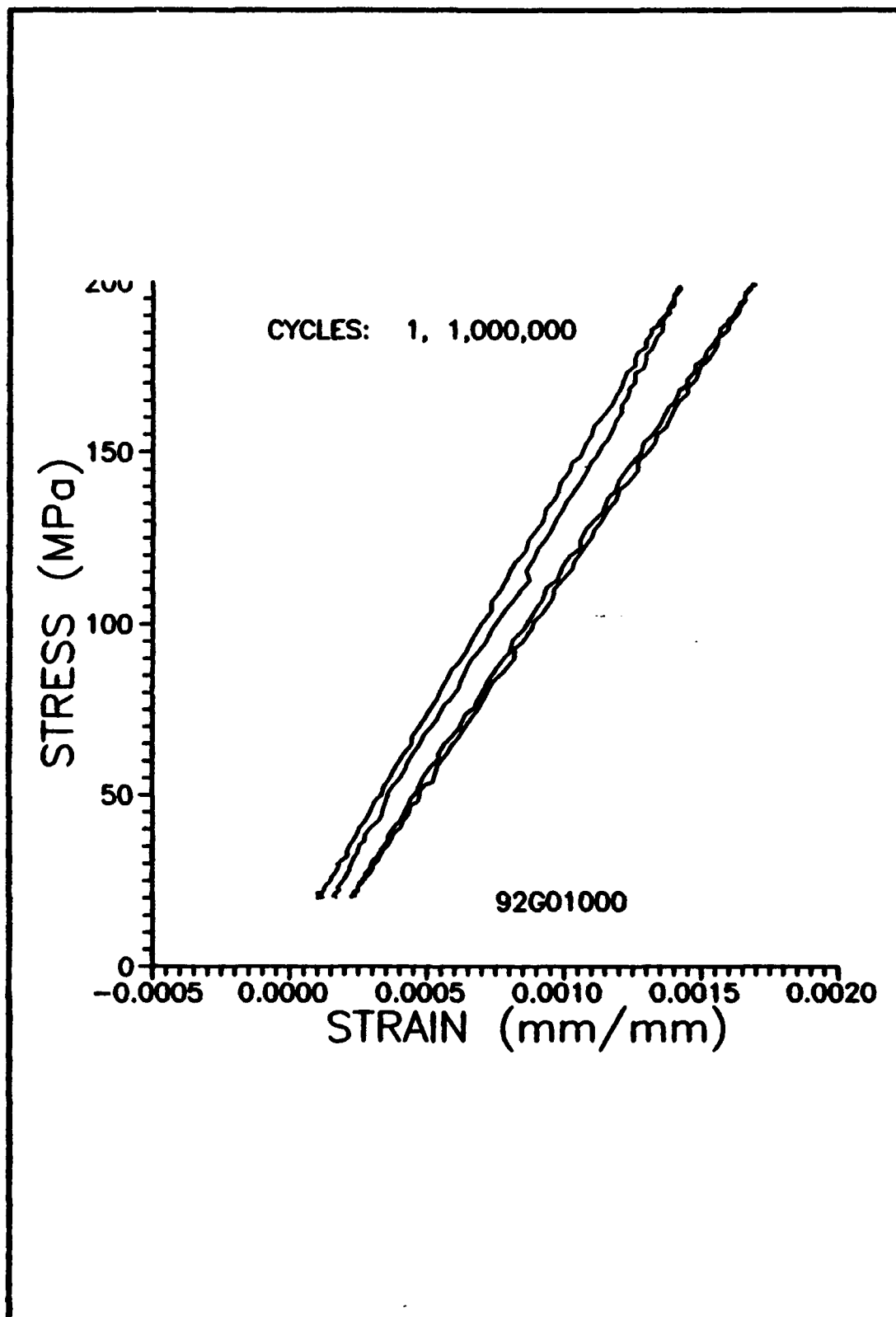


Figure 41 Tension-Tension Fatigue Stress-Strain Curve

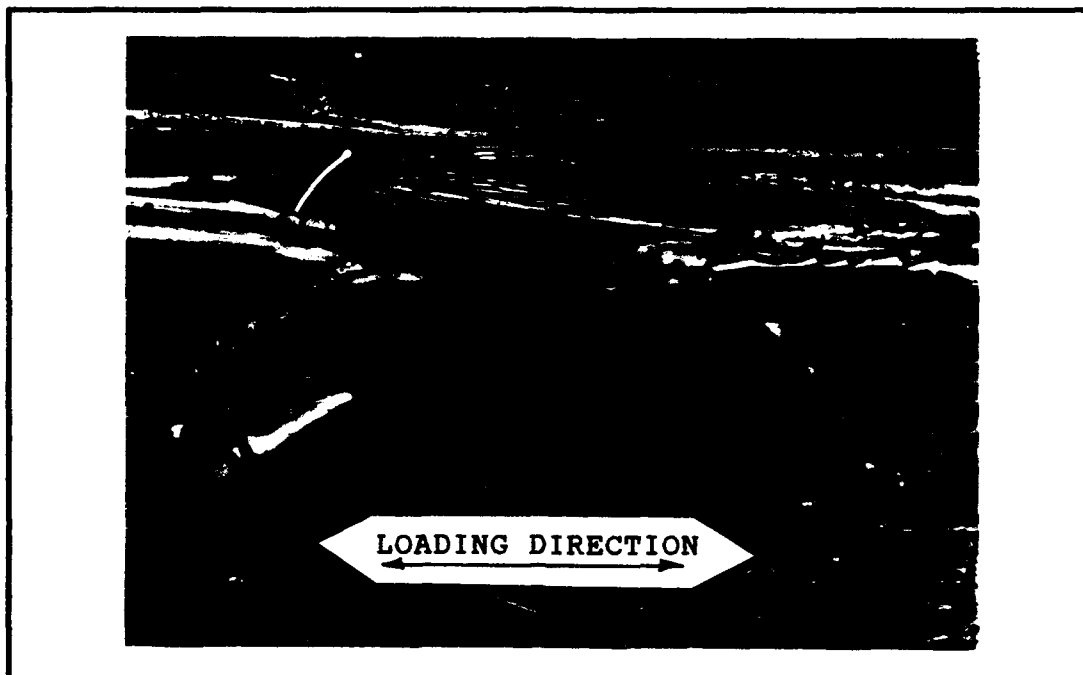


Figure 42 Face Replica of Cracks Emanating from hole on Specimen 93G01000

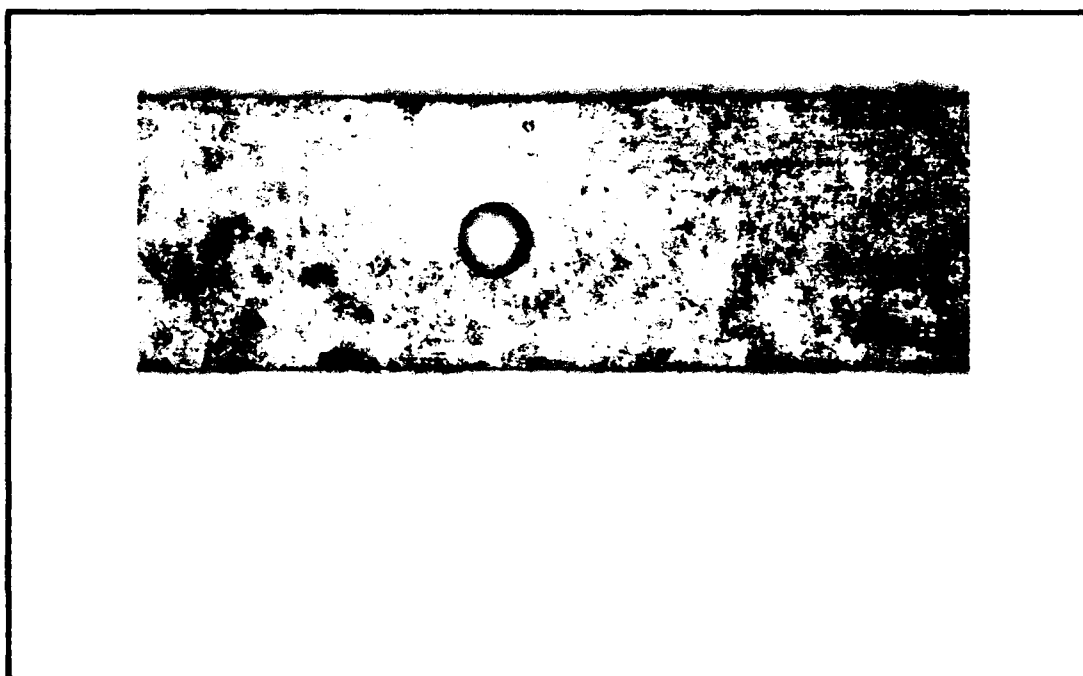


Figure 43 Specimen 92G01000 after 1,000,000 Cycles

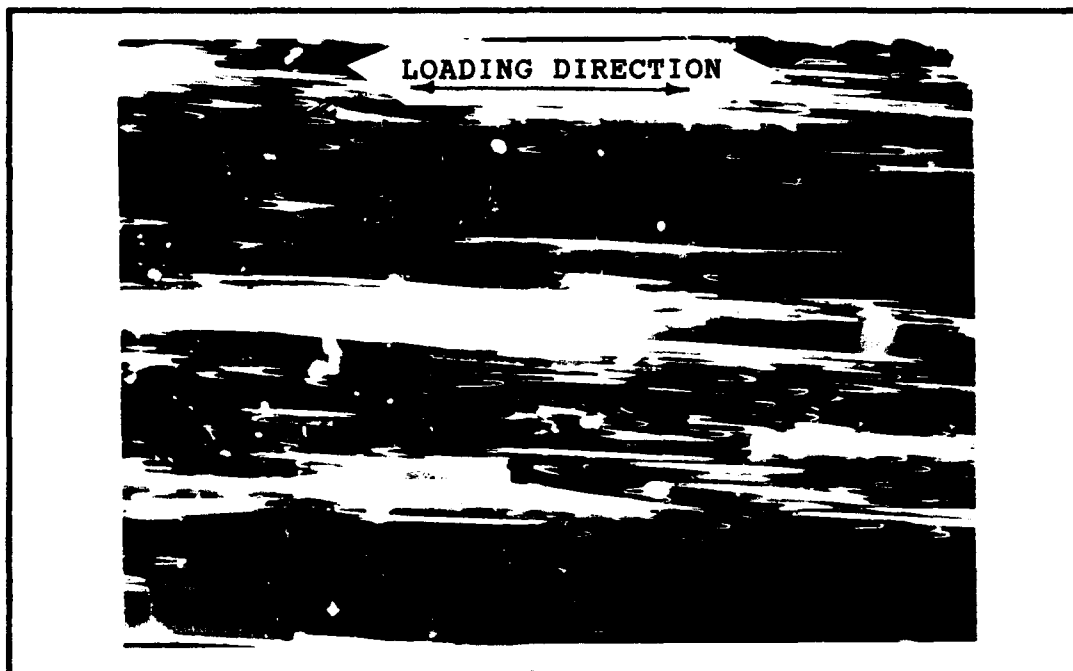


Figure 44 Edge Replica of Tension-Tension Fatigue Specimen, 50X

available material. Compression-compression fatigue at stress levels so far below the ultimate was assumed to cause no damage.

A tension-compression test with a maximum stress of 200 MPa and $R = -1$ was run to determine the effect of reversed cyclic loading on unidirectional specimens. Stress-strain curves for this test are shown in Figure 45. The tests with the cross-ply specimens showed that compressive loads applied to specimens already damaged by tensile loads would increase the damage at compressive load levels below that required to cause damage on their own. The same effect, although weaker, displayed itself with the unidirectional specimens.

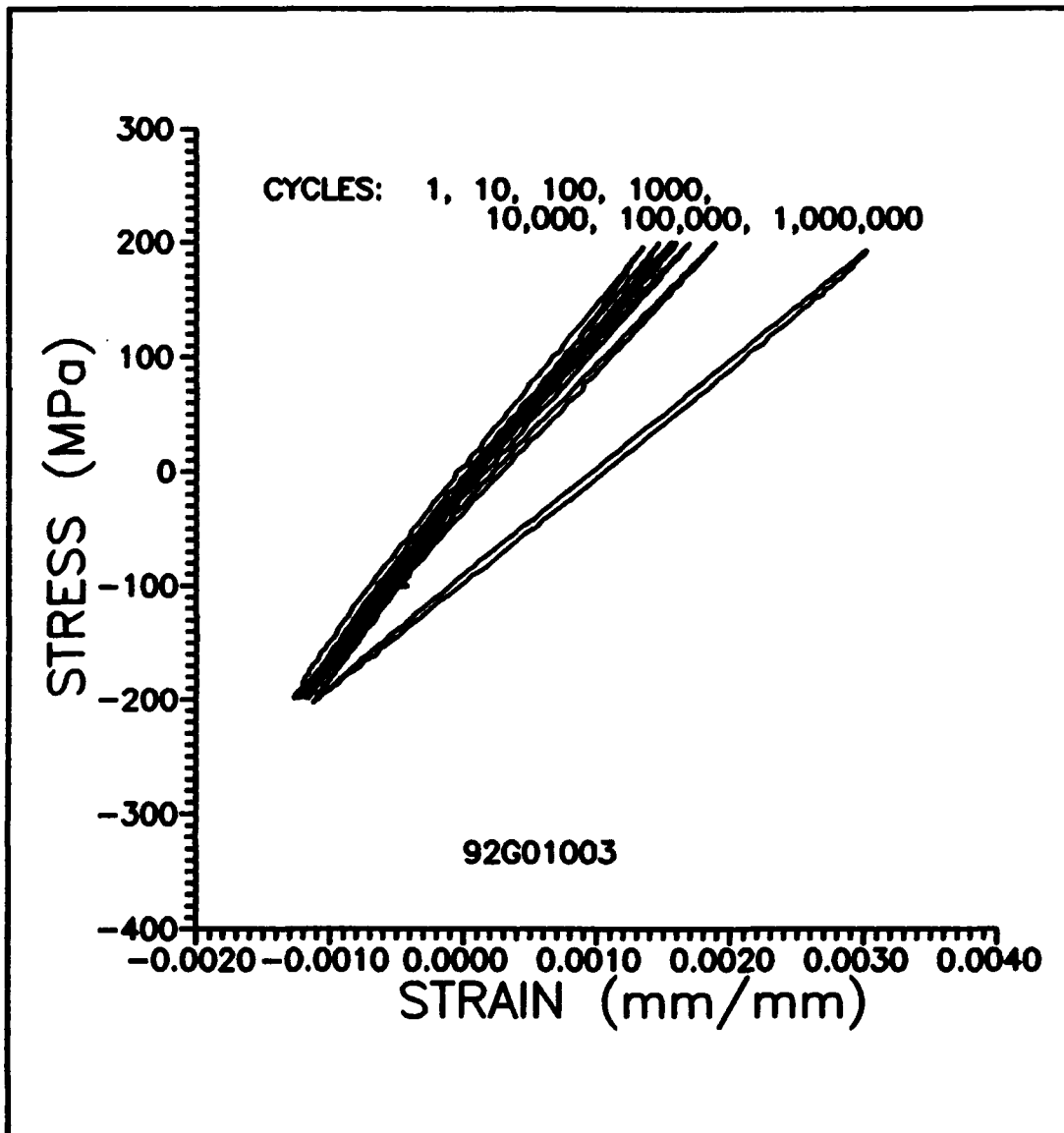
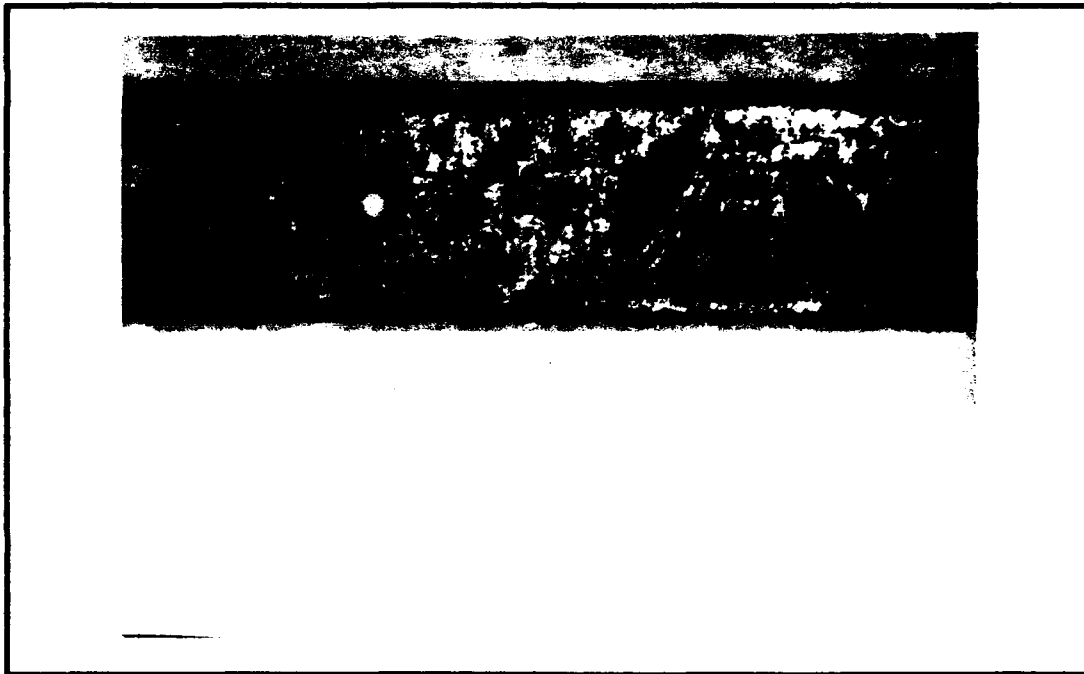
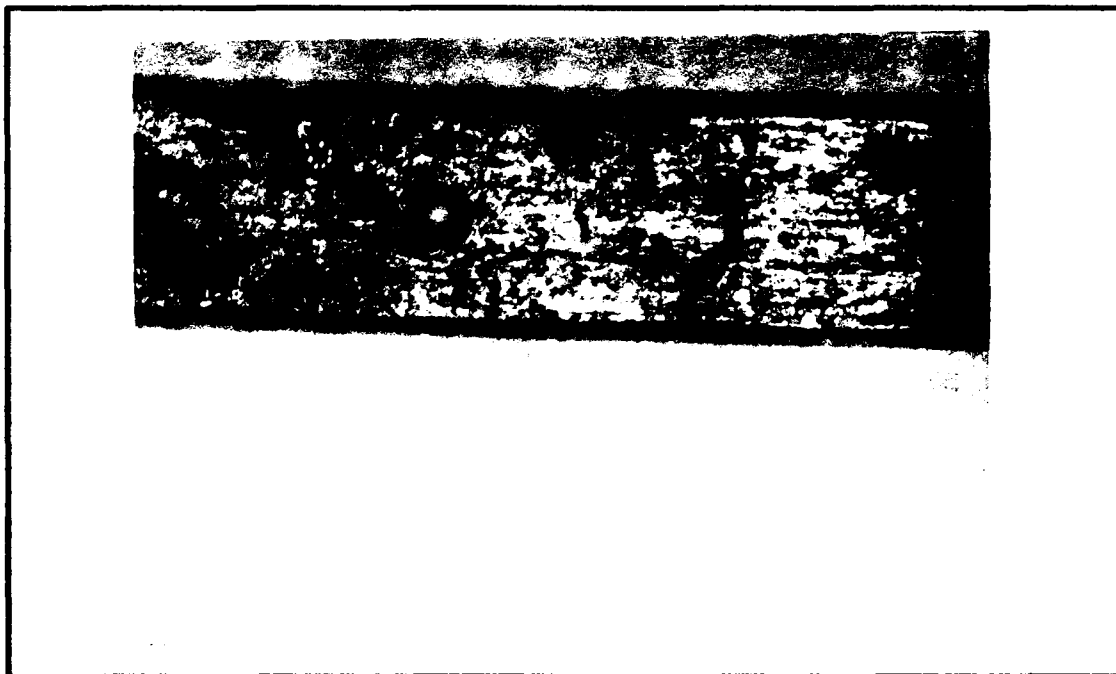


Figure 45 Tension-Compression, Stress-Strain Curves,
200 MPa

Specimen 92G01003 achieved runout but damage was significant. The photographs in Figures 46 and 47 clearly show the large longitudinal cracks which started at the hole running almost the complete length of the specimen. It is possible that the rigid grips slowed the crack growth once



**Figure 46 Front Face of Specimen 92G01003, 1,000,000
Cycles**



**Figure 47 Back Face of Specimen 92G01003, 1,000,000
Cycles**

it reached the tabs. The majority of the crack growth occurred after 200,000 cycles. This corresponds to the large drop in stiffness shown in Figure 48 and the increase in hysteretic energy density (Figure 49).

The normalized modulus is a good indicator of the damage state of a given specimen. Looking at Figure 48 some trends are evident. The rate of modulus decrease corresponds directly with the crack growth rate. The 200 MPa tension-tension specimen had only a minor decrease in stiffness and it also had only minor cracks as seen in Figures 42 and 43. The 300 MPa tension-tension specimen, as well as the two 200 MPa tension-compression specimens had sudden drops in stiffness corresponding to the rapid growth of the longitudinal face cracks. Once the 300 MPa tension-tension specimen's stiffness started to decline it went very quickly to failure. The 200 MPa tension-compression specimen's stiffness, on the other hand, gradually declined until it reached the same approximate level as the tension-tension specimen at failure. That portion of the tension-compression curves after 200,000 or 300,000 cycles is flat signifying no more damage is occurring. At this point the specimens were effectively failed. The longitudinal cracks on the faces were through the thickness and reached from tab to tab. The only things holding them together were the tabs.

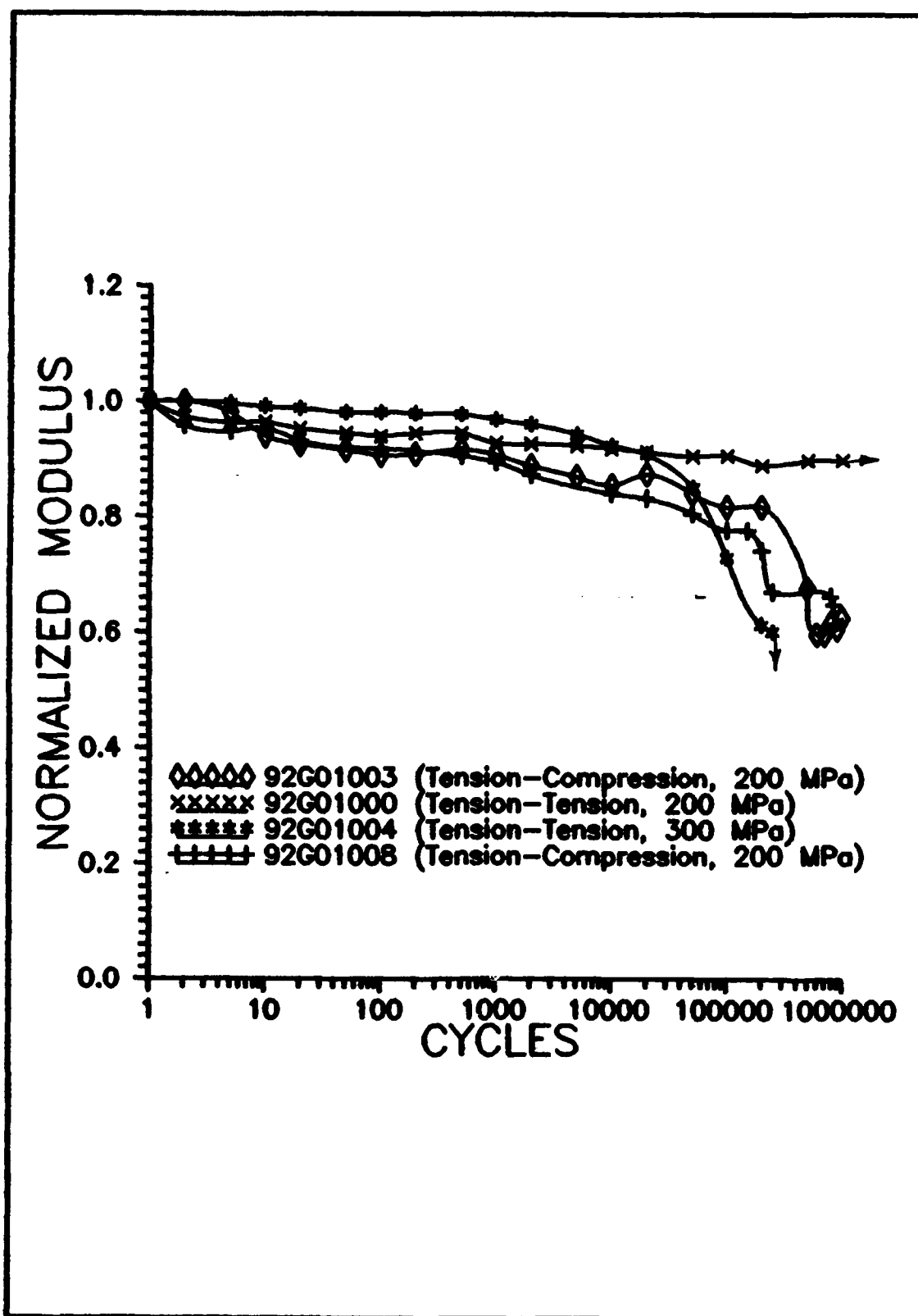


Figure 48 Unidirectional Normalized Stiffness Graphs

The hysteretic energy density curves provide even more insight into the damage progression. The most obvious trend is the increase in energy density just prior to failure. This correlates well with the stiffness curves.

The 300 MPa tension-tension curve had a relatively high energy density in cycle one. It then dropped down and began to rise again after 1,000 cycles. This specimen was tested above the proportional limit and the first cycle caused significant damage. After cycle one, the longitudinal cracks were cycling in Mode II or sliding mode and the energy density was dependent on the length of the crack. The sliding of the crack surfaces together left matrix "powder" on the lower grips during cycling. The 200 MPa tension-tension specimen had many transverse cracks but because the longitudinal cracks emanating from the hole were so small, the hysteretic energy density remained relatively low.

The energy density of the tension-compression fatigue specimens started low just like the tension-tension specimen, indicating the same damage level. However, once the longitudinal cracks formed, the compression loads helped them grow by opening them (Mode I) and the tensile loads caused them to slide increasing the energy density. The compression loads do not initiate the cracks but only lengthen them. The combination of Mode I (compression) and

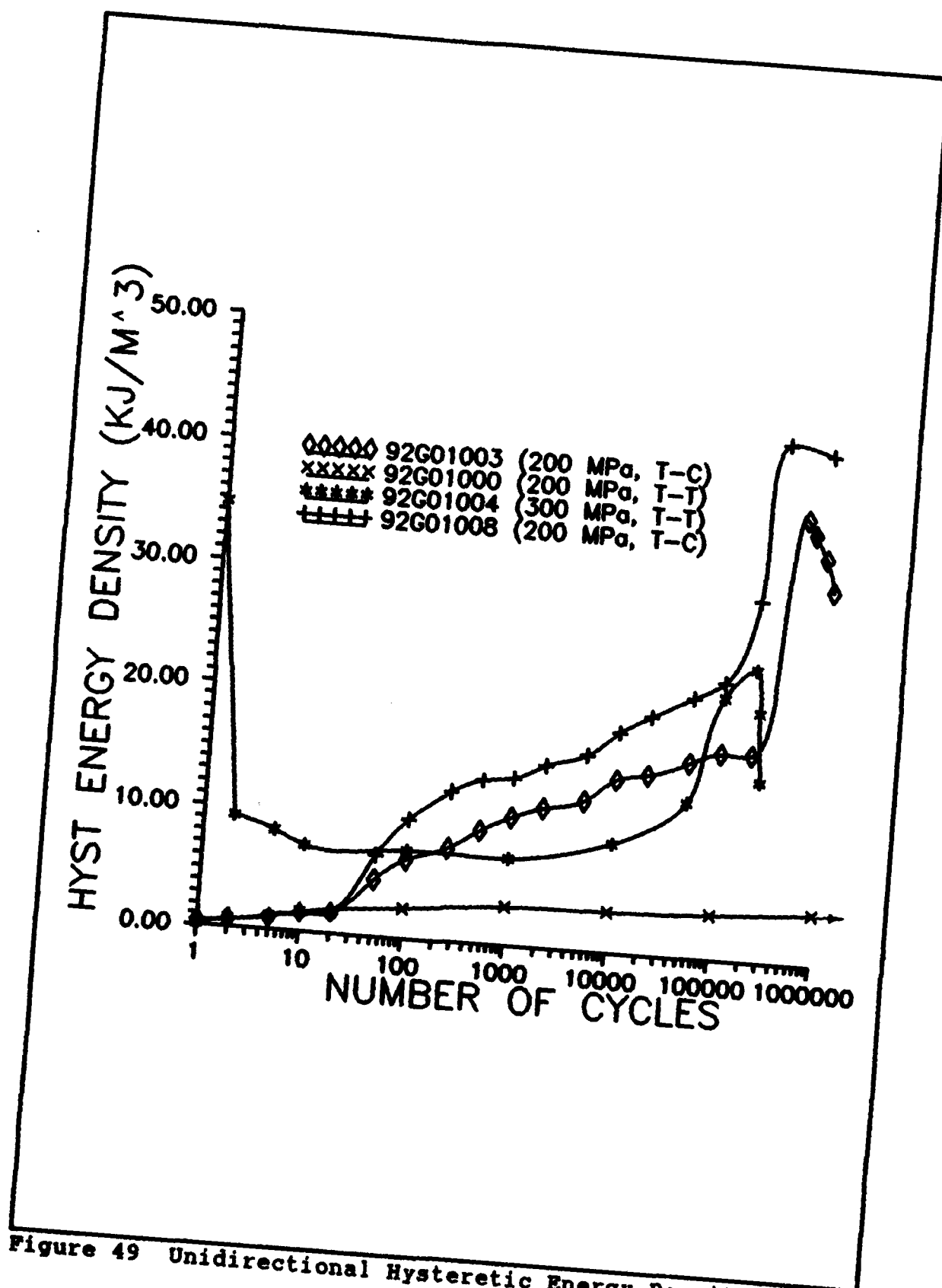


Figure 49 Unidirectional Hysteretic Energy Density Graphs

Mode II (tension) caused much greater and quicker damage than tension-tension alone.

There was very little difference in the amount of transverse cracking between the tension-tension fatigue and the tension-compression fatigue specimens (Figures 50 and 44).

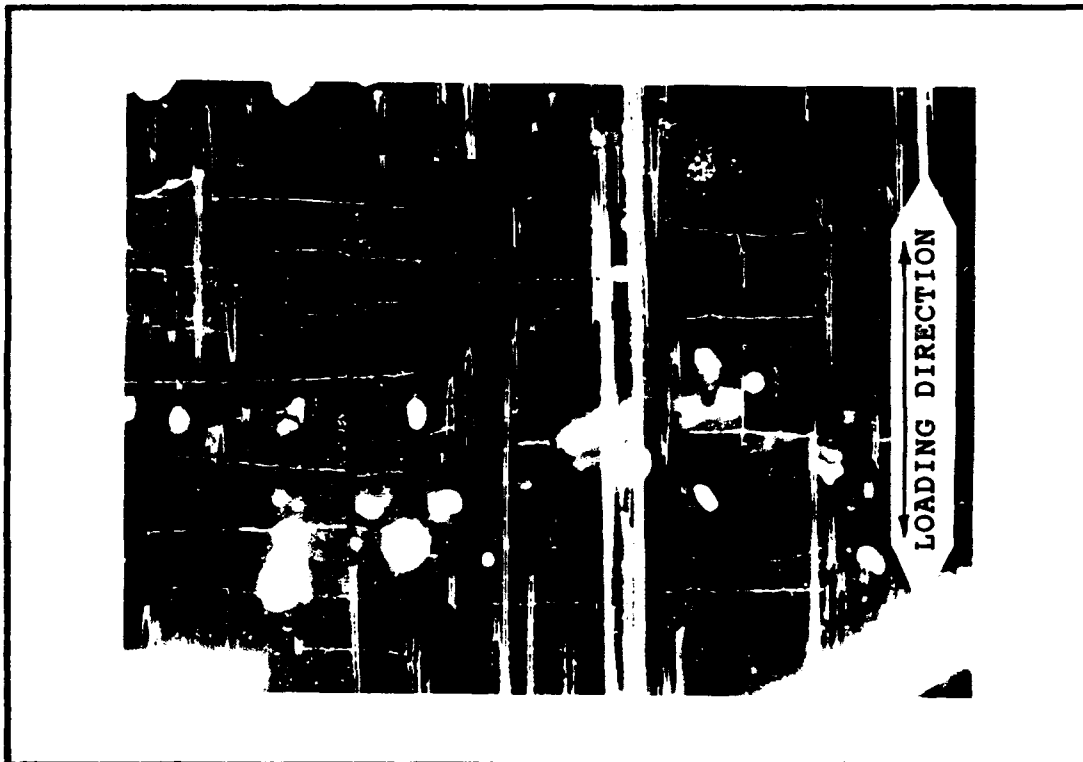


Figure 50 Tension-Compression Fatigue Edge Replica

The initiation of the longitudinal cracks on the face of the specimen occurred the same way in tension-compression fatigue as it did in tension-tension fatigue, which was explained in Chapter II. Four cracks formed and grew from the hole edge (Figures 51 and 52). Normally, two cracks

would become dominant and would propagate to the ends of the specimen causing failure.

The initiation of the longitudinal face cracks is due to the shear stress concentration at the hole periphery. The presence of the hole has a definite effect on the fatigue life of unidirectional specimens since these longitudinal face cracks are the dominant damage mode leading to failure.

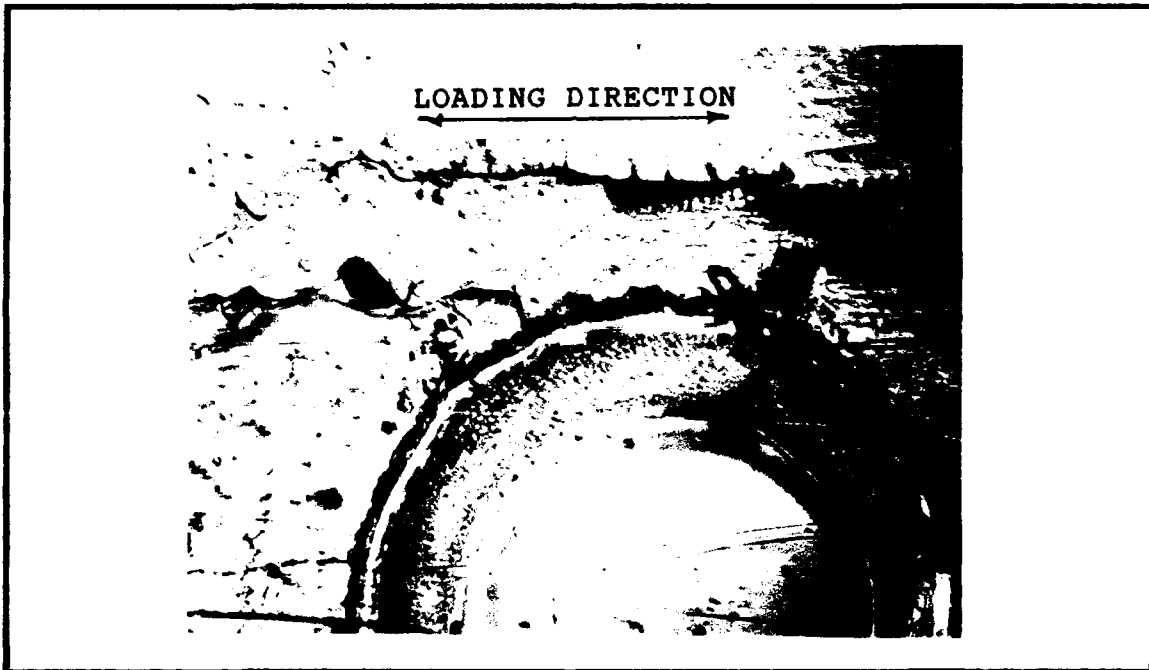


Figure 51 Specimen Face at 10,000 Cycles

2. Analytical Comparisons

Using the Whitney-Nuismer Model to predict the notched fatigue limit requires known notched and unnotched ultimate stress and the unnotched fatigue limit. This data is available for tension-tension fatigue and has been shown to apply to SiC/1723 by Moschelle [5]. However, the notched ultimate stress from this batch of material was significantly higher than that which Moschelle found. This caused the predicted fatigue limit to be between 302 and 373 MPa. The 300 MPa tension-tension fatigue specimen failed at 270,655 cycles. Thus, if one is to apply the Whitney-Nuismer Model to this material it is imperative to use ultimate and fatigue limit stress values from the same batch of material. As fabrication becomes standardized, strength differences will be reduced and the model should apply regardless of batch.

No fatigue limit was found for tension-compression fatigue so the model does not apply, given the available data. Tension-compression fatigue testing of unnotched specimens should be run at various load ratios to determine if a fatigue limit exists. .

V. CONCLUSIONS AND RECOMMENDATIONS

A. Conclusions

Tension-compression fatigue testing was performed on unidirectional, $[0]_4$, and cross-ply, $[(0/90)_2]_3$, notched laminates of SiC/1723. The specimens had a center hole ultrasonically drilled in them to evaluate its effect on their fatigue life. The diameter to width ratio was 0.26 ± 0.02 .

Static tensile tests of the cross-ply provided stress values for the two proportional limits, original stiffness, and ultimate strength. The proportional limits were at 55 and 160 MPa. Static compression tests were linear up until sudden catastrophic failure.

The proportional limits from the static tension tests were used as a guide to determine a fatigue limit for tension-tension fatigue. A fatigue limit of 150 MPa was established. A compression-compression fatigue test at 150 MPa maximum stress demonstrated that no damage took place during compression-compression fatigue at this stress level. This was supported by no change in stiffness, very small hysteretic energy densities, and no visible damage on acetate replicas.

Tension-compression testing at a maximum stress of 150 MPa and a load ratio of -1 led to continuous damage accumulation. Reversed cyclic loading decreased fatigue

life from runout (> 1,000,000 cycles) for tension-tension fatigue to between 200,000 and 400,000 cycles. Damage progression consisted of a build-up and stabilization of transverse cracks and initiation of longitudinal cracks in the 90 degree plies early in cycling. The longitudinal cracks continued to grow parallel to the loading direction. Near the end of the fatigue life, multiple longitudinal cracks would form and combine with the transverse cracks adjacent to the hole where the effective area was least. This effectively eliminated the 90 degree plies from supporting any compressive loads and allowed the specimen to buckle.

Fatigue life reduction of notched specimens compared to unnotched specimens in tension-compression fatigue was not significantly different. The major effect of the hole was to reduce the area.

The normalized stiffness was a good indicator of the damage state and reduction of the stiffness by 39% indicated failure before 1,000,000 cycles as predicted by classical laminated plate theory.

Comparisons of the hysteretic energy densities were useful in determining relative damage states for different load ratios and maximum stress levels at particular cycles.

Testing continued with the unidirectional laminate. Once again static tensile and compression tests were conducted. Static tension tests identified the proportional

limit at 255 MPa. Damage in the static tensile tests consisted of longitudinal face cracks emanating from the hole at the theoretical maximum shear stress locations. These cracks extended in the loading direction until failure.

Tension-tension fatigue tests further established the fatigue limit. Testing above the fatigue limit caused the longitudinal face cracks to grow, eventually causing failure. Testing below the fatigue limit allowed the longitudinal cracks to form but their growth was inhibited very early in the cycling and they did not fail.

The behavior under fully reversed cyclic loading was examined at a maximum stress level below the fatigue limit for tension-tension fatigue. Tension-compression fatigue caused continuous damage accumulation and reduced the fatigue life once again. Longitudinal face cracks originated the same way whether for static tension, tension-tension fatigue, or tension compression fatigue. The compressive loads helped the cracks to grow by Mode I while the tensile loads helped the longitudinal face cracks grow by Mode II.

There was no significant difference between the density or character of the transverse cracks in tension-tension fatigue compared to those in tension-compression fatigue.

Both normalized stiffness and hysteretic energy density were good indicators of the damage state. Hysteretic energy

density was especially good at showing where the damage in the tension-compression tests diverged from that of the tension-tension tests.

The hole had a definite affect on the damage. The longitudinal face cracks that eventually caused the failure initiated due to the shear stress concentration at the hole.

B. Recommendations

There are still many areas that require further study before SiC/1723 in particular and ceramic matrix composites, in general, can be adequately modeled. Only a few will be suggested here.

One projected use of ceramic matrix composites is for future turbine engines, as discussed in Chapter I. These applications require materials to withstand many service cycles at high temperatures. Fatigue behavior at constant high temperatures and cycling of both temperature and load should be examined.

Variations of the load ratio for unnotched unidirectional specimens would provide more insight into the added effect of the hole.

Cycling to limits beyond 1,000,000 cycles may also prove interesting for unidirectional specimens. Even for the tension-tension specimens the stiffness was steadily declining. Continuation of this trend could become critical, depending on the application.

Bibliography

1. Wang, Z. G., et al. "Mechanical Behaviour of a Cross-weave Ceramic Matrix Composite," Journal of Materials Science. Vol. 26, 1991, page 4751.
2. "GE, Pratt Studying Combustor, Nozzle Materials for HSCT", Aviation Week & Space Technology. August 31, 1992, page 66.
3. Agarwal, B. D. and Broutman, L. J., Analysis and Performance of Fiber Composites, Second Edition, New York: John Wiley & Sons, Inc., 1990, page 288.
4. Bullock, Capt. D.E., Failure Characterization of a Fiber Reinforced Ceramic Matrix Composite with Circular Holes. MS Thesis, AFIT/GAE/ENY/91D. School of Engineering, Air Force Institute of Technology (AU), Wright-Patterson AFB, OH, December 1991.
5. Moschelle, Capt. W. R., Fatigue Behavior and Failure Mechanisms of Centrally Notched [0] and [(0/90)] Silicon Carbide Reinforced Aluminasilicate Glass. MS Thesis, AFIT/GAE/ENY/91D. School of Engineering, Air Force Institute of Technology (AU), Wright-Patterson AFB, OH, December 1991.
6. Prewo, K. M. "Fatigue and Stress Rupture of Silicon Carbide Fiber-Reinforced Glass Ceramics," Journal of Materials Science. Vol. 22, 1987, pp. 2695-2701
7. Zawada, L. P., Butkus, l. m. and Hartmann, G. A., "Tensile and Fatigue Behavior of Silicon Carbide Fiber-Reinforced Aluminosilicate Glass", Journal of the American Ceramic Society. Vol. 74, No 11, November 1991. pp 2851-2858.
8. Tracy, Capt. G.D., Failure Mechanisms in a Quasi-Isotropic Ceramic Composite Laminate Under Tensile Fatigue Loading. MS Thesis, AFIT/GAE/ENY/91D. School of Engineering, Air Force Institute of Technology (AU), Wright-Patterson AFB, OH, December 1990.
9. Zawada, L. P. and Pernot, Capt. J. J., Effects of Load Ratio on the Fatigue Behavior of Ceramic Matrix Composites, Presentation Slides, April 1992.
10. Jones, R. M., Mechanics of Composite Materials. New York: Hemisphere Publishing Co., 1975 pp 46-51, 147-166.

11. Tsangarakis, n. et al. "Static and Fatigue Notch Strength Prediction in Alumina Fiber Reinforced Aluminum Plates with a Circular Hole", Journal of Composite Materials, Vol. 22, April 1988, pp. 386-393
12. Hwang, W. and Han, K. S., "Fatigue of Composites. Fatigue Modulus Concept and Life Prediction", Journal of Composite Materials. Vol. 20, March 1986, pp.154-165.
13. Greszczuk, L. B., "Stress Concentration and Failure Criteria for Orthotropic and Anisotropic Plates with Circular Openings", Composite Materials: Testing and Design (Second Conference), ASTM STP 497, 1972, pp. 363-381.
14. Bachmann, Capt. S. E, Transverse Cracking in a Fiber Reinforced Ceramic Matrix Composite. MS Thesis, AFIT/GAE/ENY/90D-2. School of Engineering, Air Force Institute of Technology (AU), Wright-Patterson AFB, OH, December 1990.
15. Butkus, L., Zawada, L. P., and Hartman, G. A., "Fatigue Testing of Ceramic Matrix Composites at Room and Elevated Temperatures", pending publication by American Society for Testing and Materials, 1990.
16. Sanders, Capt. B., Doctoral Candidate, Air Force Institute of Technology (AU), Wright-Patterson AFB, OH, Personel Interview, April 1992.
17. Yajima, s. et al. "Synthesis of a Polytitanocarbosilane and its Conversion into Inorganic Compounds", Journal of Materials Science, Vol 16, 1981, pp. 1349-1355.

Appendix A: Testing Summary

Table I Cross-ply Tests Summary

Specimen Number	Type of Test	R	Maximum Stress (MPa)	Initial Modulus (GPa)	Cycles to Failure
92G03007	Static Tension	N/A	288	124	N/A
92G04005	Static Tension	N/A	281	121.5	N/A
92G03010	Static Compression	N/A	-423.5	118	N/A
92G03011	Tension-Tension	.1	250	102	≈37,000
92G03014	Tension-Tension	.1	200	89	64,227
92G03005	Tension-Tension	.1	150	113.48	Runout
92G03004	Tension-Compression	-1	150	113.22	304862
92G03013	Tension-Compression	-1	150	106	291795
92G04003	Tension-Compression	-1	150	110	245225
92G04001	Tension-Compression	-1	150	105.8	315753
92G03006	Tension-Compression	-1	150	106.1	362584
92G04011	Compression - Compression	10	150	103.5	Runout

Notes: 1) Maximum stresses are for minimum (notched) area.

2) 92G03006 had the extensometer near the hole.

All other tests had it away from the hole.

Table III Unidirectional Tests Summary

Specimen Number	Type of Test	R	Maximum Stress (MPa)	Initial Stiffness (GPa)	Cycles to Failure
92G01005	Static Tension	N/A	467	150	N/A
92G01007	Static Compression	N/A	-764.8	122	N/A
92G01004	Tension-Tension	.1	300	155	270,655
92G01000	Tension-Tension	.1	200	146.3	Runout
92G01003	Tension-Compression	-1	200	147.3	Runout [†]
92G01008	Tension-Compression	-1	200	139.6	Runout ^{††}

Notes: 1) Maximum Stress are at minimum (notched) area.

2) All tests had extensometer close to the hole.

* Achieved 1,000,000 cycles but cracks extended full length of the specimen. Specimen held together by tabs and grips. Effective failure at \approx 400,000 cycles.

** Test stopped at 854,774 cycles. Same condition as 92G01003. Effective failure at \approx 400,000 cycles.

Appendix B: Additional Cross-ply Data Curves

Figure 52 shows minimum and maximum strain values versus cycle for Specimen 92G03014. This specimen was cycled in tension-tension fatigue with a notched area stress of 200 MPa. This specimen failed at 64,227 cycles. Up to 10,000 cycles the difference between the maximum and minimum strain increased steadily. Problems with the extensometer slippage prevented accurate data acquisition.

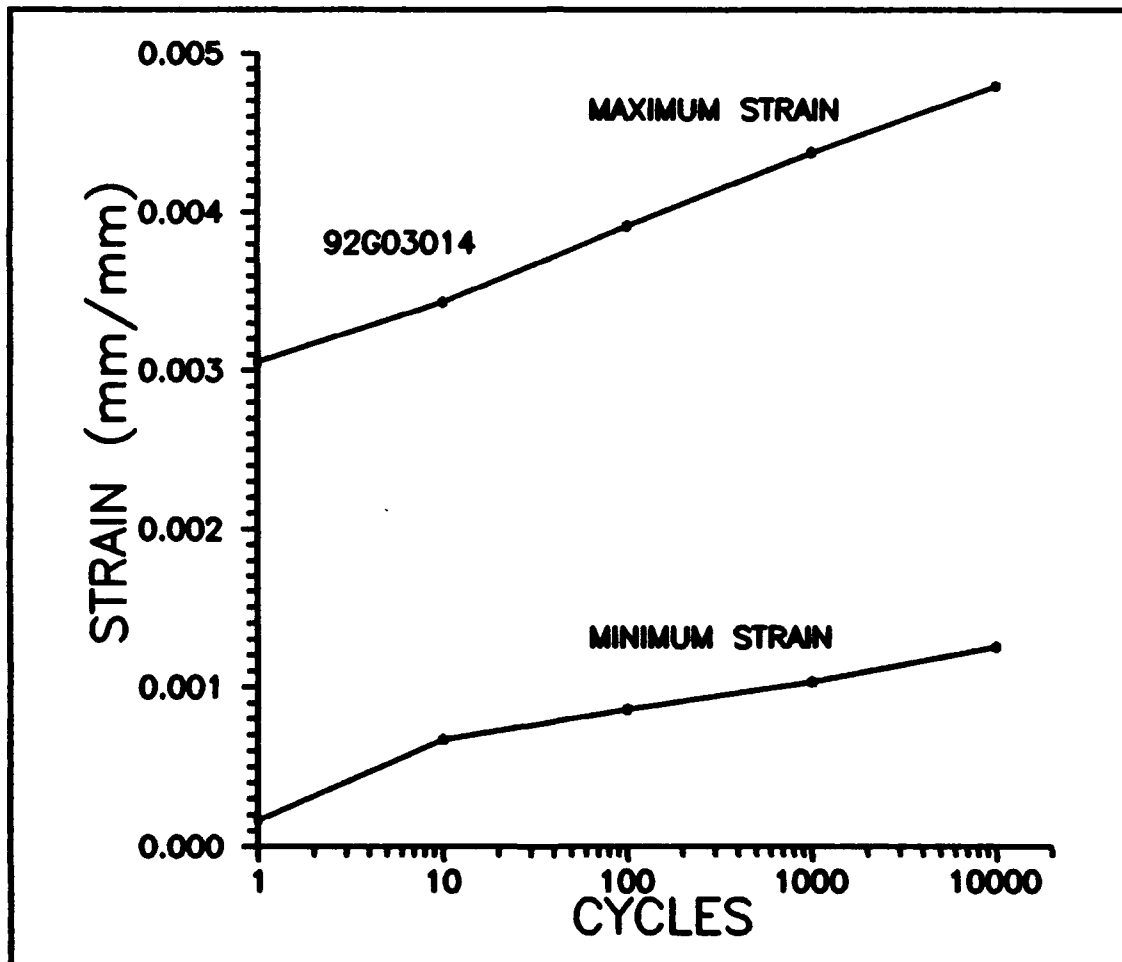


Figure 52 Strain vs. Cycles, 92G03014

The curves in Figure 53 also show a steady, but much slower, increase in the difference between the maximum and minimum strain. Specimen 92G03005 was cycled in tension-tension at a maximum notched area stress of 150 MPa and survived 1,000,000 cycles.

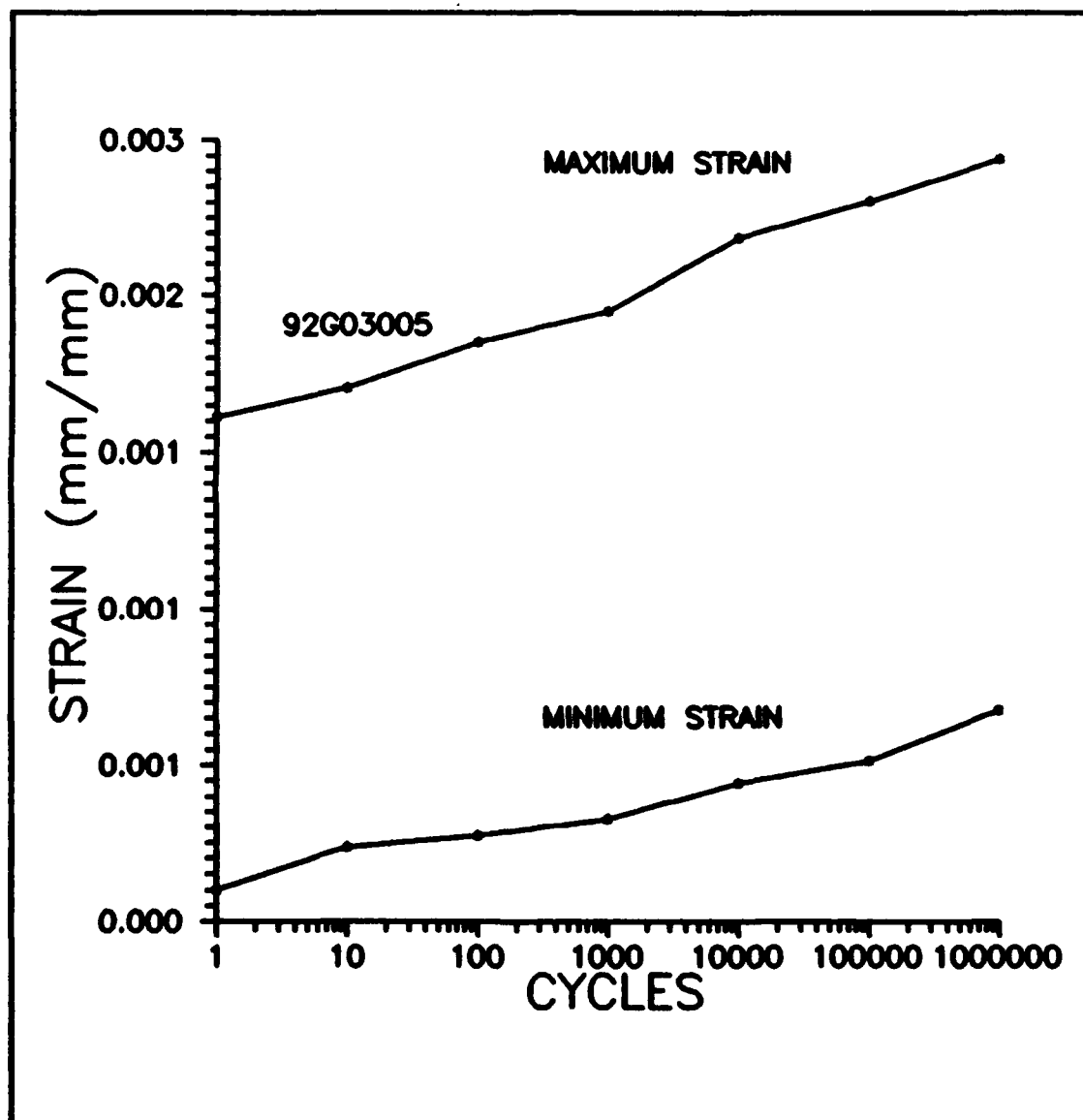


Figure 53 Strain versus Cycles, 92G03005

Figure 54 shows the strain vs. cycles curves again but this time for a tension-compression fatigue specimen. The extensometer was away from the hole for this test. Once again problems with extensometer slippage prevented accurate strain data acquisition after 100,000 cycles.

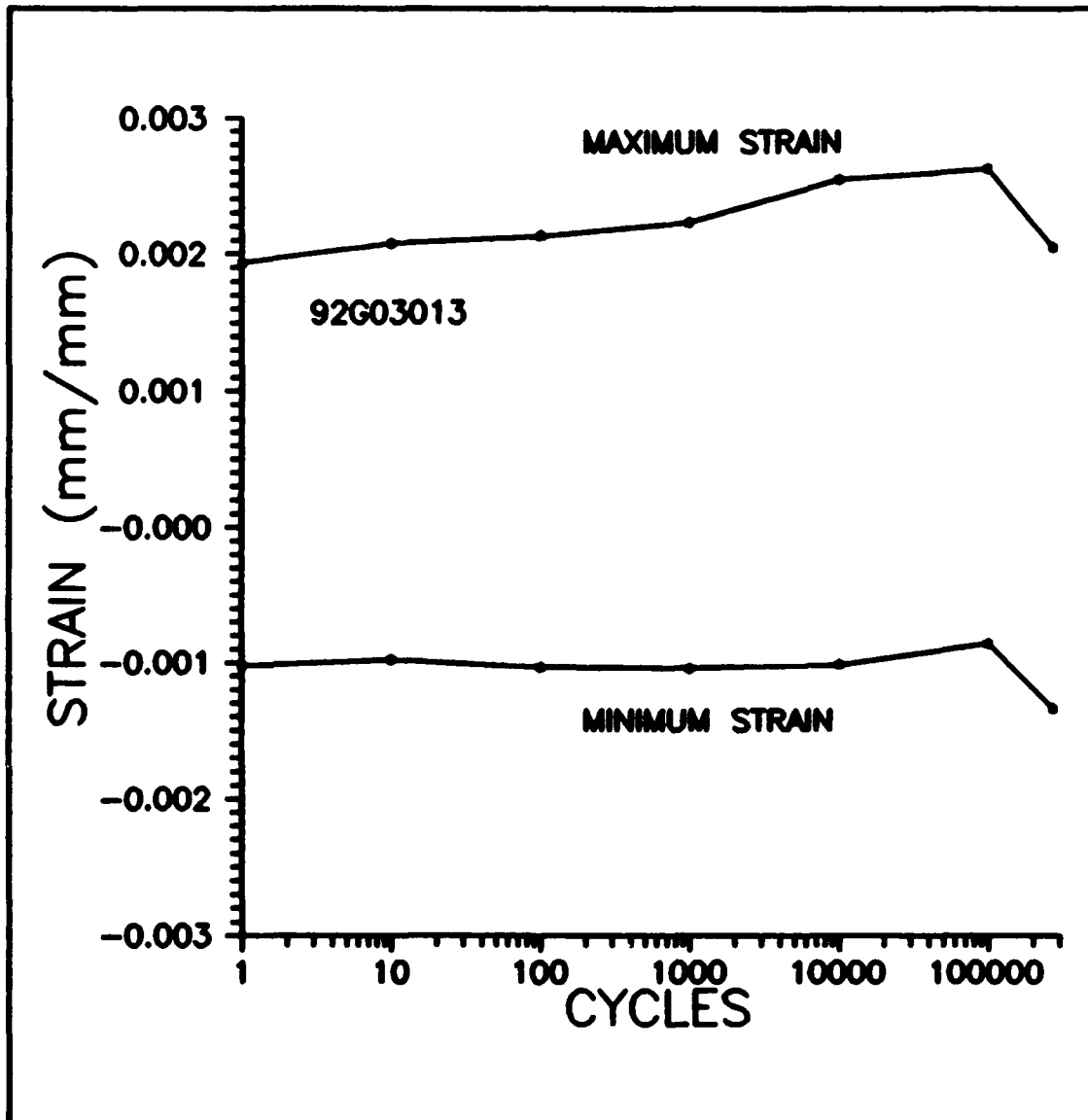


Figure 54 Strain versus Cycles, 92G03013

Specimen 92G03006 had the extensometer near the hole and the maximum strain data is significantly higher than that for Specimen 92G03013 indicating more damage near the hole. The jump between 100 and 1000 cycles was due to extensometer slippage. The difference between the minimum and maximum strains increased significantly after 100,000 cycles. The damage rate was also increasing at this time. This specimen failed at 362,584 cycles.

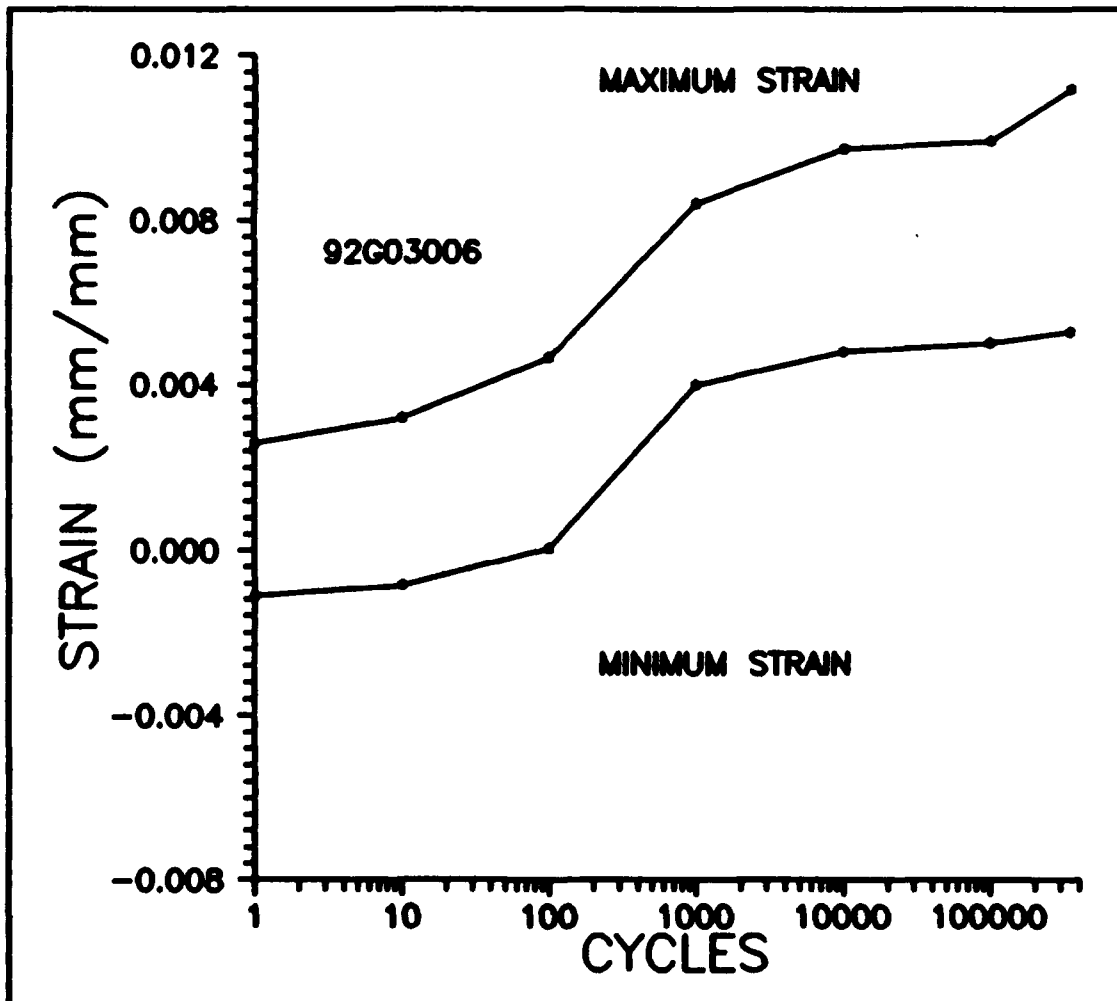


Figure 55 Strain versus Cycles, 92G03006

The previous data is also shown below in tabular form.

Table IV Tension-Tension Maximum and Minimum Strains

CYCLES	92G03014		92G03005	
	MINIMUM STRAIN	MAXIMUM STRAIN	MINIMUM STRAIN	MAXIMUM STRAIN
1	0.00016308	0.0030532	0.00009966	0.0016127
10	0.00067043	0.0034337	0.00023556	0.0017033
100	0.00086070	0.0039140	0.00027180	0.0018482
1000	0.00103280	0.0043760	0.00032616	0.0019479
10000	0.00125030	0.0047927	0.00044393	0.0021834
100000	N/A	N/A	0.00051640	0.0023012
1000000	N/A	N/A	0.00067950	0.0024371

Table V. Tension-Compression Maximum and Minimum Strains

CYCLES	92G03013		92G03006	
	MINIMUM STRAIN	MAXIMUM STRAIN	MINIMUM STRAIN	MAXIMUM STRAIN
1	-0.0010238	0.0019298	-0.0011235	0.0025732
10	-0.0009785	0.0020747	-0.0008517	0.0032074
100	-0.0010328	0.0021291	0.00006342	0.0046653
1000	-0.0010419	0.0022287	0.00400470	0.008430
10000	-0.0010147	0.0025458	0.00482000	0.0097580
100000	-0.0008607	0.0026274	0.00502870	0.0099303
270000	-0.0013409	0.0020475	N/A	N/A
350000	N/A	N/A	0.00529130	0.011181

The following figure shows the stress-strain curves for Specimen 92G03006. This data was taken with the extensometer spanning the hole. These curves were not included in the main body of this report due to the obvious error in the strain values after cycle 100. This error is due to the extensometer slipping. The rest of the data, however, is good, including the stress-strain relationships after 100 cycles.

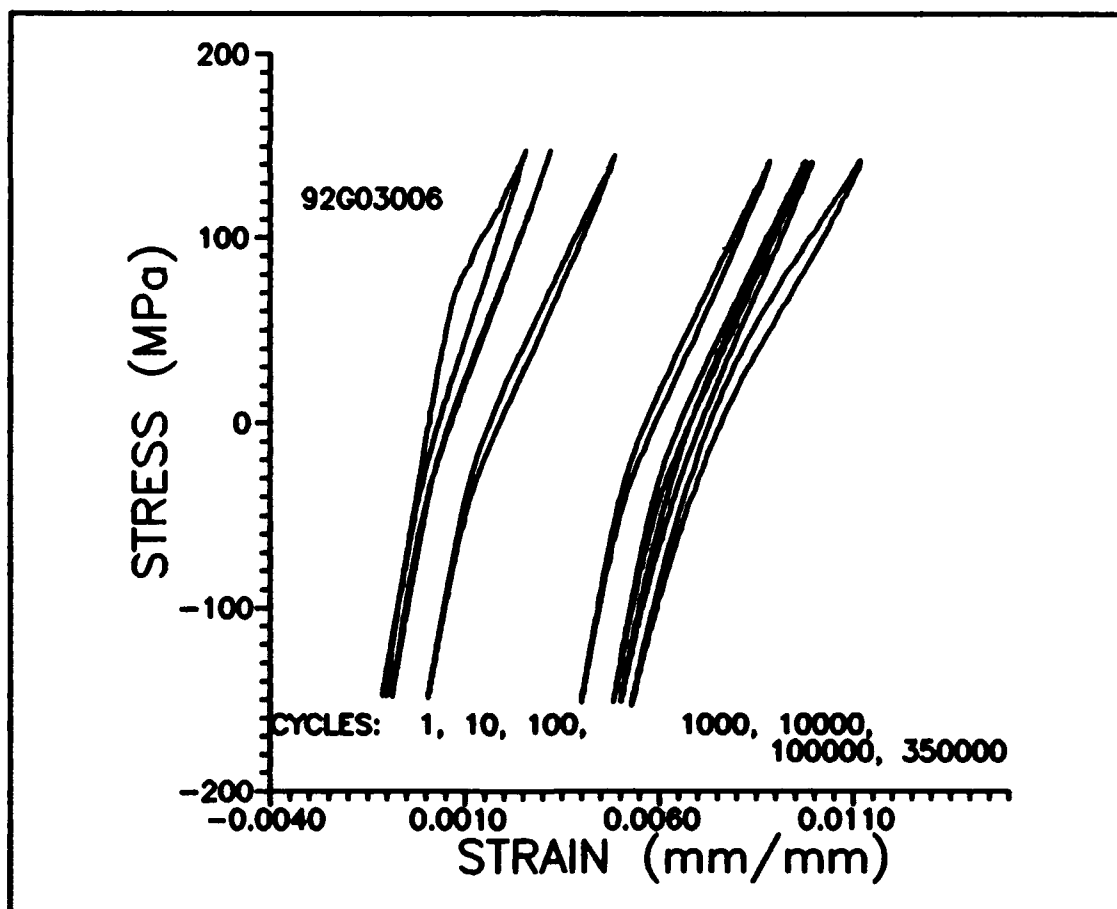


Figure 56 Specimen 92G03006 Stress Strain Curves

Vita

William A. Weidenaar was born 12 August 1959 in Grand Rapids, Michigan. He graduated from Inter-City Christian High School in 1977 and received his B.S. in Mechanical Engineering from the University of Michigan and his B.S. in Engineering and Letters from Calvin College in 1982. He joined the Air Force and was commissioned in May 1983 after completing Officer Training School. His assignments included the Air Force Weapons Laboratory, Kirtland AFB, NM, Aeronautical Systems Division, Detachment 11, Comiso AS, Italy, and Headquarters, United States Air Forces, Europe, Ramstein AB, Germany. He entered the School of Engineering, Air Force Institute of Technology in May 1991. He left the Air Force in September 1992 and is presently employed by Ford Motor Company.

December 1992 Master's Thesis (Final)
 Behavior of a Centrally Notched
 Cross-ply and Unidirectional Ceramic Matrix
 Composite in Tension-Compression Fatigue

William A. Weidenaar

Air Force Institute of Technology

AFIT/GAE/ENY/92D

WL/MLLN
 WPAFB, OH 45433

Approved for public release: distribution
 unlimited

Centrally notched (hole), cross-ply, $[(0/90)_2]_s$, and unidirectional, $[0]_s$ laminates of Silicon Carbide fiber-reinforced Aluminosilicate glass, SiC/1723, were fatigue tested under tension-compression loading with a load ratio of -1. Damage accumulated continuously for both lay-ups, leading to eventual failure and a reduced fatigue life. Critical damage in the cross-ply consisted of longitudinal cracks in the 90° plies growing and combining with transverse cracks to effectively eliminate the 90° plies' load carrying capability and allowing the specimen to buckle. Critical damage in the unidirectional lay-up consisted of longitudinal cracks which initiated at the shear stress concentration points on the hole periphery. Reversed cyclic loading caused continued crack growth at maximum stresses below the tension-tension fatigue limit. The cross-ply lay-up appeared insensitive to the hole, while critical damage in the unidirectional lay-up was dependent on the shear stress concentrations at the hole.

14. SUBJECT TERMS			15. NUMBER OF PAGES
Ceramic Matrix Composite, Tension-Compression Fatigue, Notched Specimen			100
17. SECURITY CLASSIFICATION OF REPORT			16. PRICE CODE
Unclassified			
17. SECURITY CLASSIFICATION OF THIS PAGE	18. SECURITY CLASSIFICATION OF ABSTRACT	19. LIMITATION OF ABSTRACT	
Unclassified	Unclassified	UL	